공학박사학위논문

무익기형 전기 추진 수직 이착륙기에 대한 다학제 해석 및 시뮬레이션 프레임워크

Multidisciplinary Analysis and Simulation Framework for Wingless-type eVTOL

2023 년 2 월

서울대학교 대학원

항공우주공학과

김 형 석

무익기형 전기 추진 수직 이착륙기에 대한 다학제 해석 및 시뮬레이션 프레임워크

Multidisciplinary Analysis and Simulation Framework for Wingless-type eVTOL

지도교수 이 관 중

이 논문을 공학박사 학위논문으로 제출함

2022 년 11 월

서울대학교 대학원

항공우주공학과

김 형 석

김형석의 공학박사 학위논문을 인준함

2022 년 12 월

위 원 장 :　　　　김 규 홍

부위원장 :　　　　이 관 중

위　　원 :　　　　정 신 규

위　　원 :　　　　김 태 우

위　　원 :　　　　조 영 민

Abstract

Multidisciplinary Analysis and Simulation Framework for Wingless-type eVTOL

Hyeongseok Kim

Department of Aerospace Engineering

The Graduate School

Seoul National University

A wingless-type electric vertical take-off and landing (eVTOL) is one of the representative aircrafts utilized logistics and delivery, search and rescue, military, agriculture, and inspection of structures. For a small unmanned aerial vehicles of the wingless-type eVTOL, a quadrotor is a representative configuration to operate those missions. For a large size of the wingless-type eVTOL, it is an aircraft for urban air mobility service (UAM) specialized for intracity point-to-point due to its advantages such as efficient hover performance, high gust resistance, and relatively low noisiness.

I

The rotating speed of the multiple rotors in the wingless-type eVTOL has to be changed continuously to achieve stable flight. Moreover, the speed and the loaded torque of the motors also continuously change. Therefore, it is necessary to analyze the rotor thrust and torque with respect to the speed of each rotor as assigned by the controller to predict the flight performance of the wingless-type eVTOL. The electric power required by the motors is also necessary to be predicted based on the torque loaded to the motors to maintain the rotating speed.

This study suggests a flight simulation framework based on these multidisciplinary analyses including control, rotor aerodynamics, and electric propulsion system analysis. Using the flight simulation framework, it is possible to predict the flight performance of the wingless-type eVTOL for given operating conditions.

The flight simulation framework can predict the overall performance required to resist the winds and the corresponding battery energy of a quadrotor. Flight endurance of an industrial quadrotor was examined under light, moderate, and strong breeze modeled by von Kármán wind turbulence with Beaufort wind force scale. As a result, it is found that the excess battery energy is increased with ground speed, even under the same wind conditions. As the ground speed increases, the airspeed is increased, led to higher frame drag, position error, pitch angle, and required mechanical power, consequently. Moreover, the quadrotor is not operable beyond a certain wind and ground speed since the required rotational speed of rotors exceeds the speed limit of motors.

The simulation framework can also predict the overall performance of a wingless eVTOL for UAM service. Because of its multiple rotors, rotor–rotor interference inevitably affects flight performance, mainly depending on inter-rotor distance and rotor rotation directions. In this case, there is an optimal rotation direction of the multiple rotors to be favorable in actual operation. In this study, it was proposed that a concept of rotor rotation direction that achieves the desirable flight performance in actual operation. The concept is called FRRA (Front rotor's Retreating side and Rear rotor's Advancing side). It was found that FRRA minimizes thrust loss due to rotor-rotor interference in high-speed forward flight. For a generic mission profile of UAM service, the rotation direction set by FRRA reduces the battery energy consumption of 7 % in comparison to the rotation direction of unfavorable rotor-rotor interference in operation.

III

Table of Contents

VI

Nomenclature

English symbols

C_D	Drag coefficient of a body frame
C_d	Drag coefficient of an airfoil in a blade element
C_l	Lift coefficient of an airfoil in a blade element
C_P	Power coefficient of a rotor
C_{RSM}	Coefficient matrix of the surrogate model
C_T	Thrust coefficient of a rotor
c_r	Chord length, m
D_L	Distance of adjacent bars of a body frame, m
D_L	Distance of adjacent bars of a body frame, m
D_t	Duty ratio of a motor
dD	Differential drag force of a blade, N/m
$dF_{x,b}$	Differential horizontal force of a blade, N/m
$dF_{z,b}$	Differential vertical force of a blade, N/m
dL	Differential lift force of a blade, N/m
dM_x	Differential moment on center of gravity in X-axis, N
dM_y	Differential moment on center of gravity in Y-axis, N
dM_z	Differential moment on center of gravity in Z-axis, N
dT	Local thrust, N/m
$d\psi_{blade}$	Differential azimuth angle of a blade, rad

dy	Length of a blade element, m
E	Constant matrix of surrogate model
e_θ	Attitude error of pitch angle, rad
e_ϕ	Attitude of roll angle, rad
e_ψ	Attitude of yaw angle, rad
e_U	Velocity error of forward direction in body frame, m/s
e_V	Velocity error of side direction in body frame, m/s
e_{X_b}	Position error of forward direction in body frame, m
e_{Y_b}	Position error of forward direction in body frame, m
e_Z	Altitude error in inertial frame, m
$e_{\dot{Z}}$	Velocity error of vertical direction in inertial frame, m/s
$e_{\ddot{Z}}$	Acceleration error of vertical direction in inertial frame, m/s²
$\vec{F}_{prop}$	Aerodynamic forces on center of gravity, N
$\vec{F}_{drag}$	Drag force on a body frame, N
G	Change in the slope of the discharge curve of a battery cell due to current, Ω/Ah
g	Gravitational acceleration, m/s2
$H_{V_{wind}}$	Turbulence filter of von Kármán wind turbulence model
h	Flight altitude, ft
I_0	No-load current of a motor, A
I_a	Current of avionics, A
I_m	Current of a motor, A

I_{xx}	Moment of inertia about the X-axis, kg·m^2
I_{xy}	Product of inertia in the XY-plane, kg·m^2
I_{xz}	Product of inertia in the XZ-plane, kg·m^2
I_{yy}	Moment of inertia about the Y-axis, kg·m^2
I_{yz}	Product of inertia in the YZ-plane, kg·m^2
I_{zz}	Moment of inertia about the Z-axis, kg·m^2
K	Primary dependency of voltage on the capacity discharged, V/Ah
K_v	Speed constant of a motor, RPM/V
L	Distance between the center of gravity and each rotor's hub, m
L_T	Bar length from the center of gravity to an inner rotor, m
L_B	Bar length from an inner rotor to an outer rotor, m
L_u	Turbulence scale length in forward direction, ft
L_v	Turbulence scale length in side direction, ft
L_w	Turbulence scale length in vertical direction, ft
$\vec{M}_{prop}$	Moments on center of gravity, N·m
M_X	Moment in the X-axis, N·m
M_Y	Moment in the Y-axis, N·m
M_Z	Moment in the Z-axis, N·m
m	Mass, kg
N_b	Number of blades
N_{rotor}	Total number of rotors
P	Roll rate of a vehicle, rad/s

P_{Co}	Copper loss, W
P_{Ir}	Iron loss, W
P_i	Induced power, W
P_{Me}	Mechanical loss, W
P_o	Profile power, W
P_p	Parasite power, W
P_{St}	Stray loss, W
P_{elec}	Electric power of a motor, W
P_{mech}	Mechanical power of a rotor, W
Q	Pitch rate, rad/s
Q_b	Total capacity of a battery cell discharged up to the present instant, Ah
Q_i	Torque of ith rotor, N·m
$\boldsymbol{R}$	Rotation matrix
R	Yaw rate, rad/s
R_b	Resistance of a battery, Ω
R_{esc}	Resistance of an electric speed controller, Ω
R_m	Resistance of a motor, Ω
S	Control signal
T_i	Thrust of ith rotor, N
t_f	Total flight endurance, s
U	Ground speed of forward direction in body frame, m/s

$U_{P,disk}$	Vertical speed of a rotor disk, m/s
$U_{T,disk}$	Horizontal speed of a rotor disk, m/s
V	Ground speed of side direction in body frame, m/s
V_a	Airspeed speed in body frame, m/s
V_b	Voltage of a battery, V
V_{emf}	Motor electromotive force, V
V_m	Voltage of a motor, V
V_o	Open circuit voltage of a battery cell, V
V_{tip}	Tip speed of a rotor, m/s
V_{von}	Wind speed in von Kármán wind turbulence model, m/s
V_w	Wind speed in body frame, m/s
W	Ground speed of vertical direction in body frame, m/s
w	Rotation speed of a motor, rad/s
X	Forward direction in inertial frame
X$_{ref}$	Target path coordinate of forward direction in inertial frame, m
X_i	Distance between ith rotor's hub and center of gravity of X-axis in body frame, m
Y	Side direction in inertial frame
Y$_{ref}$	Target path coordinate of side direction in inertial frame, m
Y_i	Distance between ith rotor's hub and center of gravity of Y-axis in body frame, m
y	Distance between a hub and a blade element, m

Z	Vertical direction in inertial frame
Z_{ref}	Target path coordinate of vertical direction in inertial frame, m

Greek symbols

$\alpha_{disk,i}$	Angle of attack of a propeller disk, rad
$\alpha_{e,i}$	Effective angle of attack of a blade element, rad
κ	Induced power factor
θ	Pitch angle, rad
θ_{cmd}	Target pitch angle, rad
θ_{blade}	Twist angle of a blade element, rad
$\lambda_{inflow,i}$	Inflow ratio of a blade element
μ_i	Advance ratio of a propeller
ν	Kinematic viscosity, m^2/s
ρ	Air density, kg/m3
σ_u	Turbulence intensity in forward direction
σ_v	Turbulence intensity in side direction
σ_w	Turbulence intensity in vertical direction
ϕ	Roll angle, rad
ϕ_{cmd}	Target roll angle, rad
$\phi_{ind,i}$	Induced angle of a blade element, rad
ψ	Yaw angle, rad
ψ_{ref}	Heading angle, rad

ψ_{blade} Azimuth angle of a blade, rad

Subscripts

A	Altitude
a	Airspeed
avg	Average value
i	i^{th} rotor
P	Pitching attitude
R	Rolling attitude
Y	Yawing attitude
x	Forward direction in body frame
y	Side direction in body frame
z	Vertical direction in body frame

Abbreviations

6-DOF	Six-Degree-Of-Freedom
ADM	Actuator Disk Model
CFD	Computational Fluid Dynamics
CLOUDS	Conceptual Layout Optimization for Universal Drone Systems
ESC	Electric Speed Controller
EPS	Electric Propulsion System
FRRA	Front rotor's Retreating side and Rear rotor's Advancing side

eVTOL   Electric Vertical Take-Off and Landing

KARI   Korea Aerospace Research Institute

PID   Proportional-Integral-Derivative

RPM   Revolutions Per Minute

UAV   Unmanned Aerial Vehicle

UAM   Urban Air Mobility

VTOL   Vertical Take-Off and Landing

List of Figures

XVI

XVII

XVIII

List of Tables

Chapter 1.

Introduction

1.1   Overview of wingless-type eVTOL

Vertical take-off and landing (VTOL) aircrafts are widely used for various public and military sectors due to their advantage of not having to rely on runways. Various configurations of VTOL, such as tilt rotor, tilt wing, tilt jet, vectored thrust, tail sitter, lift+cruise, and tip jet, have been developed. The Vertical Flight Society[†] (VFS) in USA categorized various VTOL aircrafts and propulsion concepts as shown in Fig. 1-1.

Technology development of electric propulsion systems (EPSs), distributed propulsion, autonomous intelligence, and battery energy storage lead to the appearance of electric VTOL (eVTOL). While most conventional VTOLs are engine-based fuel-consuming propulsion systems, eVTOLs are based on electric propulsion system (EPS) composed of rotors, electric motors, and batteries. The VFS presented and categorized the main players and eVTOL models as shown in Fig. 1-2. In the category, the vectored thrust and lift+cruise eVTOLs usually have a fixed wing and multiple rotors, but the multirotor eVTOLs have only multiple rotors, so called wingless-type eVTOLs.

[†] https://vtol.org/

1
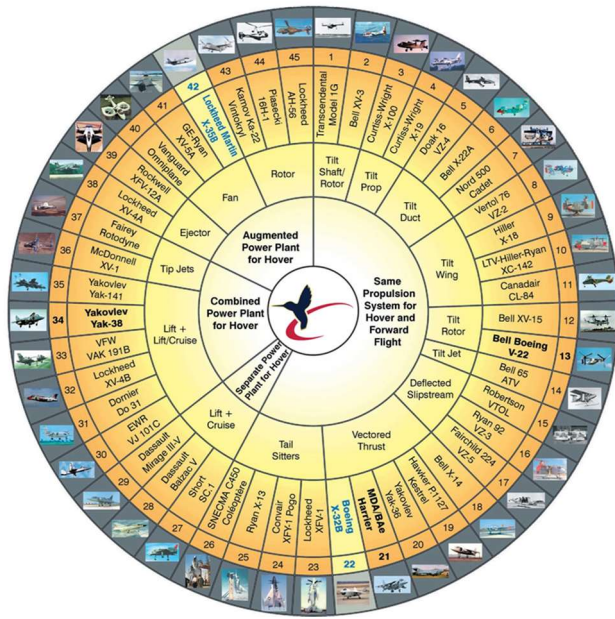
Fig. 1-1 V/STOL aircraft and propulsion concepts[†]

Fig. 1-2 Electric VTOL aircrafts[††]

[†] https://vtol.org/vstol/wheel.htm

[††] https://evtol.news/__media/PDFs/Hirschberg-eVTOL-Ames-2Jul2018.pdf

Among these eVTOL configurations, the wingless-type eVTOL has the advantages of efficient hover performance, low noisiness, and safety. As shown in Fig. 1-3, Volocopter, the representative configuration of the wingless-type eVTOL, has much lower disk loading than other VTOL models [1]. Due to the characteristic of the low disk loading, the wingless-type eVTOLs have high performance at hover and low loading noise. Also, there are many remaining rotors that can cope with failure of a rotor or a motor in the wingless-type eVTOL, so the fail-safe capability is great.
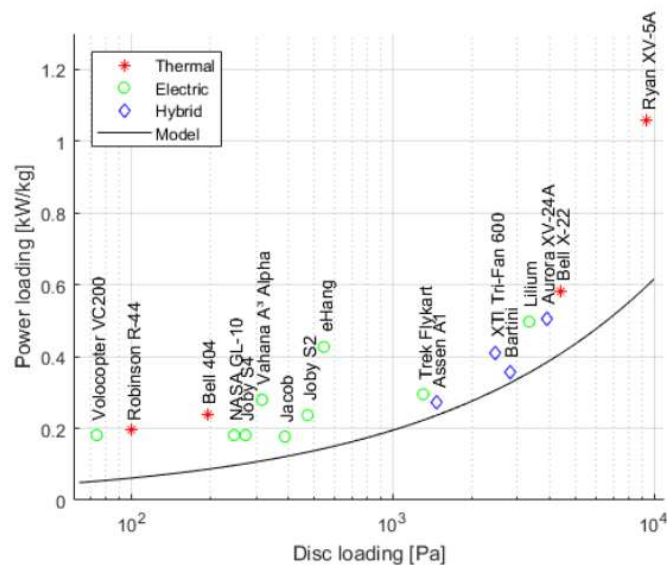
Fig. 1-3 Power and disk loading for various VTOLs [1]

From small size for unmanned aerial vehicle (UAV) to large size for urban air mobility (UAM) service, there are various size of wingless-type eVTOLs with respect to their mission operation. Wingless-type eVTOLs for small UAV are utilized

3

in logistics and delivery [2-11], search and rescue [12-15], military [16-17], agriculture [18-24], and inspection of structures [25-34]. In large size of wingless-type eVTOLs, they have been developed mainly for UAM service, such as Volocopter 2X, eHang 184, and CityAirBus models shown in Fig. 1-2. They are expected to be a suitable configuration for transportation point-to-point services within a city [35]. Among the models, a representative model of the wingless-type eVTOL is the VoloCity series produced by Volocopter GmbH. Among the models, the Volocopter 2X model was developed to provide an air taxi service for two passengers using a distributed EPS with 18 rotors. In 2021, the model received production organization approval in compliance with Part 21G of the European Union Aviation Safety Agency[†].

The wingless-type eVTOL controls the speed of its multiple rotors to maintain its ground speed and a stable attitude along a given flight path. The rotating speed of the rotors has to be changed continuously to achieve stable flight. Concurrently, the rotating speed and the loaded torque of the motors also continuously change. Therefore, to predict the overall flight performance of a wingless-type eVTOL, it is necessary to analyze the rotor thrust and torque with respect to the rotating speed of each rotor as assigned by the controller. Also, the electric power required by the motors is also necessary to be predicted based on the torque loaded to the motors to

---

[†]https://www.easa.europa.eu/newsroom-and-events/press-releases/easa-issues-first-approval-defined-drone-operations-volocopter

maintain the rotating speed. Through a series of multidisciplinary analyses of flight simulation, including control, rotor aerodynamics, and EPS analyses, it is possible to predict the flight performance of a wingless-type eVTOLs in ideally operating condition, such as calm wind and no aerodynamic interference between rotors.

For actual operation of the wingless-type eVTOLs, two issues have to be considered on its flight performance prediction: one is external wind and the other is rotor-rotor interference. In the case of wingless-type eVTOLs in small UAVs, their operations are easily affected by the external wind due to their relatively small size and low ground speed compared to wingless-type eVTOLs for UAM service. According to the report [36] which analyzed the impact of outdoor operation conditions on UAVs, the overall flight endurance of a 2 kg class quadrotor was reduced by up to 30% under 5 knot headwinds in forward flight. The winds cause thrust fluctuation in each rotor and frame drag, resulting in position and attitude errors. On the contrary, in the case of wingless-type eVTOLs for UAM service, rotor–rotor interference inevitably affects their flight performance, because their multiple rotors, usually over 10 rotors, are disposed within a limited rim size. Therefore, external wind effect for small UAV and rotor-rotor interference effect for UAM service are necessary to evaluate their flight performance in actual operation.

1.2   Previous studies about wingless-type eVTOL

The issues of the flight performance prediction of wingless-type eVTOLs in actual operation are three: 1) multidisciplinary analysis, 2) external wind of

wingless-type eVTOLs for small UAVs, and 3) rotor-rotor interference of wingless-type eVTOLs for UAM service. In this section, various previous studies related to flight performance prediction of wingless-type eVTOLs are introduced in those three categories.

1.2.1 Multidisciplinary analysis of control, aerodynamic, and EPS

Nandakumar et al. [37] suggested a new quadrotor configuration using overlapped rotor disk with height offset and showed more increased flight endurance than the conventional configuration. However, the overall flight endurance measured in the actual flight test under the wind condition was more reduced by up to 6 minutes than the endurance predicted by simulations, since the simulation assumed calm wind condition. Bershadsky et al. [38] developed a wingless-type eVTOL performance analysis tool, EMST, and presented rotor aerodynamic and circuit analyses of the electric propulsion system. The validity of the analysis tool was demonstrated by comparing the flight test data of several commercial quadrotors with the analysis results. However, EMST has a limitation in that the motor efficiency is considered constant rather than varying with the flight conditions.

Tools such as flyEval [39] and Conceptual Layout Optimization of Universal Drone Systems (CLOUDS) [40, 41] were developed to overcome this limitation. Shi et al. [39] developed flyEval for evaluating flight performance by calculating the motor efficiency according to flight conditions based on the specifications of the electrical system components such as motors, ESCs, and batteries. However, the tool

6

could design a wingless-type eVTOL only for preassigned mission profiles such as acrobatic flight, aerial photography, heavy load, and package delivery. CLOUDS used an analysis technique similar to that of flyEval, but it could estimate the performance based on the specified mission profile. Further, it derived the optimal design of the wingless-type eVTOL for small UAVs required for a specific mission through optimization processes such as sequential least squares programming and genetic algorithm using the OpenMDAO [42] framework. The validity of the performance analysis method used in CLOUDS was demonstrated by comparing the actual flight test data of several commercial quadrotors with the analysis results. Furthermore, an actual quadrotor was manufactured, and flight test demonstrated the feasibility and capability of CLOUDS in [43]. However, it also has a limitation in that it cannot predict the flight performance induced by the instantaneous position and attitude changes due to the winds.

Concerning the flight performance analysis studies of wingless-type eVTOLs for UAM service, Pradeep et al. [44] devised a mode of operation that minimized the amount of energy required for each landing speed and various tops of descent in a cruise mission by a coaxial quadrotor eVTOL, the eHang 184 model. Based on momentum theory with the control variable of rotor thrust, the required mechanical power was analyzed and a fixed-final-time multiphase optimal control problem was solved. However, due to the lack of consideration of the EPS, the method was insufficient to predict the flight performance such as the electric power required by motors and batteries. To predict the amount of energy stored in the batteries, Pradeep

7

et al. [45] further developed energy-based and electrochemical-based battery models. The amount of battery energy required for various cruise speeds, altitudes, climb profiles, ranges, and required time of arrival of the quadrotor eVTOL was determined. However, the power stored in the battery was only induced to the mechanical power needed for the rotors and did not include the power lost by the motors and electric speed controllers.

Kadhiresan et al. [46] found an optimized design that minimized the total weight of a helicopter, wingless-type, lift+cruise, tilt-rotor, and tilt-wing configurations flying within an area of 50 square feet. Although the weight of the EPS was estimated, this method for predicting the flight performance is limited due to the absence of an analysis of the EPS. Michel et al. [47] predicted the flight performance of an octorotor eVTOL by analyzing the rotor aerodynamics and the EPS using the pulse-width modulation signal of each rotor. The rotor aerodynamics was based on blade element theory with the inflow model of momentum theory. Since the control signal was fixed without control feedback, this method was insufficient to predict flight performance in actual operation. Hendricks et al. [48] developed a multidisciplinary design optimization framework for a quadrotor eVTOL. They derived the minimum total weight using design variables such as operation range, allowable temperature and energy density of the batteries, and the diameter of the rotors. In addition, a temperature control system for the batteries, consisting of a puller fan, nozzle, coolant reservoir, and pump, was considered in the design process. However, the

design was solely available to quadrotor eVTOLs and rotor–rotor interference was not induced.

Kim et al. [49] developed a multidisciplinary framework for simulating flight performance. It had control, rotor aerodynamics, and EPS analysis modules. This work was a predecessor of this paper. The framework predicted the rotor speed using a cascade PID controller and rotor aerodynamic forces using blade element theory with a linear inflow model. In addition, the power required by the loaded motors and the battery energy required to maintain the rotor speed were predicted. However, the framework lacked generality and could not be applied to a representative eVTOL alike Volocopter. Moreover, rotor–rotor interference was not induced.

1.2.2 External wind of wingless-type eVTOLs for small UAVs

To improve the control performance of a quadrotor in crosswind environments, Ding et al. [50] developed a control algorithm in which small overshoots occur even under crosswind environments where the quadrotor was flying upward to reach the target altitude. However, one major limitation was the lack of clarity regarding position errors under various wind directions as the study focuses on reducing position errors only under crosswind conditions. Using the Dryden wind model [51] for simulating the turbulence characteristics of external wind in a more realistic environment, Massé et al. [52] compared the linear quadratic regulator with the structured H-infinity control technique and showed that structured H-infinity control exhibits better control performance in turbulent wind conditions. Wang et al. [53]

9

suggested a robust and adaptive control strategy for a quadrotor under the wind condition using von Kármán wind turbulence model and showed that the quadrotor under the wind well followed the given path despite a sudden payload mass change. Lei et al. [54] measured thrust and power for a pair of rotors with respect to spacing ratios and disk plane angles and showed that a back-to-back pair of rotors showed increased tendency for wind resistance.

Including other studies [55-65] related to control performance improvement, these studies partially noted on enabling a quadrotor to fly under external winds with a stable attitude, but they did not note the excess battery energy consumed for attitude corrections leading to reduction of the overall flight performance.

1.2.3 Rotor-rotor interference of wingless-type eVTOLs for UAM

Miesner et al. [66] conducted an aerodynamic analysis of a Volocopter 2X model with a trimmed rotor speed using FLOWer, a computational fluid dynamics (CFD) code developed by DLR, and VFAST, which combined flight dynamics with blade element momentum theory. This high-fidelity aerodynamic analysis can deal with a high density of small vortices, based on loose coupling with the trim analysis code. Although it can appropriately analyze the aerodynamic forces for specific instantaneous flight conditions, this type of high-fidelity analysis is hardly applicable to predicting the flight performance over an entire flight time of several tens of minutes under various operating conditions.

Johnson et al. [67] used NDARC, CAMRAD 2, and ANOPP 2 to estimate the total weight and to analyze the rotor aerodynamic force, EPS, and handling quality of a quiet single-main-rotor helicopter, a side-by-side helicopter, a multirotor, and lift+cruise configurations. They emphasized that the aerodynamic characteristics changed due to rotor–rotor interference, which should be considered when analyzing or designing a multirotor eVTOL. It was suggested that the power required by the rear rotor decreased as the vertical position of that rotor was increased.

Misiorowski et al. [68] and Hwang et al. [69] analyzed rotor–rotor interference for the plus and cross configurations of a small quadrotor unmanned aerial vehicle (UAV). For the plus configuration, this interference increased the thrust of the intermediate rotors and decreased the thrust of the rear rotor, compared with an isolated rotor. For the cross shape, the thrust of both rear rotors was lower compared with an isolated rotor. These studies were conducted in the condition of a fixed rotor speed. In the actual operation of a wingless-type eVTOL, since the speed of each rotor changes continuously, it is necessary to predict the rotor speed as it changes due to control feedback and the 6-DOF dynamics.

Usov et al. [70] analyzed rotor-rotor interference for front and rear rotors in a straight line. The proposed model to predict the rotor-rotor interference was based on Beddoes prescribed wake geometry. The numerical results showed that thrust of the rear rotor was reduced due to the additional inflow of the rear rotor by the inflow from the front rotor. However, the model was only available at advance ratios over 0.15 due to the limitation of the Beddoes' generalized wake. Also, the numerical

11

results were based on only front and rear rotors in straight. In wingless-type eVTOLs for UAM service, their rotors would be usually disposed in straight, diagonal, or side-by-side.

In other studies [71-78] related to rotor-rotor interference, the rotor aerodynamic force was analyzed based only on a specific configuration for the rotor rotation directions in these studies of rotor–rotor interference. Even if the rotation directions ensure that torque trim is satisfied in hover flight, they are not uniquely determined. Because the effect of rotor–rotor interference on flight performance depends on the rotation directions, it is assumed that there exists an optimal rotation direction for a given lot of multiple rotors in actual operation. Therefore, it is essential to investigate rotor–rotor interference for various rotation direction and the resulting flight performance.

1.3   Motivation and scope of the dissertation

The methodologies to predict the flight performance of a wingless-type eVTOL in the previous studies mainly focused on the steady level flight conditions, but the methodologies were still limited to consider the flight performance including the control for the wind and rotor-rotor interference disturbances. To maintain a stable operation of the wingless-type eVTOL under the disturbances, the rotational speed of the rotors is constantly controlled, and the change in the rotation speed affects the flight performance, consequently. Therefore, concurrent analyses of rotation speed of rotors for the trimmed condition for the disturbances, aerodynamic forces with

varying the rotation speed, and electric propulsion performance with varying the loaded torque on the motors are necessary to predict the flight performance of a wingless-type eVTOL operating in the disturbances.

In the previous studies about a wingless-type eVTOL for small UAV, control characteristics under the wind disturbance were mainly improved its flight performance was greatly affected by the disturbance due to its small size and low ground speed. However, it is still needed to investigate how much flight performance is reduced due to the wind disturbance and what are the main characteristics of the operation in the disturbance. In addition, although the flight performance determined by the specifications of the rotors, motors, and batteries, only the maximum flight speed is currently presented as a specific indicator for evaluating wind resistance of a wingless-type eVTOL.

In the previous studies about a wingless-type eVTOL for UAM service, aerodynamic characteristics were analyzed based on a specific rotation speed and direction of rotors, considering rotor-rotor interference. However, there are various combinations of rotation directions that can be used. It is still needed to investigate how much the flight performance is changed with respect to the rotation directions in trimmed condition for the rotor-rotor interference.

In summary, three research questions of this dissertation were derived from the limitations of the previous studies, as below.

1. *Is it possible to predict flight performance of a wingless-type eVTOL including the control for the disturbances such as external winds and rotor-rotor interference?*

2. *What are the characteristics of the flight performance of a wingless-type eVTOL for small UAV including the control for wind disturbance? Is there a standard for evaluating the wind resistance characteristics of it?*

3. *Is there a desirable combination for the rotation direction of multiple rotors in a wingless-type eVTOL for UAM service?*

To overcome the limitations of previous studies and answer those research questions, this study aims to develop a flight simulation framework for wingless-type eVTOLs, based on the multidisciplinary analysis including the control for the disturbances of external wind and rotor-rotor interference. After that, the tendency of excess battery energy and operable wind conditions is identified with respect to ground speed and wind speed of a wingless-type eVTOL for small UAV. Finally, variations in flight performance and operation range with respect to rotor rotation directions are predicted to investigate the desirable rotation direction of a wingless-type eVTOL for UAM service.

This paper is organized as follows:

In Chapter 2, layout and each analysis module of the flight simulation framework are outlined. Also, details of cascade PID control, aerodynamic, EPS, 6-DOF dynamics, and two add-on modules for actual operation is described.

In Chapter 3, the developed simulation framework is validated, comparing the numerical results from the framework with the results from experiments and numerical analysis of Free-Vortex Wake (FVW) and high-fidelity computational fluid dynamics (CFD).

In Chapter 4, flight performance of a wingless-type eVTOL for small UAV under external wind condition is numerically investigated. Operable wind condition with respect to ground speeds and excess battery energy for operation under the wind are also investigated.

In Chapter 5, flight performance of a wingless-type eVTOL for UAM service considering rotor-rotor interference is numerically investigated. A new desirable concept of rotor rotation direction is suggested and compared with another rotation direction of unfavorable rotor-rotor interference.

Finally, the conclusion of this paper is given in Chapter 6.

Chapter 2.

Simulation Framework

2.1   Layout and analysis modules in simulation framework

By inputting a target path, flight conditions, and the specification of a wingless-type eVTOL, the flight simulation framework can predict its flight performance such as rotor thrust and mechanical power, motor drive current and required electric power, and consumed battery energy along the target path. As shown in Fig. 2-1, the overall procedures are 4 steps:

Step 1. The difference between the current position and the target path at each time step of the simulation is input to the cascade PID control analysis module, which calculates an adjustment to the rotational speed of each rotor to compensate for the position and attitude errors.

Step 2. The required rotational speed of each rotor is input to the aerodynamic analysis module, which calculates an adjustment to the thrust and mechanical power of each rotor.

Step 3. The new thrust and mechanical power of each rotor are input to the 6-DOF dynamics analysis module, which calculates an updated position and attitude at the end of the time step.

Step 4. The rotational speed and mechanical power of each rotor are input to the electric propulsion system (EPS) analysis module, which calculates the motor

driving current, the electric power required, and the battery energy consumed in the corresponding time step.

Iterating these steps over whole the target path, it is possible to predict the trajectory and the flight performance.
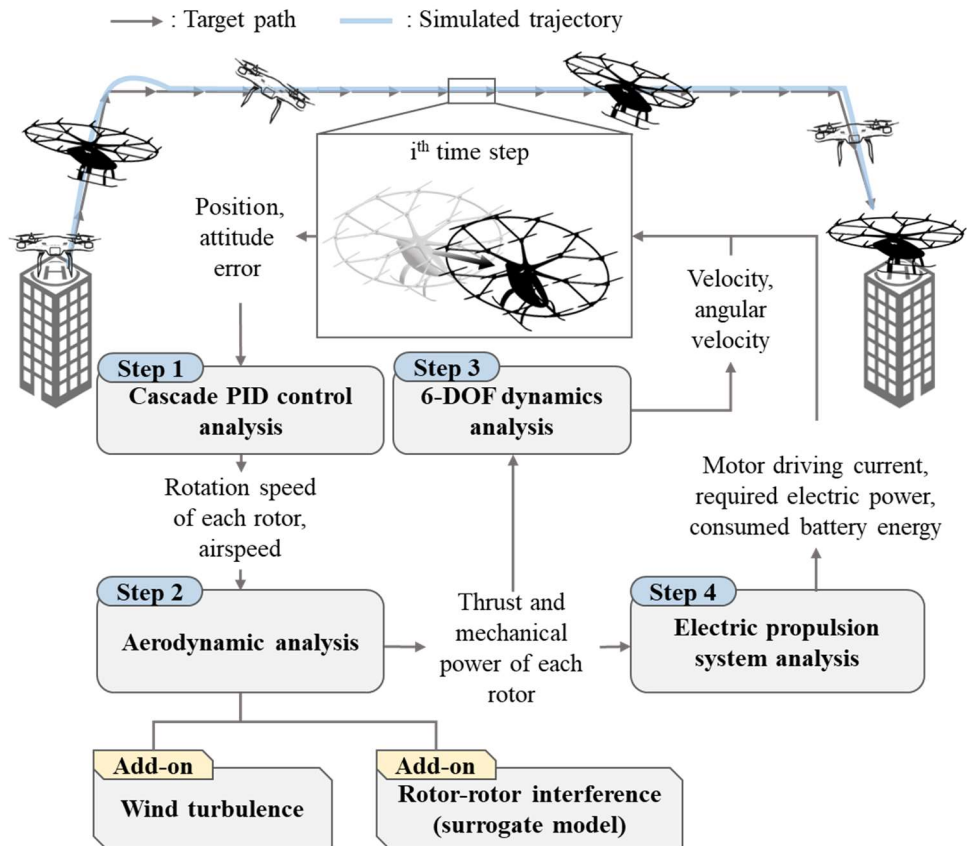
Fig. 2-1 Layout and modules in flight simulation framework

The analysis modules of cascade PID control, 6-DOF dynamics, and EPS are available for general wingless-type eVTOLs from 4 rotors (quadrotor) to more than 10 rotors. To predict the flight performance in actual operation, two add-on modules

for the aerodynamic analysis module are necessary with respect to the size of the wingless-type eVTOL.

In the case of small-scale wingless-type eVTOLs, the wind turbulence add-on is needed to predict the flight performance of them in actual operation. The representative configuration of them is a quadrotor and its flight performance under various external winds would be analyzed in this paper. In the case of large-scale wingless-type eVTOLs, the rotor-rotor interference add-on is needed to predict the flight performance of them in actual operation. The representative configuration of them is a configuration similar with Volocopter (18 rotors) and its flight performance affected by rotor-rotor interference would be analyzed in this paper.

Details in the analysis modules and add-on modules are presented in following sections.

2.1.1 Cascade PID control module

The cascade PID control algorithm is based on ArduCopter which is widely used in the flight control of wingless-type eVTOLs. In this paper, a control algorithm used in the simulation was developed and similar to the cascade PID control of ArduCopter to predict the position and attitude errors of wingless-type eVTOLs. The overall flow of the control algorithm is shown in Fig. 2-2. The inputs of the algorithm are heading ψ_{ref}, horizontal target path X_{ref}, Y_{ref}, and altitude Z_{ref}. After proportional control for the horizontal position errors of e_{X_b} and e_{Y_b} and PID control for the speed errors of e_U and e_V, the target roll angle ϕ_{cmd} and pitch angle θ_{cmd} for attitude control were calculated. In altitude control, proportional control for altitude error e_Z and vertical speed error $e_{\dot{Z}}$, and PID control for vertical acceleration error $e_{\ddot{Z}}$ were conducted. In attitude control, proportional controls for the error of roll angle e_ϕ and the error of pitch angle e_θ were conducted. From the target heading, proportional control for the yaw angle error e_ψ was also conducted.
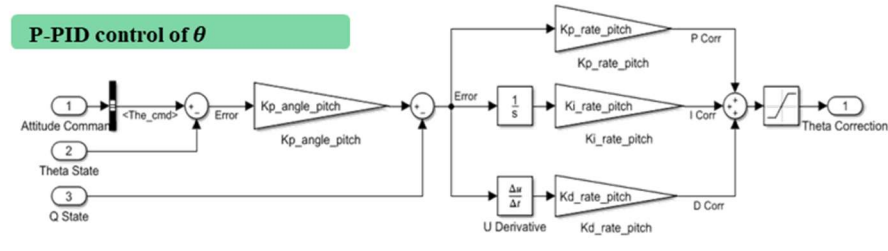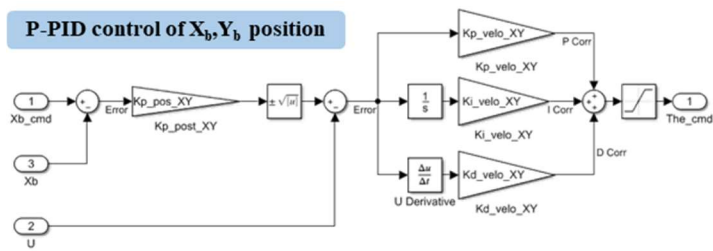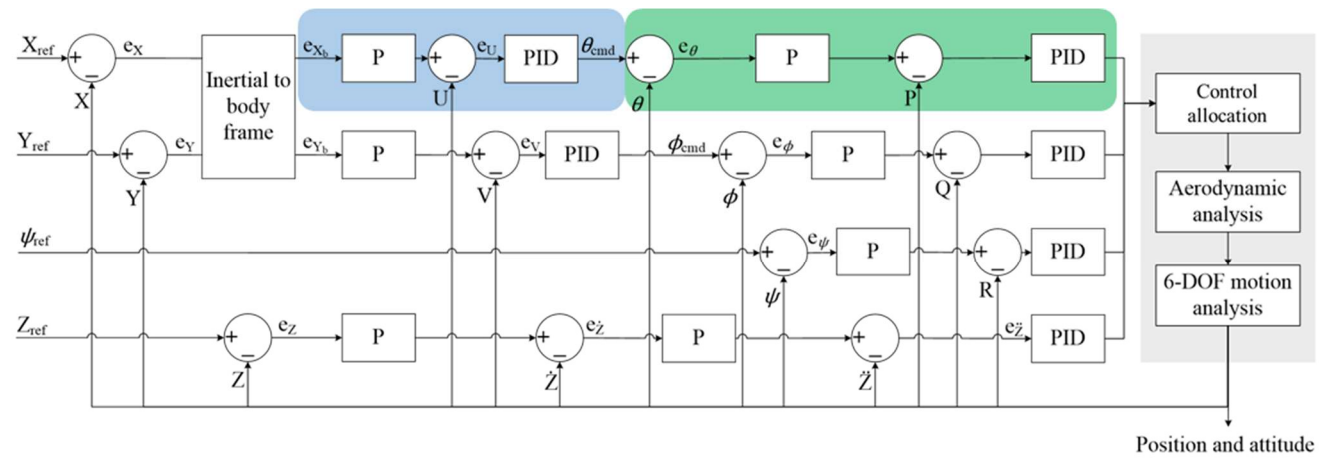
Fig. 2-2 Cascade PID control block diagram in Matlab Simulink

20

The cascade PID control algorithm was generic and it could be applicable on many configurations of wingless-type eVTOLs. However, it should be noted that control allocation is dependent on the number and position of motors. In this paper, two representative configurations in wingless-type eVTOLs were investigated to predict their flight performance: 1) Quadrotor (4 motors) and 2) Volocopter-type eVTOL (18 motors).

For a quadrotor, allocating a rotational speed to each motor to control the flight is always unique because each of the four motors has its own control inputs of rolling, pitching, yawing, and altitude. However, there are various control allocation strategies for the four control inputs when the number of motors are more than six. Of the various control allocation, PX4 is used for hexarotor UAVs. It is a widely used open source-based autopilot software program. PX4 assigns a speed to a motor that is proportional to the distance between the motor and the center of gravity[†].

Among many available control strategies, a control strategy inspired by the control allocation of PX4 that set the speed of a motor proportional to its horizontal distance from the center of gravity was adopted. The control strategy can be applied to an aircraft with any number of motors. The present study analyzes the control of an aircraft with 18 driving motors, which is similar to a representative wingless-type eVTOL, the Volocopter 2X. Thus, S_P, S_R, S_Y, and S_A, which are the result of cascade PID control, are control signals for pitching, rolling, yawing, and altitude,

---

[†] https://www.mathworks.com/help/supportpkg/px4/ug/plant-attitude-px4-hexacopter.html (Accessed 17 August 2021)

21

respectively. As shown in Fig. 2-3, when the distance from each motor to the pitching plane is $X_{1,2,3,4}$ and the distance to the rolling plane is $Y_{1,2,3,4}$, the control signal received from each motor is shown in Table 2-1.
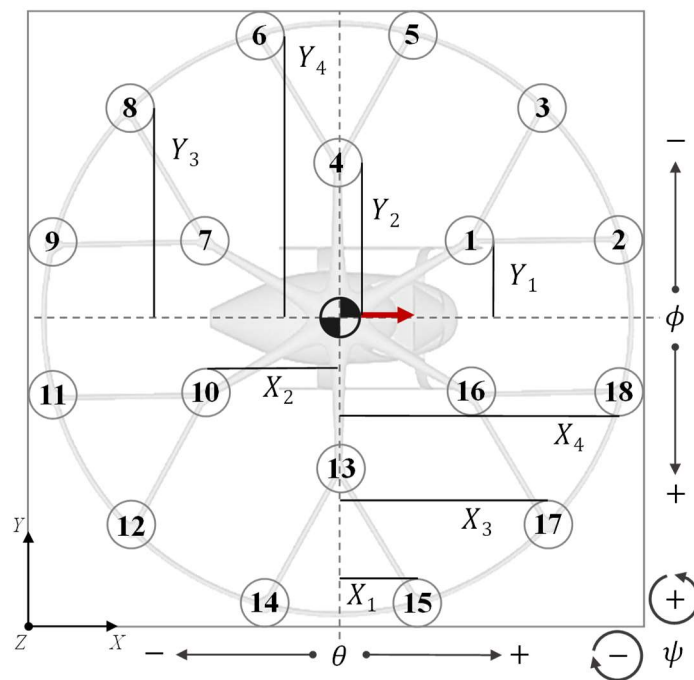
Fig. 2-3 Horizontal distances from the center of gravity to each motor in body frame

Table 2-1. Control allocation for each motor

Rotor number	Allocated control signal (± depends on the rotation direction)
1	$- S_P (X_2 / X_4) + S_R (Y_1 / Y_4) \pm S_Y + S_A$
2	$- S_P + S_R (Y_1 / Y_4) \pm S_Y + S_A$
3	$- S_P (X_3 / X_4) + S_R (Y_3 / Y_4) \pm S_Y + S_A$
4	$S_R (Y_2 / Y_4) \pm S_Y + S_A$
5	$- S_P (X_1 / X_4) + S_R \pm S_Y + S_A$
6	$S_P (X_1 / X_4) + S_R \pm S_Y + S_A$
7	$S_P (X_2 / X_4) + S_R (Y_1 / Y_4) \pm S_Y + S_A$
8	$S_P (X_3 / X_4) + S_R (Y_3 / Y_4) \pm S_Y + S_A$
9	$S_P + S_R (Y_1 / Y_4) \pm S_Y + S_A$
10	$S_P (X_2 / X_4) - S_R (Y_1 / Y_4) \pm S_Y + S_A$
11	$S_P - S_R (Y_1 / Y_4) \pm S_Y + S_A$
12	$S_P (X_3 / X_4) - S_R (Y_3 / Y_4) \pm S_Y + S_A$
13	$- S_R (Y_2 / Y_4) \pm S_Y + S_A$
14	$S_P (X_1 / X_4) - S_R \pm S_Y + S_A$
15	$- S_P (X_1 / X_4) - S_R \pm S_Y + S_A$
16	$- S_P (X_2 / X_4) - S_R (Y_1 / Y_4) \pm S_Y + S_A$
17	$- S_P (X_3 / X_4) - S_R (Y_3 / Y_4) \pm S_Y + S_A$
18	$- S_P - S_R (Y_1 / Y_4) \pm S_Y + S_A$

If acceleration is required in the forward direction, the 2nd, 9th, 11th, 18th motors, which are farthest from the pitching plane, can generate a pitching moment greater than the other motors, even with the same thrust. Table 1 shows that when the control signal S_P is positive, the rotational speeds of the 2nd and 18th motors are reduced the most and the rotational speeds of 9th and 11th motors are increased the most. The same applies also to the rolling plane. In the yawing plane, the rotational speed changes with respect to the rotation direction of the motor.

After the control allocation, the analyses of aerodynamic forces for rotors and 6-DOF motion were carried out. The outputs of the 6-DOF motion analysis were position, velocity, acceleration, attitude angle, and angular velocity. These output

values would be feedback in the next time step of the simulation. The cascade PID control algorithm was implemented with Matlab Simulink version R2019b. The list of PID gain values was shown in Appendix-A, and these values were manually tuned for quadrotors to follow a designated path line well.

2.1.1 Aerodynamic analysis module

The required rotation speed of each motor calculated by the cascade PID controller was used as the input value for aerodynamic analysis, and then the thrust and mechanical power were calculated. The vertical force $dF_{z,b,i}$ and horizontal force $dF_{x,b,i}$ of a blade element shown in Fig. 2-4 were calculated through the blade element theory and linear inflow model [51] presented in this section. It should be noted that the linear inflow model is difficult to consider rotor-rotor interference. The aerodynamic analysis module is available for wingless-type small UAVs, not for the wingless-type eVTOLs for UAM service. The rotor-rotor interference is more dominant to wingless-type eVTOLs for UAM service than wingless-type small UAVs, because multiple rotors over 10 are disposed within a limited rim size. Therefore, the rotor aerodynamic analysis considering the rotor-rotor interference is presented in Section 2.2.2.

The freestream velocity on a blade element V_{element} is the sum of three velocities induced by: 1) translating and rotating motion of a quadrotor, 2) wind, and 3) rotating rotor. By integrating vertical forces $dF_{z,b}$ and horizontal forces $dF_{x,b}$ on the blade elements, thrust and mechanical power of rotors are calculated through

24

aerodynamic analysis. When a quadrotor operates under the winds, these element

forces fluctuate due to control for the position and attitude errors caused by the winds.
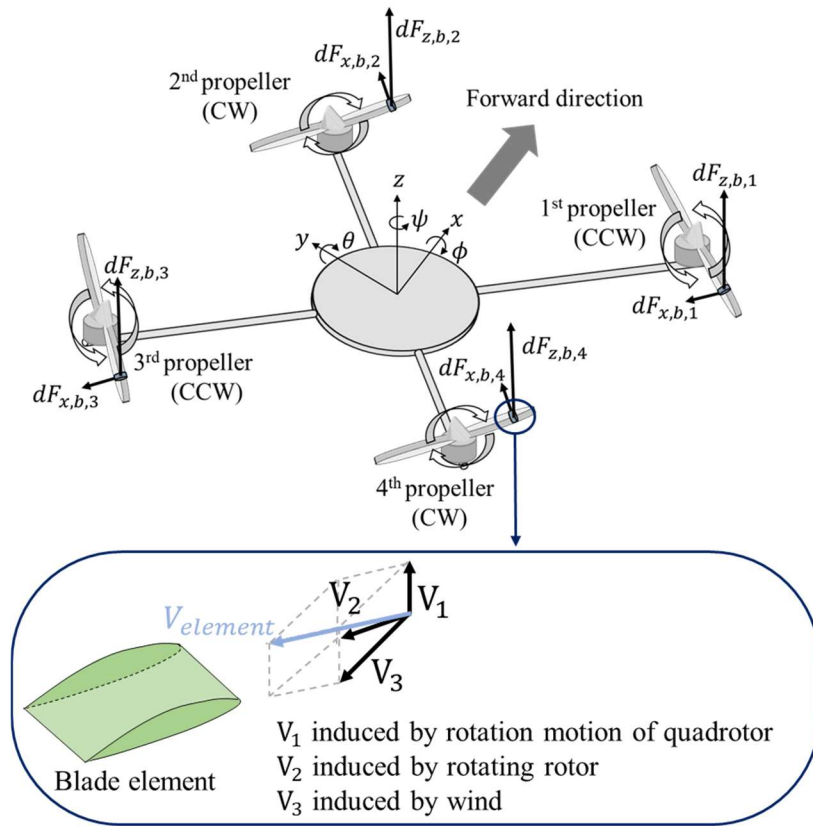
Fig. 2-4 Body frame of a quadrotor and forces on blade elements

Velocities $V_{a_{x,i}}$, $V_{a_{y,i}}$, and $V_{a_{z,i}}$ at each ith rotor's hub are the airspeed in body

frame and L is the distance between the center of gravity and each rotor's hub. The

airspeed is the velocity between the ground speed in body frame U, V, W, wind

speed in body frame V_{w_x}, V_{w_y}, V_{w_z} and angular velocities of the vehicle, as shown

in Eq. (1) and (2).

$$
\begin{bmatrix} X_1, Y_1 \\ X_2, Y_2 \\ X_3, Y_3 \\ X_4, Y_4 \end{bmatrix} = \begin{bmatrix} \dfrac{L}{\sqrt{2}}, -\dfrac{L}{\sqrt{2}} \\ \dfrac{L}{\sqrt{2}}, \dfrac{L}{\sqrt{2}} \\ -\dfrac{L}{\sqrt{2}}, \dfrac{L}{\sqrt{2}} \\ -\dfrac{L}{\sqrt{2}}, -\dfrac{L}{\sqrt{2}} \end{bmatrix} \tag{1}
$$

$$
\begin{bmatrix} V_{a_{x,i}} \\ V_{a_{y,i}} \\ V_{a_{z,i}} \end{bmatrix} = \begin{bmatrix} -U + Y_i R + V_{w_x} \\ -V + X_i R + V_{w_y} \\ -W - Y_i P + X_i Q + V_{w_z} \end{bmatrix} \tag{2}
$$

Inflow $\lambda_{inflow,i}$ of the blade element of the ith rotor with tip speed $V_{tip,i}$ at horizontal velocity $U_{Ti,disk}$, vertical velocity $U_{Pi,disk}$, angle of attack α_{disk}, advance ratio μ_i, and thrust coefficient C_T of each rotor is calculated by Eq. (3) to (5) during forward flight.

$$
\begin{bmatrix} U_{Ti,disk} \\ U_{Pi,disk} \end{bmatrix} = \begin{bmatrix} \sqrt{V_{a_{x,i}}^2 + V_{a_{y,i}}^2} \\ V_{a_{z,i}} \end{bmatrix} \tag{3}
$$

$$
\begin{bmatrix} \alpha_{disk,i} \\ \mu_i \end{bmatrix} = \begin{bmatrix} \tan^{-1} \dfrac{U_{Pi,disk}}{U_{Ti,disk}} \\ \dfrac{U_{Ti,disk}}{V_{tip,i}} \end{bmatrix} \tag{4}
$$

$$
\lambda_{inflow,i} = \mu_i \tan\left(\alpha_{disk,i}\right) + \dfrac{C_T}{\sqrt{\mu_i^2 + \lambda_{inflow,i}^2}} \tag{5}
$$

In the blade element of the ith rotor, the vertical velocity U_{Pi} and horizontal velocity U_{Ti} are represented by Eq. (6).

$$\begin{bmatrix} U_{P1}, U_{T1} \\ U_{P2}, U_{T2} \\ U_{P3}, U_{T3} \\ U_{P4}, U_{T4} \end{bmatrix} = \begin{bmatrix} -P|Y_1| - Q|X_1| + W + V_{tip,1}\lambda_{inflow,1}, w_1 r \\ P|Y_2| - Q|X_2| + W + V_{tip,2}\lambda_{inflow,2}, w_2 r \\ P|Y_3| + Q|X_3| + W + V_{tip,3}\lambda_{inflow,3}, w_3 r \\ -P|Y_4| + Q|X_4| + W + V_{tip,4}\lambda_{inflow,4}, w_4 r \end{bmatrix} \tag{6}$$

Induced angle $\phi_{ind,i}$ and effective angle of attack α_e of the blade element are calculated using Eq. (7) and (8) from blade twist angle θ_{blade}.

$$\phi_{ind,i} = \tan^{-1} \frac{U_{P,i}}{U_{T,i}} \tag{7}$$

$$\alpha_{e,i} = \theta_{blade} - \phi_{ind,i} \tag{8}$$

Using Eq. (9) with air density ρ and chord length c_r, local lift dL_i and drag dD_i on the element are calculated.

$$\begin{bmatrix} dL_i \\ dD_i \end{bmatrix} = \begin{bmatrix} \frac{1}{2} C_l \rho (U_{T,i}^2 + U_{P,i}^2) c_r \ dy \\ \frac{1}{2} C_d \rho (U_{T,i}^2 + U_{P,i}^2) c_r \ dy \end{bmatrix} \tag{9}$$

Lift coefficient C_l and drag coefficient C_d of the airfoil are calculated using the Reynolds number and effective angle of attack of the airfoil. In this paper, the coefficients based on Clark-Y airfoil were calculated using X-foil analysis. From

27

dL_i and dD_i, vertical force $dF_{z,b,i}$ and horizontal force $dF_{x,b,i}$ on the element are calculated using Eq. (10).

$$\begin{bmatrix} dF_{z,b,i} \\ dF_{x,b,i} \end{bmatrix} = \begin{bmatrix} dL_i \cos(\phi_{ind,i}) - dD_i \sin(\phi_{ind,i}) \\ dL_i \sin(\phi_{ind,i}) + dD_i \cos(\phi_{ind,i}) \end{bmatrix} \tag{10}$$

The forces on blade elements would be input at 6-DOF dynamics analysis module.

The body frame drag was calculated using Eq. (11) and (12) with air density ρ, the distance between adjacent motors D_L, frame drag coefficient C_D, and airspeed V_a on the body frame.

$$\begin{bmatrix} V_{a_x} \\ V_{a_y} \\ V_{a_z} \end{bmatrix} = \begin{bmatrix} -U + V_{w_x} \\ -V + V_{w_y} \\ -W + V_{w_z} \end{bmatrix} \tag{11}$$

$$\vec{F}_{drag} = \frac{1}{2}\rho D_L{}^2 \begin{bmatrix} C_{D_x} V_{a_x}{}^2 \\ C_{D_y} V_{a_y}{}^2 \\ C_{D_z} V_{a_z}{}^2 \end{bmatrix} \tag{12}$$

The drag coefficient of the body frame was derived from wind tunnel test data obtained by Korea Aerospace Research Institute (KARI) with respect to the Reynolds number and pitch angle of a DJI Matrice-100 model, which was one of the common configurations of quadrotors. The aerodynamic moment of the frame was neglected, assuming that the rotor thrust deviation to be compensated for the moments was insignificant.

To operate a quadrotor under the winds, required mechanical power consists of three powers: induced power P_i, profile power P_o, and parasite power P_p. The induced power is used to maintain rotating speed of rotors with induced drag due to finite blades. The profile power is also used to maintain the rotating speed with skin friction drag on airfoil. The parasite power is used to maintain the ground speed with frame drag due to the airspeed. Until the end of the flight, each time averaged power was defined in Eq. (13) to (15). As rotor aerodynamic analysis parameters, induced power factor κ is 1.1 and the number of blades N_b is 2. The meaning of t_f, y, and $d\psi_{blade}$ are total flight time, the distance between a hub and a blade element, and the differential azimuth angle of a blade, respectively. The value of induced power factor was selected by static thrust and torque experiment of a small UAV rotor in Section 3.1 in this paper. Also, the rotational speeds of rotors w_i were calculated by the cascade PID control module.

$$P_i = \frac{1}{t_f} \int_0^{t_f} \sum_{i=1}^{4} \frac{N_b}{2\pi} \int \int \kappa \ dL_i \sin(\phi_{ind,i}) \ w_i y \ d\psi_{blade} \ dt \tag{13}$$

$$P_o = \frac{1}{t_f} \int_0^{t_f} \sum_{i=1}^{4} \frac{N_b}{2\pi} \int \int dD_i \cos(\phi_{ind,i}) w_i y \ d\psi_{blade} \ dt \tag{14}$$

$$P_p = \frac{1}{t_f} \int_0^{t_f} \vec{F}_{drag} \cdot V_a \ dt \tag{15}$$

2.1.2 Electric propulsion system analysis module

The electric power and driving current of each motor and the battery energy consumed are calculated in the EPS analysis module using as input the rotational speed of each motor as calculated by the cascade PID control analysis module and the mechanical power of each rotor as calculated by the aerodynamic analysis module. The circuit of EPS is illustrated in Fig. 2-5. Through the circuit analysis, the motor driving voltage was calculated using Eq. (16) and (17), and the duty ratio of each motor D_{t_i} which was the ratio of the rotational speed of a loaded motor to the speed of an unloaded motor, was calculated using Eq. (18). In Eq. (16) to (18), V_{m_i}, V_b, R_b, I_{m_i}, R_{esc}, w_i, R_m, and K_v are motor drive voltage, duty ratio, battery voltage, battery resistance, motor drive current, ESC resistance, rotational speed of the motor, motor resistance, and speed constant of motor, respectively.

$$V_{m_i} = V_b - \left(\sum_{i=1}^{N_{rotor}} I_{m_i} + I_a \right) R_b - I_{m_i} R_{esc} \tag{16}$$

$$V_{m_{i_{avg}}} = D_{t_i} V_b - \left(\sum_{i=1}^{N_{rotor}} I_{m_i} + I_a \right) R_b - I_{m_{i_{avg}}} R_{esc} \tag{17}$$

$$D_{t_i} = \frac{2\pi w_i}{60 \left(V_{m_i} - I_{m_i} R_m \right) K_v} \tag{18}$$
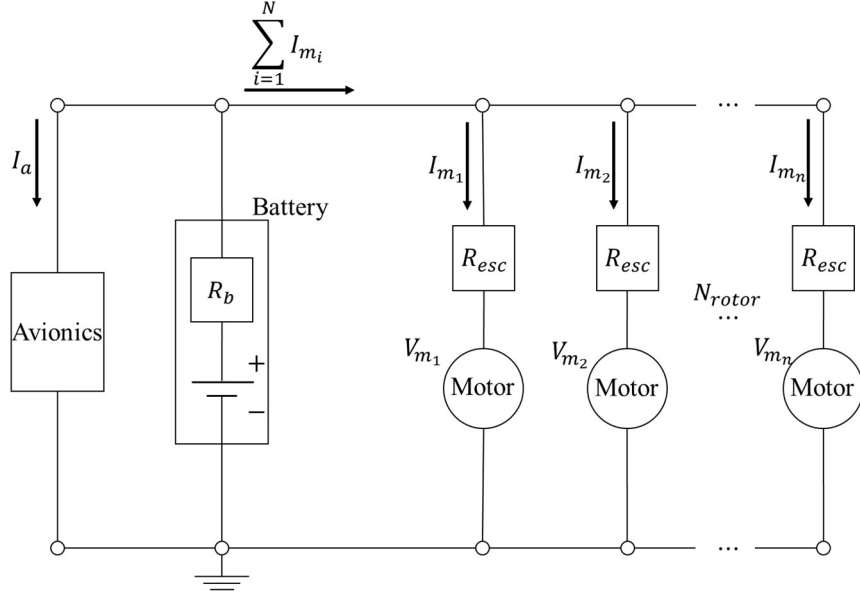
Fig. 2-5 Schematic of electric propulsion system circuit

The aerodynamic drag of each rotor was loaded as the mechanical power of each motor. Further, the electrical power of each motor was calculated using Eq. (19), considering four power losses. These power losses are copper loss P_{Co} caused by heating of the copper wire owing to internal resistance, iron loss P_{Ir} caused by magnetic hysteresis and eddy currents, mechanical friction loss P_{Me}, and stray loss P_{St} caused by leakage of the magnetic flux. Copper and iron losses were calculated using Eq. (20) and (21). The mechanical friction and stray losses were found to be proportional to the mechanical power of 5 %, respectively, in a previous study [79].

$$P_{elec} = P_{mech} + (P_{Co} + P_{Ir} + P_{Me} + P_{St}) = V_{m_{i_{avg}}} I_{m_{i_{avg}}} \tag{19}$$

$$P_{Co} = I_m^2 R_m \tag{20}$$

$$P_{Ir} = V_{emf}I_0 = (V_m - I_mR_m)I_0 \qquad (21)$$

The drive current, voltage of each motor and required battery energy during the current simulation time step were calculated using Eq. (16) - (21). By integrating the required battery energy in each time step of the simulation, the total required battery energy was estimated. Consequently, the flight feasibility for a given flight conditions and wind conditions was evaluated by comparing the required battery energy with the mounted battery energy. When the motor duty ratio D_t exceeded 100%, the flight simulation was terminated and we concluded that the flight failed because the mounted motor could not rotate fast as the required RPM with required mechanical power of the rotors. The duty ratio of a motor is a non-physical value when it exceeds 100%. This non-physical value occurs when the required RPM is extremely high to compensate for the position and attitude errors due to external winds, when the voltage of the mounted battery is extremely low to drive the motors. Therefore, a duty ratio exceeding 100% generated during flight under certain external wind conditions was used as a criterion for determining that the quadrotor was not able to operate under the winds.

The EPS analysis used the discharge characteristic of a commercially available battery model. To predict the battery discharge characteristic for a wingless-type eVTOL, a nearly linear discharge model [80] was implemented in the EPS analysis in this study. The parameters for a specific battery cell include the open circuit voltage V_o, the primary dependency of the voltage on the capacity discharged K, the

internal resistance R_b, and the change in the slope of the discharge curve due to the current G. With these parameters, the battery voltage is calculated as follows:

$$V_b = 0.5 \left[(V_o - KQ_b) + \sqrt{(V_o - KQ_b)^2 - 4 \left(R_b \sum_{i=1}^{N_{rotor}} P_{mech} + GQ_b \sum_{i=1}^{N_{rotor}} P_{mech} \right)} \right] \quad (22)$$

where Q_b is the total discharged capacity at the corresponding flight time and P_{mech} is the loaded mechanical power on the ith motor, as calculated by the aerodynamic analysis module.

2.1.3 6-DOF dynamics analysis module

After calculating the thrust T_i and torque Q_i generated by the ith rotor, the force and moment acting on the center of gravity are calculated by the 6-DOF dynamics analysis module, which gives the position and attitude angle after the corresponding flight time step. The rotation matrix R that converts from the body frame to the inertial frame is Eq. (23) with Euler angles ϕ, θ, and ψ.

$$\mathbf{R} = \begin{bmatrix} \cos\psi \cos\theta & \cos\psi \sin\theta \sin\phi - \sin\psi \cos\phi & \cos\psi \sin\theta \cos\phi + \sin\psi \sin\phi \\ \sin\psi \cos\phi & \sin\psi \sin\theta \sin\phi + \cos\psi \cos\phi & \sin\psi \sin\theta \cos\phi - \cos\psi \sin\phi \\ -\sin\theta & \cos\theta \sin\phi & \cos\theta \cos\phi \end{bmatrix} \quad (23)$$

The 6-DOF dynamics analysis can be applied to any number of rotors, but the direction of the moments depends on the horizontal position of the rotor and the rotor

33

rotation direction. In this study, the 6-DOF dynamics equations were driven in the arbitrary number of rotors, N. However, moments on the center of gravity induced by all rotors, $\vec{M}_{prop}$, was able to be defined, depending on the position of each rotor. Therefore, it should be noted that 6-DOF dynamics linked up with blade element theory of a quadrotor as a representative wingless-type small UAV was introduced in this section. In the case of a wingless-type eVTOL for UAM service, analyses of rotor aerodynamics and 6-DOF dynamics will be introduced in Section 2.2.2, add-on module for rotor-rotor interference.

In the case of a quadrotor, using Eq. (24) and (25), the moments $dM_{x,i}, dM_{y,i}$ and $dM_{z,i}$ at the center of gravity and local thrust, dT_i, with the number of blades N_b, and the resultant force in each rotor were calculated. Aerodynamic forces $\vec{F}_{prop}$ and moments $\vec{M}_{prop}$ of the rotating rotor are calculated by integrating along the radial direction, as shown in Eq. (26) and (27).

$$dT_i = N_b \, dF_{z,b,i} \qquad\qquad (24)$$

$$
\begin{bmatrix}
dM_{x,1}, dM_{y,1}, dM_{z,1} \\
dM_{x,2}, dM_{y,2}, dM_{z,2} \\
dM_{x,3}, dM_{y,3}, dM_{z,3} \\
dM_{x,4}, dM_{y,4}, dM_{z,4}
\end{bmatrix}
$$

$$
= N_b
\begin{bmatrix}
-dF_{z,b,1}(|Y_1| + y\sin\psi_{blade}), -dF_{z,b,1}(|X_1| - y\cos\psi_{blade}), -dF_{x,b,1}\sin\psi_{blade}\,(|Y_1| + y\sin\psi_{blade}) + dF_{x,b,1}\cos\psi_{blade}\,(|X_1| - y\,\cos\psi_{blade}) \\
dF_{z,b,2}(|Y_2| + y\sin\psi_{blade}), -dF_{z,b,2}(|X_2| - y\cos\psi_{blade}),\ \ dF_{x,b,2}\sin\psi_{blade}\,(|Y_2| + y\sin\psi_{blade}) -\ \ dF_{x,b,2}\cos\psi_{blade}\,(|X_2| - y\cos\psi_{blade}) \\
dF_{z,b,3}(|Y_3| - y\sin\psi_{blade}), dF_{z,b,3}(|X_3| + y\cos\psi_{blade}),\ \ dF_{x,b,3}\sin\psi_{blade}\,(|Y_3| - y\sin\psi_{blade}) -\ \ dF_{x,b,3}\cos\psi_{blade}\,(|X_3| + y\sin\psi_{blade}) \\
-dF_{z,b,4}(|Y_4| - y\sin\psi_{blade}), dF_{z,b,4}(|X_4| + y\cos\psi_{blade}), -dF_{x,b,4}\sin\psi_{blade}\,(|Y_4| - y\sin\psi_{blade}) + dF_{x,b,4}\cos\psi_{blade}\,(|X_4| + y\sin\psi_{blade})
\end{bmatrix}
$$

(25)

$$
\vec{F}_{prop} =
\begin{bmatrix}
0 \\
0 \\
\displaystyle\sum_{i=1}^{4} \frac{N_b}{2\pi} \int \int dT_i \ d\psi_{blade}
\end{bmatrix}
\tag{26}
$$

$$
\vec{M}_{prop} =
\begin{bmatrix}
\displaystyle\sum_{i=1}^{4} \frac{N_b}{2\pi} \int \int dM_{x,i} \ d\psi_{blade} \\
\displaystyle\sum_{i=1}^{4} \frac{N_b}{2\pi} \int \int dM_{y,i} \ d\psi_{blade} \\
\displaystyle\sum_{i=1}^{4} \frac{N_b}{2\pi} \int \int dM_{z,i} \ d\psi_{blade}
\end{bmatrix}
\tag{27}
$$

The translational accelerations $\dot{U}$, $\dot{V}$, and $\dot{W}$ and the rotational accelerations $\dot{P}$, $\dot{Q}$, and $\dot{R}$ are calculated in the body frame as follows:

$$
\begin{bmatrix} \dot{U} \\ \dot{V} \\ \dot{W} \end{bmatrix} = \boldsymbol{R}^{-1} \begin{bmatrix} 0 \\ 0 \\ -g \end{bmatrix} + \frac{\vec{F}_{prop}}{m} - \begin{bmatrix} 0 & -R & Q \\ R & 0 & -P \\ -Q & P & 0 \end{bmatrix} \begin{bmatrix} U \\ V \\ W \end{bmatrix}
\tag{28}
$$

$$
\begin{bmatrix} \dot{P} \\ \dot{Q} \\ \dot{R} \end{bmatrix} = \left(\begin{bmatrix} I_{xx} & -I_{xy} & -I_{xz} \\ -I_{yx} & I_{yy} & -I_{yz} \\ -I_{zx} & -I_{zy} & I_{zz} \end{bmatrix} \right)^{-1}
$$
$$
\left(\vec{M}_{prop} - \begin{bmatrix} 0 & -R & Q \\ R & 0 & -P \\ -Q & P & 0 \end{bmatrix} \begin{bmatrix} I_{xx} & -I_{xy} & -I_{xz} \\ -I_{yx} & I_{yy} & -I_{yz} \\ -I_{zx} & -I_{zy} & I_{zz} \end{bmatrix} \begin{bmatrix} P \\ Q \\ R \end{bmatrix} \right)
\tag{29}
$$

The translational velocities $\dot{X}$, $\dot{Y}$, and $\dot{Z}$ and the rotational velocities $\dot{\phi}$, $\dot{\theta}$, and $\dot{\psi}$ in the inertial frame are calculated as follows:

$$
\begin{bmatrix} \dot{X} \\ \dot{Y} \\ \dot{Z} \end{bmatrix} = \boldsymbol{R} \begin{bmatrix} \dot{U} \\ \dot{V} \\ \dot{W} \end{bmatrix}
\tag{30}
$$

$$
\begin{bmatrix} \dot{\phi} \\ \dot{\theta} \\ \dot{\psi} \end{bmatrix} = \begin{bmatrix} 1 & \tan\theta\sin\phi & \tan\theta\cos\phi \\ 0 & \cos\phi & -\sin\phi \\ 0 & \sin\phi/\cos\theta & \cos\phi/\cos\theta \end{bmatrix} \begin{bmatrix} \dot{P} \\ \dot{Q} \\ \dot{R} \end{bmatrix}
\tag{31}
$$

Next, the position and attitude angle after the corresponding flight time step are calculated using a fourth-order Runge-Kutta time integral with a flight time step of 10^{-3} seconds.

2.2   Add-on modules for actual operation

Based on the control, aerodynamic, and electric propulsion system analyses, the overall performance such as the position and attitude errors, thrust and mechanical power of the rotors, efficiency and duty ratio of the motors, and consumed battery energy could be predicted as results of the simulation framework. However, these analysis modules are still limited to the flight performance analysis only in ideal operation such as the flight under calm wind and the flight without rotor-rotor interference. In the case of small wingless-type UAVs in actual operation, they are easily affected by the external environment due to their relatively small size and low ground speed compared to engine-powered manned aircrafts. In the case of large wingless-type eVTOLs for UAM service in actual operation, they are easily affected by rotor-rotor interference because their multiple rotors are disposed within a limited rim size. To apply these considerations of actual operation, two add-on modules were developed: 1) wind turbulence module and 2) Rotor-rotor interference module

2.2.1 Wind turbulence module

Dahl et al. [81] analyzed the gust response of a conventional helicopter to external winds and divided the external wind models into two categories: 1) discrete and single event gust and 2) continuous stochastic disturbances. The discrete and single event gust models, which define the wind using step, ramp, or sinusoidal functions, were mainly used to evaluate the instantaneous changes caused by external winds and the resonance of the system. The continuous stochastic disturbance models,

which define the winds using random signals, were used to assess the overall performance in the external wind environment. Therefore, the continuous stochastic disturbance model was considered appropriate to evaluate the overall performance of a quadrotor under the winds. The von Kármán wind turbulence model in the Matlab/Simulink blockset was one of the representative models of the continuous stochastic disturbance models and it was chosen as the external wind model in this study. It should be noted that other wind models or wind data to provide a specific wind velocity vector are available for the wind turbulence model.

The von Kármán wind turbulence model applies the turbulence filters with variable s in frequency domain given in Eq. (32) – (34) to the white noise signals generated by a random signal and calculates the increment in the external wind speed to derive the wind velocity over time.

$$H_{V_{wind_x}}(s) = \frac{\sigma_u \sqrt{\frac{2L_u}{\pi V_{von}}} \left(1 + 0.25 \frac{L_u}{V_{von}} s\right)}{1 + 1.357 \frac{L_u}{V_{von}} s + 0.1987 \left(\frac{L_u}{V_{von}} s\right)^2} \tag{32}$$

$$H_{V_{wind_y}}(s) = \frac{\sigma_v \sqrt{\frac{L_v}{\pi V_{von}}} \left\{1 + 2.7478 \frac{L_v}{V_{von}} s + 0.3398 \left(\frac{L_v}{V_{von}} s\right)^2\right\}}{1 + 2.9958 \frac{L_v}{V_{von}} s + 1.9754 \left(\frac{L_v}{V_{von}} s\right)^2 + 0.1539 \left(\frac{L_v}{V_{von}} s\right)^3} \tag{33}$$

$$H_{V_{wind_z}}(s) = \frac{\sigma_w \sqrt{\frac{L_w}{\pi V_{von}}} \left\{1 + 2.7478 \frac{L_w}{V_{von}} s + 0.3398 \left(\frac{L_w}{V_{von}} s\right)^2\right\}}{1 + 2.9958 \frac{L_w}{V_{von}} s + 1.9754 \left(\frac{L_w}{V_{von}} s\right)^2 + 0.1539 \left(\frac{L_w}{V_{von}} s\right)^3} \tag{34}$$

Among the input parameters of the von Kármán wind turbulence model, speed V_{von} was defined as the relative motion between the external wind and the vehicle

under a low ground speed or during hovering flight [43]. In this study, wind turbulence was considered independent of the ground speed, assuming that V_{von} represented only the wind speed. The von Kármán wind turbulence was used as a tool for calculating the random signal generation and increments in the wind speed. As input parameters for the von Kármán wind turbulence model, the turbulence scale length L and turbulence intensity σ generated at a flight altitude h and the wind speed V_{von} were calculated using Eq. (35) - (38).

$$L_w = h \tag{35}$$

$$L_u = L_v = \frac{h}{(0.177 + 0.000823h)^{1.2}} \tag{36}$$

$$\sigma_w = 0.1 \ V_{von} \tag{37}$$

$$\frac{\sigma_u}{\sigma_w} = \frac{\sigma_v}{\sigma_w} = \frac{1}{(0.177 + 0.000823h)^{0.4}} \tag{38}$$

2.2.2 Rotor-rotor interference module

In flight simulation, the rotational speed of each motor changes at each simulation time step. Thus, the thrust and power required for each rotor change at each time step, so it is also necessary to perform a rotor aerodynamic analysis. The aerodynamic analysis module in the flight simulation framework predicted the rotor thrust and power efficiently using blade element theory and linear inflow model. However, it cannot consider rotor–rotor interference. This interference can be evaluated through

a CFD analysis based on a Navier–Stokes solver. For a specific wingless-type eVTOL model, the thrust and mechanical power of each rotor for various rotor speeds and airspeed conditions can be analyzed and used to build a surrogate model. This surrogate model is used in the aerodynamic analysis module to allow for rotor–rotor interference in the flight simulation framework. Various Navier–Stokes CFD solvers could be used to build the surrogate model. The solver needs to be able to calculate efficiently dozens of analysis conditions consisting of a combination of airspeed, rotor speed, and rotor rotation direction. Kim et al. [82] developed the Actuator Disk Model (ADM) code. Blade element theory was combined with PIMPLE which is PISO-SIMPLE, Pressure Implicit with Splitting the Operators (PISO) and Semi-Implicit Method for Pressure-Linked Equation (SIMPLE) in OpenFOAM, an open-source CFD code. The incompressible solver in OpenFOAM was developed by Jasak [83]. The reliability of the ADM solver for a single rotor was validated by comparing forward flight data for rotor–body interactions with the numerical results from ADM in Kim et al. [84] and Son et al. [85]. In this study, it was determined that the ADM solver can efficiently predict rotor–rotor interference for various flight conditions.

The pressure difference between the top and bottom of the virtual disk is added as the source term of the momentum equation at designated computed cells in the virtual disk [82]. At the other computed cells, the source term becomes zero. The momentum equation added the source term, $\vec{s}$, is calculated as follow:

$$\frac{\partial U}{\partial t} + \nabla \cdot \left(\vec{U}\vec{U} \right) - \nabla \cdot \left(\nu \nabla \vec{U} \right) = \vec{s} - \nabla p \qquad (39)$$

$$\vec{s} = \frac{d\vec{T}}{\rho dV} \qquad (40)$$

where ρ is density, dV is the volume of the cell, and $d\vec{T}$ is the local thrust. Fig. 2-6 shows the overall flowchart of rotor analysis using the ADM code.
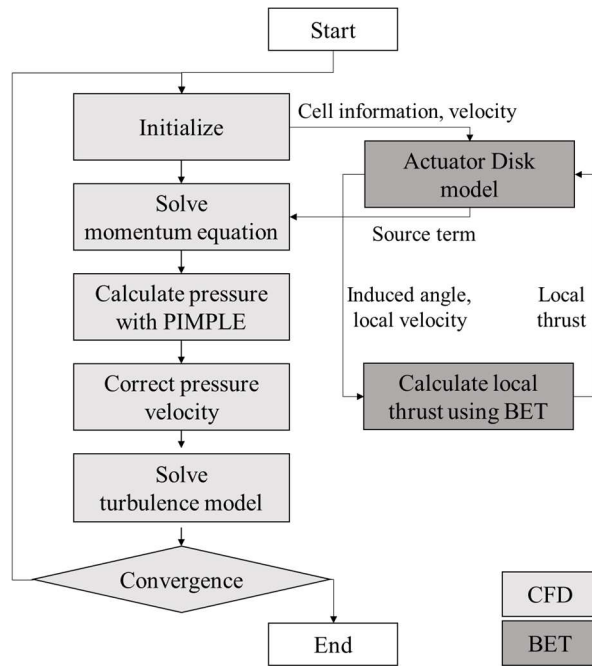
Fig. 2-6 Rotor analysis algorithm [82]

A surrogate model was generated to predict thrust and power coefficient of each rotor, using the ADM solver. The surrogate model applicable to the flight simulation framework was constructed in the form of a fourth-order polynomial of the response

41

surface model (RSM). The dimensionless thrust and power coefficients based on the minimum and maximum values for the ith rotor, $\bar{C}_{T,P,i}$, are calculated as follows:

$$\begin{bmatrix} \bar{C}_{T,P,1} \\ \vdots \\ \bar{C}_{T,P,18} \end{bmatrix} = [D][C_{RSM}]^T + E \tag{41}$$

$$[D] = \begin{bmatrix} \overline{RPM}, \bar{U}, \bar{V}, \bar{W}, \overline{RPM^2}, \bar{U}^2, \bar{V}^2, \bar{W}^2, \overline{RPM^3}, \bar{U}^3, \bar{V}^3, \bar{W}^3, \\ \overline{RPM^4}, \bar{U}^4, \bar{V}^4, \bar{W}^4, \overline{RPM\,U}, \overline{RPM\,V}, \overline{RPM\,W}, \overline{UV}, \overline{UW}, \overline{VW} \end{bmatrix} \tag{42}$$

C_{RSM} is the coefficient matrix, E is a constant matrix, and D is a variable matrix.

The detail values of the surrogate model are presented in Chapter 5, Section 3.

Using the surrogate model, thrust T_i and torque Q_i of ith rotor were calculated. Total force $\vec{F}_{prop}$ and moment $\vec{M}_{prop}$ at the center of gravity induced by rotors were calculated by Eq.(43) and (44).

$$\vec{F}_{prop} = \sum_{i=1}^{18} T_i \tag{43}$$

$$\vec{M}_{prop} = \begin{bmatrix} \sum_{i=1}^{18} M_{X,i} \\ \sum_{i=1}^{18} M_{Y,i} \\ \sum_{i=1}^{18} M_{Z,i} \end{bmatrix} \tag{44}$$

The moment of ith rotor in each axis, $M_{X,i}$, $M_{Y,i}$, $M_{Z,i}$, are shown in Table 2-2. The moment of ith rotor in each axis. After that, rest of 6-DOF dynamics procedure is identical with Section 2.1.4.

Table 2-2. The moment of ith rotor in each axis

Rotor number	$M_{X,i}$	$M_{Y,i}$	$M_{Z,i}$ Hexa-like	$M_{Z,i}$ FRRA
1	$T_1 Y_1$	$-T_1 X_2$	Q_1	Q_1
2	$T_2 Y_1$	$-T_2 X_4$	Q_2	$-Q_2$
3	$T_3 Y_3$	$-T_3 X_3$	Q_3	Q_3
4	$T_4 Y_2$	0	$-Q_4$	Q_4
5	$T_5 Y_4$	$-T_5 X_1$	$-Q_5$	Q_5
6	$T_6 Y_4$	$T_6 X_1$	$-Q_6$	$-Q_6$
7	$T_7 Y_1$	$T_7 X_2$	Q_7	Q_7
8	$T_8 Y_3$	$T_8 X_3$	Q_8	$-Q_8$
9	$T_9 Y_1$	$T_9 X_4$	Q_9	$-Q_9$
10	$-T_{10} Y_1$	$T_{10} X_2$	$-Q_{10}$	$-Q_{10}$
11	$-T_{11} Y_1$	$T_{11} X_4$	$-Q_{11}$	Q_{11}
12	$-T_{12} Y_3$	$T_{12} X_3$	$-Q_{12}$	Q_{12}
13	$-T_{13} Y_2$	0	Q_{13}	$-Q_{13}$
14	$-T_{14} Y_4$	$T_{14} X_1$	Q_{14}	Q_{14}
15	$-T_{15} Y_4$	$-T_{15} X_1$	Q_{15}	$-Q_{15}$
16	$-T_{16} Y_1$	$-T_{16} X_2$	$-Q_{16}$	$-Q_{16}$
17	$-T_{17} Y_3$	$-T_{17} X_3$	$-Q_{17}$	$-Q_{17}$
18	$-T_{18} Y_1$	$-T_{18} X_4$	$-Q_{18}$	Q_{18}

Chapter 3.

Validation of Simulation Framework

3.1 Static thrust and torque on a single rotor test

Thrust and mechanical power of a commercially available rotor, Graupner E-9x5, were measured in Theys [86] with various rotor tilt angles and steady wind conditions. The rotor in the experiment was fixed which was zero ground speed. And the wind conditions in the experiment were calm wind and 6 m/s wind speed. To validate the aerodynamic analysis module, blade geometry data of the rotor such as chord length and twist were used. Thrusts and torques for two test conditions of calm wind without disk tilt and 6 m/s wind speed with 30° disk tilt were compared with the aerodynamic analysis results. As analysis parameters, induced power factor value of 1.1 and tip loss factor value of 0.98 were used. Thrust and torque were properly predicted with the parameter values, as shown in Fig. 3-1. The maximum torque error of 7 % was shown at rotation speed of 9,137 RPM. It was found that the accuracy of aerodynamic analysis was acceptable to predict the performance in various flight and wind conditions.
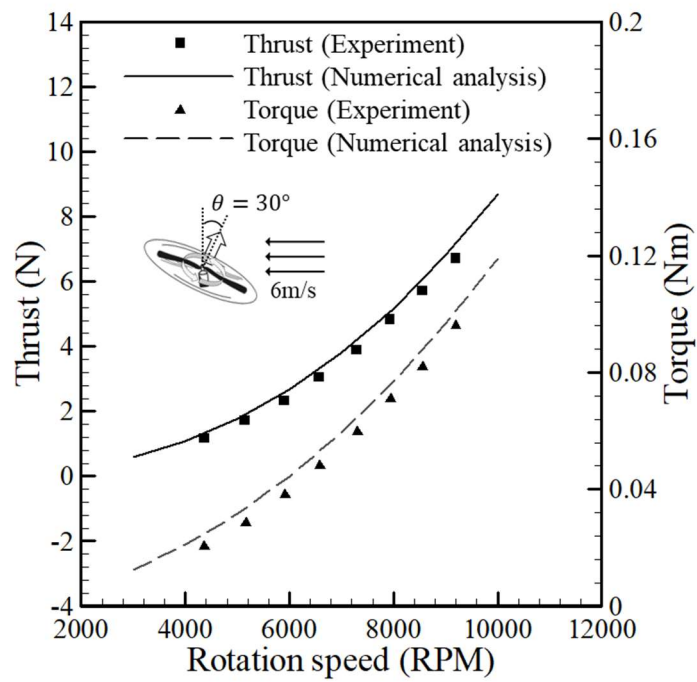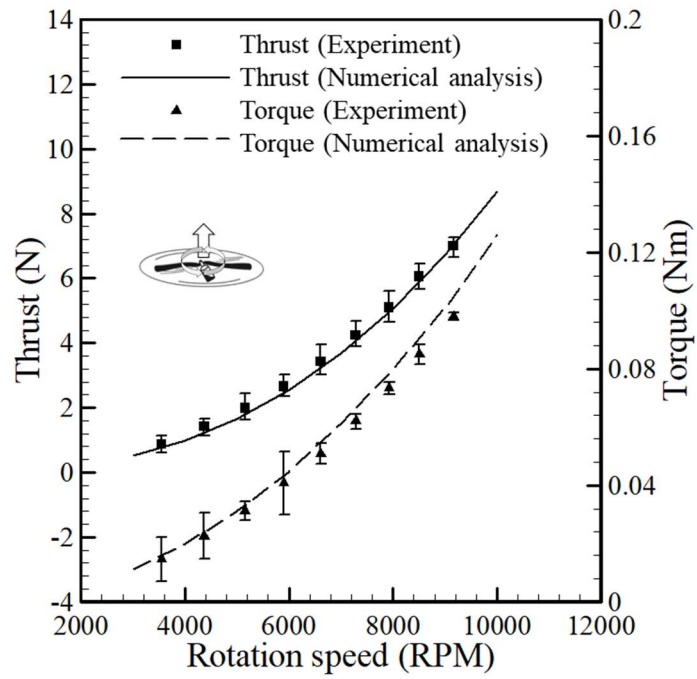
Fig. 3-1 Static thrust and torque of a Graupner E-9x5 under calm wind

45

3.2   Wind resistance test

DevKopter2 was developed by KARI as shown in Fig. 3-2. Table 3-1 provides the specifications of the hypothetical model. The quadrotor model was composed of T-motor 22x6.6 rotors and T-motor U7-V2.0 KV280 motors. The internal resistance and no-load current values of the motor were obtained from official website of T-motor[†]. The values of the voltage per battery cell and ESC internal resistance were estimated based on the battery discharge data and ESC internal resistance estimation performed by Lim [41].

Fig. 3-2 DevKopter2 developed by KARI

---

† https://www.dji.com/kr/matrice100/info#specs (2020). (Accessed 17 March 2020)

Table 3-1. Specifications of DevKopter2 model

Component group	Component	Value	Unit
Rotor	Diameter	22	inch
	Pitch	6.6	inch
	Number of blades	2	
Motor	Speed constant	280	Kv
	Inner resistance	0.071	Ω
	No-load current	0.5	A
Battery	Capacity	10	Ah
	Number of cells	6	
ESC	Maximum current	60	A
	Inner resistance	0.0017(estimated)	Ω
Frame	Wheelbase	0.95	m

To verify the validity of the performance analysis simulation, the numerical results were compared with the wind resistance experiment of DevKopter2 tested by KARI. The pitch angle and battery voltage drop of DevKopter2 were measured with respect to the crosswind velocities in hovering flight. The measured velocity of the crosswind was gradually increased from 1 m/s to 13 m/s with plateaus as shown in Fig. 3-3. As the experimental data fluctuated locally owing to noise from the sensor and non-uniform wind profiles, the measured pitch angle data were filtered using a Savizky–Golay filter, which is the least squares smoothing filter in Matlab. Using the measured data of the wind velocity profile as the ambient wind condition for the simulation, calculated pitch angles were compared with the filtered pitch angle data from the experiment. When the wind speed was 5 m/s, the pitch angle analysis error up to 2° occurred during flight endurance between 40 seconds and 70 seconds, but

the error was reduced in subsequent flight periods. In addition, the absolute value of the filtered pitch angle was 12.3° when the wind speed was at the maximum value of 13 m/s, and the difference between the calculated and measured pitch angles was 1.4° at this wind speed. The pitch angle was slightly overestimated during calculation compared to the measured pitch angle. However, the pitch angle error of the quadrotor calculated during the simulation was acceptable for the flight simulation.
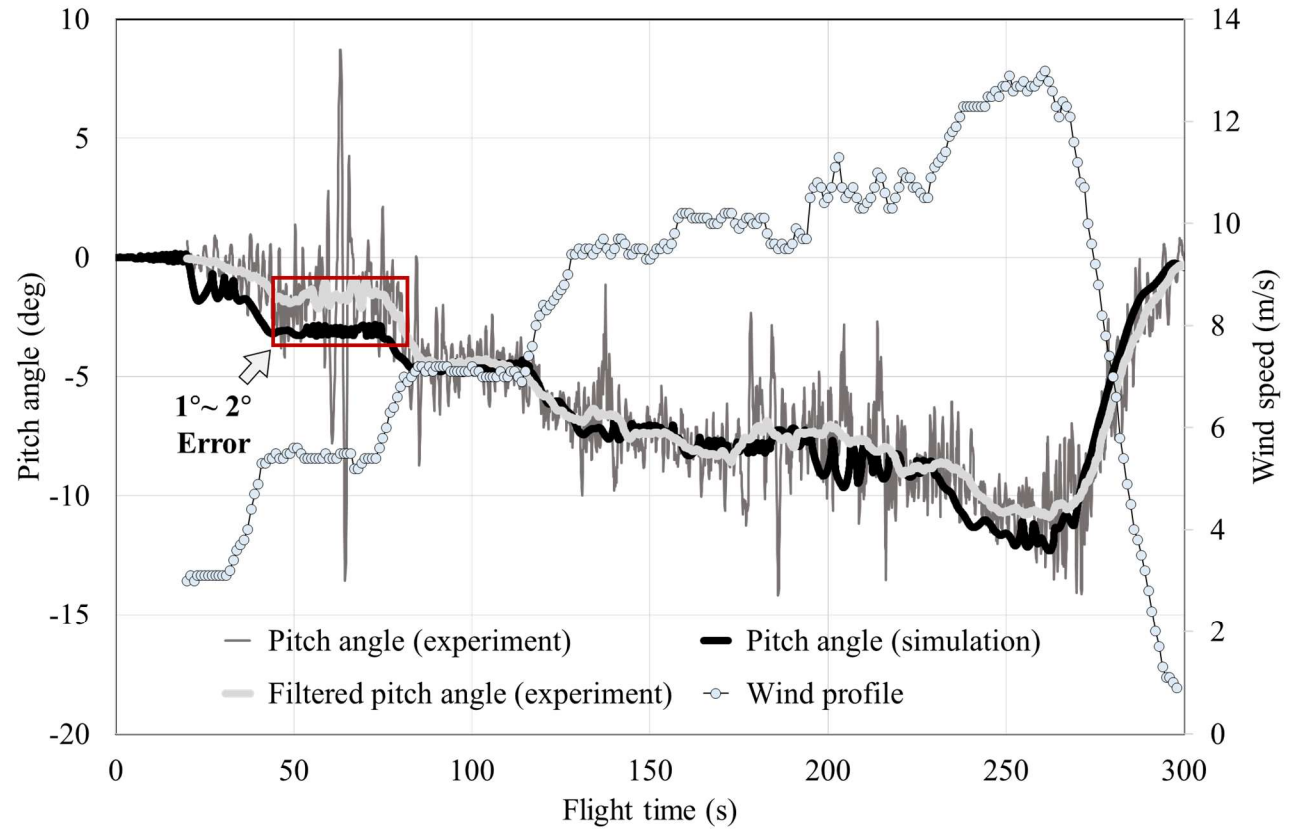
Fig. 3-3 Comparison of pitch angle with respect to wind speeds

In the same experiment, the battery voltage was measured and compared with the simulation result, as shown in Fig. 3-4. To exclude the battery energy consumed for the idling test and climbing before the experiment, the initial voltage value of the electric propulsion system analysis was set to 23.65 V, which was the value when the crosswind started blowing in the experiment. As the wind fluctuated locally, the measured battery voltage data were filtered using Savizky–Golay filters. Although the filtered voltage data at interval from 80 seconds to 120 seconds with 7 m/s wind velocity seems to be a constant value and then decreased afterward, the battery voltage analysis results showed a steady decrease. In the simulation time from 80 seconds to 120 seconds, the difference between the calculated and measured battery voltage was from 0.2 V to 0.23 V. This difference was considered acceptable because the voltage difference was considerably small, i.e. approximately 1 % of 22.2 V, which was the representative value of the six-cell battery.
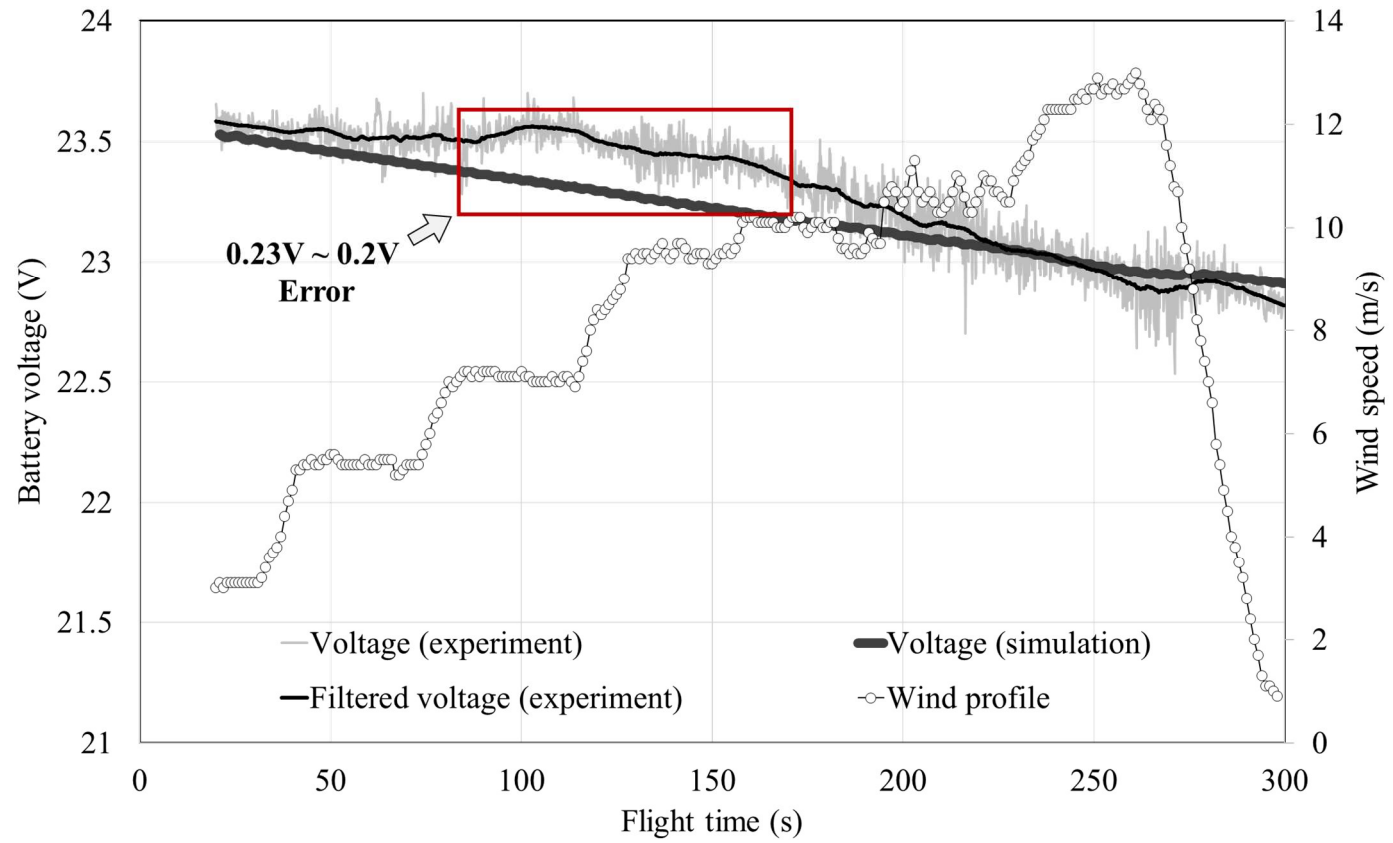
Fig. 3-4 Comparison of battery voltage with respect to wind speeds

3.3   Rotor-rotor interference of tandem rotors

The reliability of the ADM analysis for a single rotor was validated in previous studies [82], [84], and [85], but further validation was needed to assess whether the effect of rotor–rotor interference for multiple rotors was reliable in a numerically appropriate way. The ADM results of thrust and power were compared with those from a previous study of rotor–rotor interference for tandem rotors [70]. In the previous study, Free-Vortex Wake (FVW) model was validated with the experimental data of XV-15 rotors in [87]. After that, thrust and mechanical power of tandem rotors was investigated using the FVW model. The study on the effect of rotor–rotor interference during the forward flight of tandem rotors without fuselage was selected as a benchmark case for validating ADM in this study. The ADM analysis was conducted with a hypothetical rotor based on XV-15 two-bladed rotors, proposed in the benchmark study. The freestream velocity was an advance ratio μ_∞ of 10 m/s, and the disk angle of rotor α_{disk} was 5° nose-down. These settings were the same as the benchmark study. Comparison results of thrust and mechanical power of the tandem rotors are shown in Fig. 3-5 for thrust and Fig. 3-6 for mechanical power. Thrust ratio and power ratio means the ratio of the thrust and power in tandem rotors to the thrust and power in an isolated rotor, respectively. When the tip-to-tip separation distances was decreased, thrust loss and mechanical power of the rear rotor was increased. Thrust was decreased by up to 0.96 and mechanical power was increased by up to 1.05 in the separation distance of 0.1. These trends of thrust and mechanical power were similar in both FVM and ADM results, with maximum error

52

of 1% in the thrust analysis and the error of 2% in the mechanical power analysis. Therefore, since the thrust and mechanical power results from the ADM analysis of the tandem rotors were similar to the results from the numerical analysis of the benchmark case, it was judged that ADM was reliable for analyzing rotor–rotor interference.
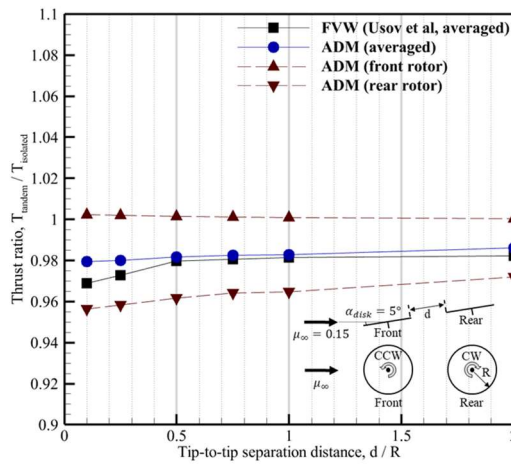
Fig. 3-5 Thrust ratio of tandem rotors with respect to tip-to-tip separation distances
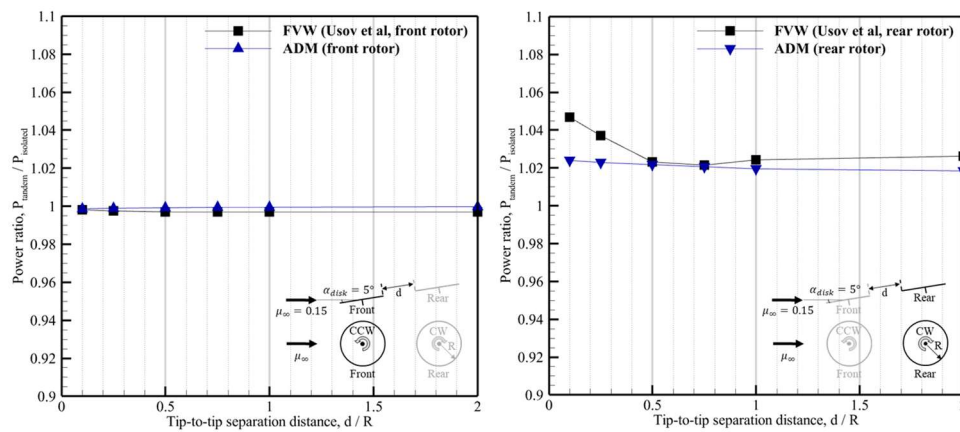
Fig. 3-6 Mechanical power ratio of tandem rotors with respect to tip-to-tip separation distances

53

3.4 Rotor-rotor interaction of a quadrotor in CFD

The ADM results were compared with those from a previous study of rotor–rotor interference for a quadrotor UAV [68]. The study on the effect of rotor–rotor interference during the forward flight of a small quadrotor UAV was selected as a benchmark case for validating ADM in this study. The ADM analysis was conducted with APC 12×5.5 rotors in the plus configuration. The turbulence model of Spalart-Allmaras in OpenFOAM was used. The forward speed was 10 m/s, and the aircraft was in a 5° nose-down pitch attitude. These settings were the same as the benchmark case. Fig. 3-7 shows the computational domain for the ADM analysis. The far-field was the same as the benchmark case. The virtual rotor disk consisted of elements that were as long as 2 % of the rotor radius. There were 13 million grid points. The ADM analysis was performed for 18 rotations with a fixed time step corresponding to a 1° rotation of the azimuth angle based on the average rotational speed of the entire rotor.
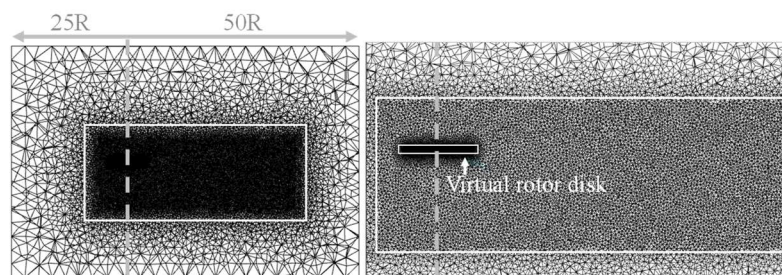
Fig. 3-7 Computational domain of the far-field (left) and the virtual rotor disk (right)

Thrust comparison of all rotors are shown in Fig. 3-8 and Fig. 3-9, with maximum error of 3.6 % in the east rotor. The analysis method used in the benchmark predicted

the effect of rotor–rotor interference from the rotor blades, whereas ADM predicted the interference effect from the rotor disk. Despite this difference, the differences in the numerical analysis results for the thrust of each rotor thrust were insignificant. The azimuth angular region of the rear rotor affected by downwash from the front rotor was similar in the ADM data and in the benchmark data.
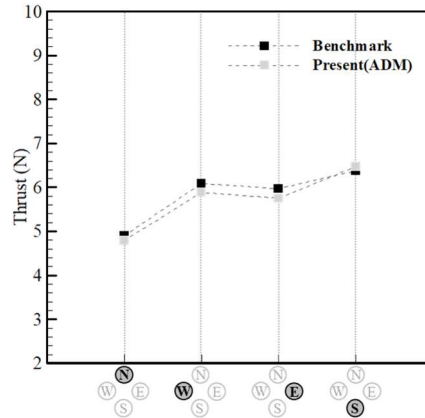
Fig. 3-8 Thrust comparison of north, west, east, and south rotors
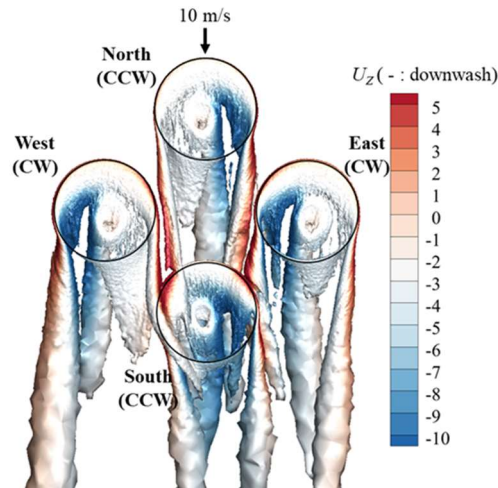
Fig. 3-9 Iso-surfaces for $Q = 500$ with color-coded vertical velocities for

forward flight at 10 m/s

55

Comparing the thrust distribution of the north and south rotors in Fig. 3-10, the thrust loss for the south rotor occurred at 150° to 210° azimuth angle due to rotor–rotor interference. This loss of thrust by the south rotor was due to the downwash from the north rotor in that angular region. These results for decreased thrust by the south were similar to the benchmark case. However, the thrust was higher in the region from 150° to 210° in the south rotor compared to the same region in the north rotor. This increase was due to the upwash from the west rotor. Therefore, since the results for rotor–rotor interference from the ADM analysis in this study are similar to the results from the numerical analysis of the benchmark case, it was judged that ADM was reliable for analyzing rotor–rotor interference.
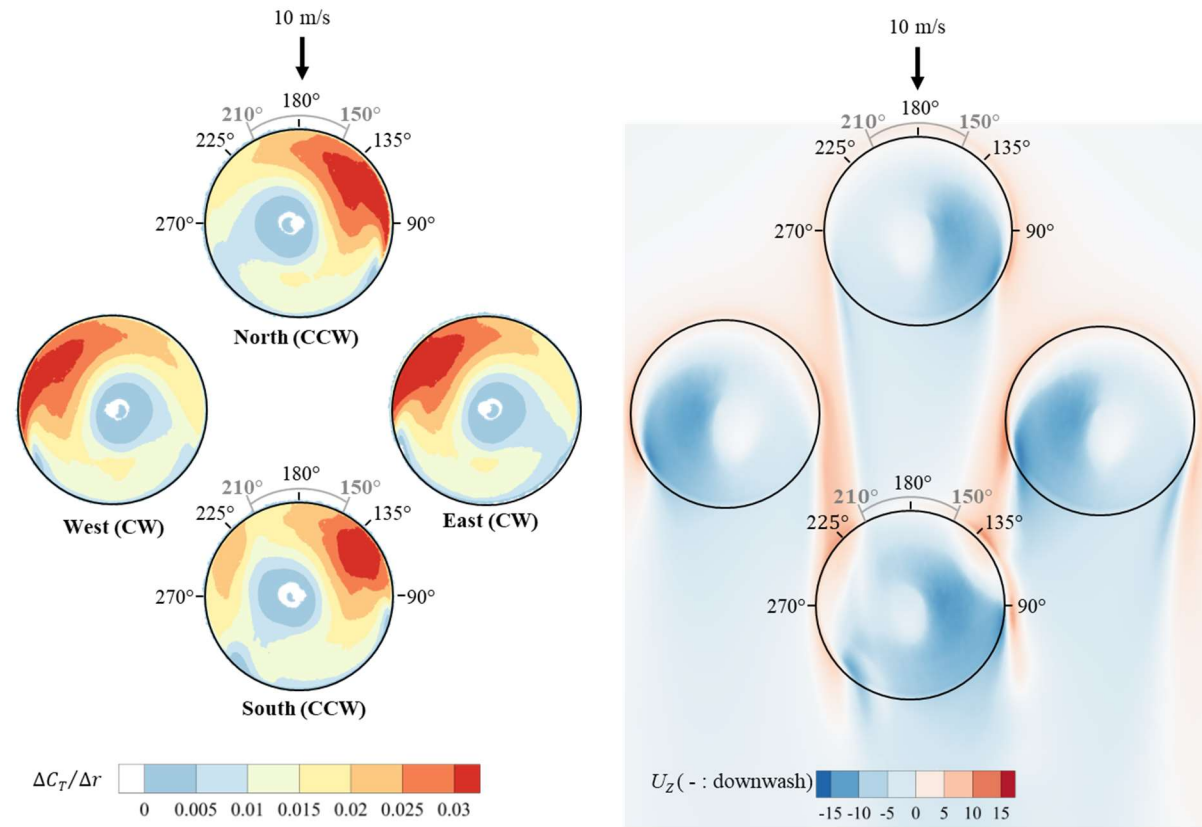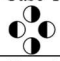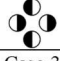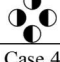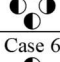
Fig. 3-10 Sectional thrust coefficient (left) and vertical velocity (right) for forward flight at 10 m/s

3.5 Investigation of rotor-rotor interference with respect to rotation directions in a quadrotor

The ADM results were compared with those from a previous study of rotor–rotor interference for a quadrotor UAV. In a wingless-type eVTOL for UAM service, there are more rotors within the limited size of the rim than for a small quadrotor UAV. Hence, the distance between rotors as a percentage of the rotor radius is smaller. For example, the gap between two adjacent rotors of the Volocopter 2X model is estimated to be about 10% of the rotor radius. To investigate the effect of rotor–rotor interference when the distance between rotors is reduced, an ADM analysis was performed when the gap between rotors was reduced from 80% of the radius in the benchmark configuration to 10% of the radius. In addition, ADM analysis was conducted in six cases of rotational directions. These cases are representative of all rotational directions that can be used in a quadrotor. As the ADM results, the thrust for each rotor is shown in Table 3-2.

Table 3-2. Thrusts with respect to gap of rotors and rotation direction

		Rotor	North	West	East	South
Gap of 80% radius	Benchmark	Rotation direction	CCW	CW	CW	CCW
		Thrust, N	4.79	5.89	5.75	6.47
		Difference with isolated rotor, %	0.2	3.4	1	0.3
Gap of 10% radius	Case 1	Rotation direction	CCW	CW	CW	CCW
		Thrust, N	4.95	6	5.77	5.92
		Difference with isolated rotor, %	3.1	5.4	1.2	-8.7
	Case 2	Rotation direction	CW	CCW	CCW	CW
		Thrust, N	4.95	5.76	6.01	5.92
		Difference with isolated rotor, %	3.2	1.2	5.4	-8.8
	Case 3	Rotation direction	CCW	CCW	CW	CW
		Thrust, N	4.97	5.75	5.76	5.87
		Difference with isolated rotor, %	3.54	1.00	1.05	-9.62
Advancing Retreating	Case 4	Rotation direction	CW	CCW	CW	CCW
		Thrust, N	4.97	5.75	5.76	5.87
		Difference with isolated rotor, %	3.6	1.0	1.2	-9.5
	Case 5	Rotation direction	CCW	CW	CCW	CW
		Thrust, N	4.93	6.01	5.9	6.02
		Difference with isolated rotor, %	2.7	5.6	3.6	-7.2
	Case 6	Rotation direction	CW	CW	CCW	CCW
		Thrust, N	4.93	5.90	6.02	6.03
		Difference with isolated rotor, %	2.7	3.7	5.7	-7.1

When the gap between the rotors was decreased from 80% of the radius to 10% with the same rotation direction, Benchmark and Case 1 in Table 3-2 showed that the difference in the thrust for the rotors due to the rotor–rotor interference was increased compared to an isolated rotor. In particular, a reduction of 8.7% occurred for the thrust of the south rotor, which was the rearmost rotor. This reduction was because the downwash from the north rotor flowed into the advancing side of the south rotor, as shown in Case 1 of Fig. 3-11,Fig. 3-12, and Fig. 3-13.

The results of thrust difference with isolated rotor were almost identical in Case 1 and Case 2. Both Case 3 and Case 4, and both Case 5 and Case 6 corresponded to the identical thrust difference. The tendency to show a similar thrust difference even though the rotation directions were different was determined by the strength of the downwash of the front rotor flowing into the advancing side of the rear rotor. For

example, in the case of the north rotor rotated counter-clockwise as shown in Fig. 3-11, the advancing side of east rotor had an impact on the stronger downwash from the north rotor than the west rotor. Also, strong downwash from the north and east rotor affected the south rotor in Case 1, the downwash from the north, east, and west rotor affected the south rotor in Case 3, and the downwash from the north rotor affected the south rotor in Case 5. As shown in Fig. 3-12 of the vertical velocity difference with the isolated rotor, much stronger downwash difference from 2 m/s to 5m/s in the south rotor of Case 3 was calculated than Case 1 and Case 5. Because the downwash increased the induced angle of attack of rotor disk, the difference of the induced angle was more increased in Case 3 than other cases, as shown in Fig. 3-12. The increased induced angle resulted in the decreased effective angle of attack and sectional thrust. Therefore, low induced angle in the advancing side of a rotor, which have high freestream velocity magnitude and mainly generates thrust, is important to minimize the loss of thrust. As shown in sectional thrust difference at Fig. 3-13, east and south rotor in Case 1, east, west and south rotor in Case 3, and only south rotor in Case 5 had a negative impact on the thrust by strong downwash and high induced angle. As a result, west rotor in Case 1 and east and west rotor in Case 5, which were affected by weak downwash from retreating side of north rotor, generated above 4 % higher thrust, as shown in Fig. 3-13. In south rotor, minimized loss of the thrust was calculated in Case 5 because weak downwash from retreating side of both west and east rotors flowed into the south rotor.

60

In summary, the rotor-rotor interference is the concurrent interaction between the aerodynamic force of one rotor and induced velocities from the other rotors. A rotating front rotor generates its aerodynamic force and induced velocity. In forward flight, the induced velocity from the front rotor affects the aerodynamic forces of the rear rotors. These induced velocities and aerodynamic forces of the rotors are needed to be concurrently and iteratively calculated in the same computational domain for the ADM analysis.

If the advancing side of the front rotor was aligned with the advancing side of the rear rotor, strong downwashes from the advancing side of the front rotor affected the advancing side of the rear rotor, resulting in the reduced thrust of the rear rotor. Therefore, it was concluded that the reduction of the rear rotor's thrust was minimized when the retreating side of the front rotor and the advancing side of the rear rotor were aligned in a straight line. This concept of rotation direction to minimize the thrust loss of rear rotors due to rotor-rotor interference, FRRA(Front Retreating Rear Advancing), is proposed in this study. However, the ADM results were for only four rotors and a fixed rotor speed without actual control feedback, which was still insufficient to predict flight performance in trimmed thrust conditions.
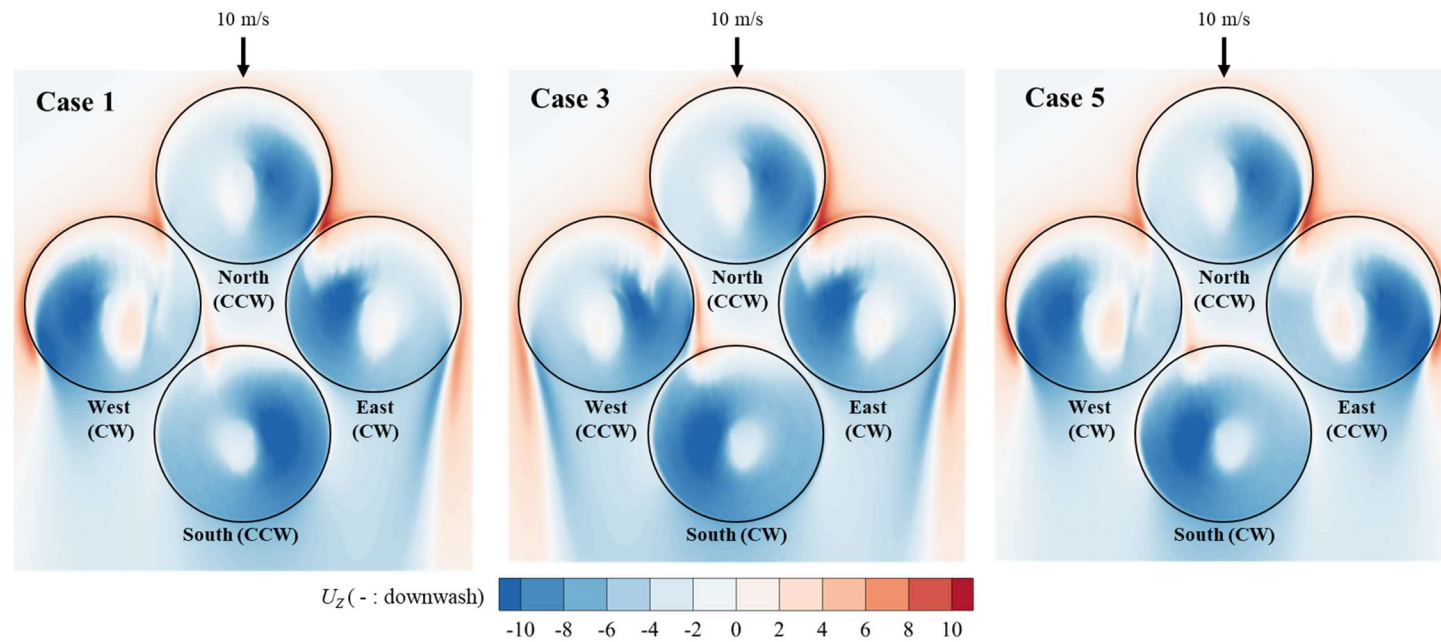
Fig. 3-11 Vertical velocity with a gap of 10% of the radius for forward flight at 10 m/s in three cases of the counter-clockwise north rotor
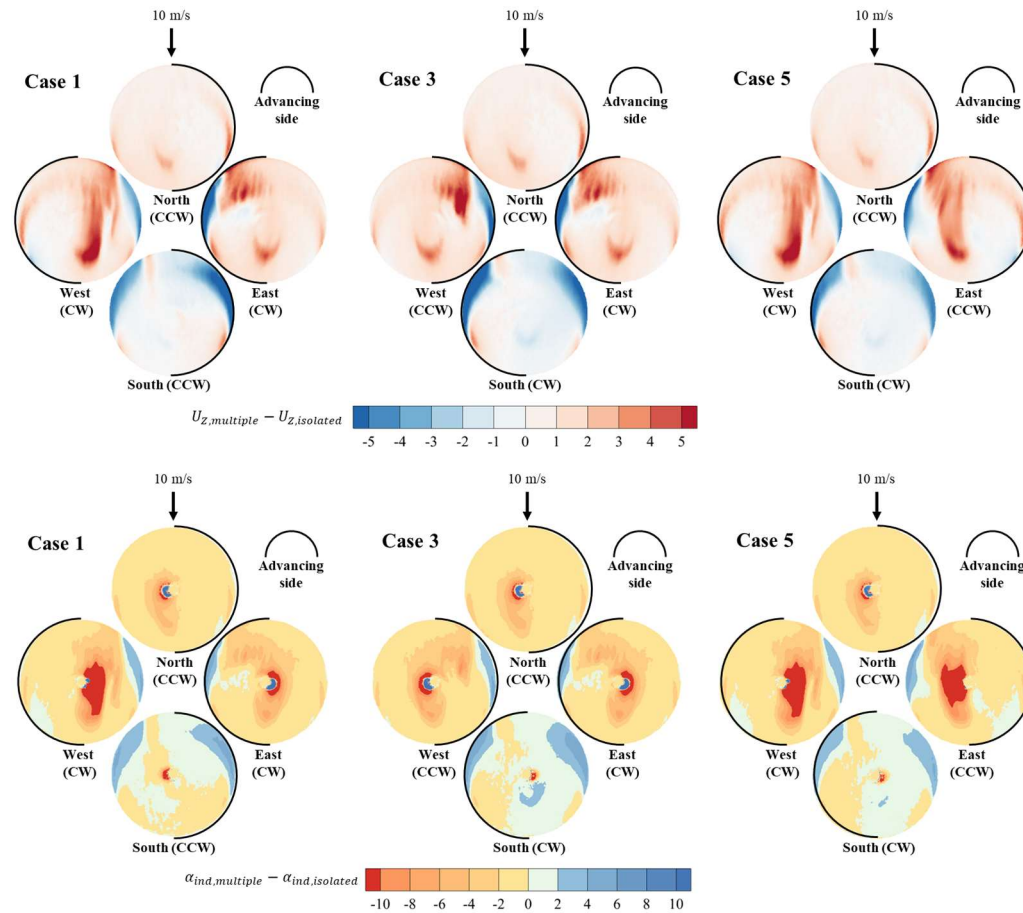
Fig. 3-12 Difference with the isolated rotor of vertical velocity and induced angle of attack with for forward flight at 10 m/s
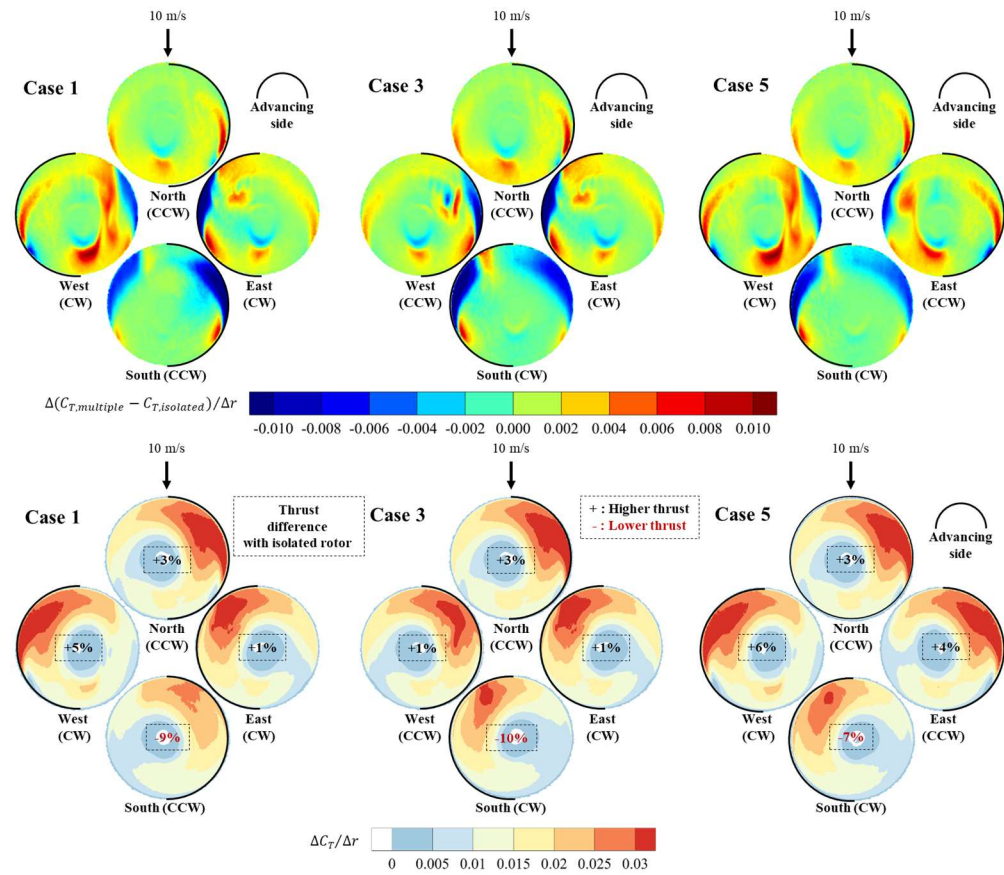
Fig. 3-13 Sectional thrust and its difference with the isolated rotor for forward flight at 10 m/s

64

Chapter 4.

Flight Performance of Quadrotor under Wind Turbulence

A hobby quadrotor can flexibly terminate the flight depending on the remained battery energy during the mission. However, industrial quadrotors have more restriction in terminating their mission than hobby quadrotors when they run out of battery energy during the operation. Thus, the required battery energy and overall flight endurance reduction induced by the winds were investigated for a hypothetical model of a quadrotor UAV similar to DevKopter2 in Chapter 3 and Section 2. The weight of the model was 5 kg classified by the weight ranges of DJI industrial quadrotors[†].

4.1 Flight conditions

The flight conditions cover a climbing flight up to an altitude of 30 m at a speed of 0.5 m/s, and forward flight that maintains the altitude until depth of discharge reaches 75 %, which was a common flight for various missions as shown in Fig. 4-1. Assuming that 80 % of total battery energy is used for climbing, forward flight, and landing, 5 % of battery energy was considered for landing. The overall flight

---

† https://www.dji.com/kr/matrice100/info#specs (2020). (Accessed 17 March 2020)

endurance of the middle and lightweight class quadrotors was analyzed for five

forward ground speeds of 0, 3, 6, 9, and 12 m/s as well as under four wind conditions,

namely calm wind, light breeze, moderate breeze, and strong breeze.

Climbing
- Altitude: 0~30m
- Time: 60s
- Rate of clime: 0.5m/s

Forward flight
- Altitude: 30m
- Ground speed: 0(hovering), 3m/s, 6m/s, 9m/s, 12m/s
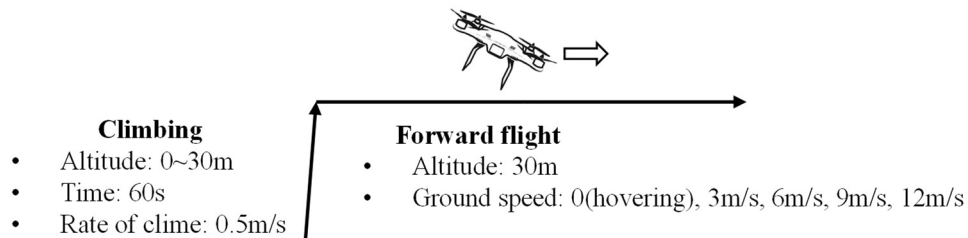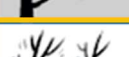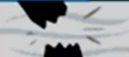
Fig. 4-1 Flight conditions

4.2   Wind turbulence conditions

The flight altitude of the quadrotor in the simulation was 30 m. The average wind

speed used to define the wind turbulence intensity was determined from four types

of winds presented in the Beaufort scale, namely calm wind (V_{von} = 0 m/s), light

breeze (V_{von} = 2.45 m/s), moderate breeze (V_{von} = 6.7 m/s), and strong breeze (V_{von}

= 11.9 m/s). As results of the turbulence model, the wind velocity profiles of light,

moderate, and strong breezes was shown in Fig. 4-3.

Beaufort Scale

Beaufort number	Wind Speed (mph)	Seaman's term		Effects on Land
0	Under 1	Calm		Calm; smoke rises vertically.
1	1-3	Light Air		Smoke drift indicates wind direction; vanes do not move.
2	4-7	Light Breeze		Wind felt on face; leaves rustle; vanes begin to move.
3	8-12	Gentle Breeze		Leaves, small twigs in constant motion; light flags extended.
4	13-18	Moderate Breeze		Dust, leaves and loose paper raised up; small branches move.
5	19-24	Fresh Breeze		Small trees begin to sway.
6	25-31	Strong Breeze		Large branches of trees in motion; whistling heard in wires.
7	32-38	Moderate Gale		Whole trees in motion; resistance felt in walking against the wind.
8	39-46	Fresh Gale		Twigs and small branches broken off trees.
9	47-54	Strong Gale		Slight structural damage occurs; slate blown from roofs.
10	55-63	Whole Gale		Seldom experienced on land; trees broken; structural damage occurs.
11	64-72	Storm		Very rarely experienced on land; usually with widespread damage.
12	73 or higher	Hurricane Force		Violence and destruction.

☐ : Wind conditions in this paper

Fig. 4-2 Beaufort wind scale[†]

---

† https://www.mackiteboarding.com/judging-wind-speed-using-the-beaufort-scale.htm (Accessed 20 October 2022)
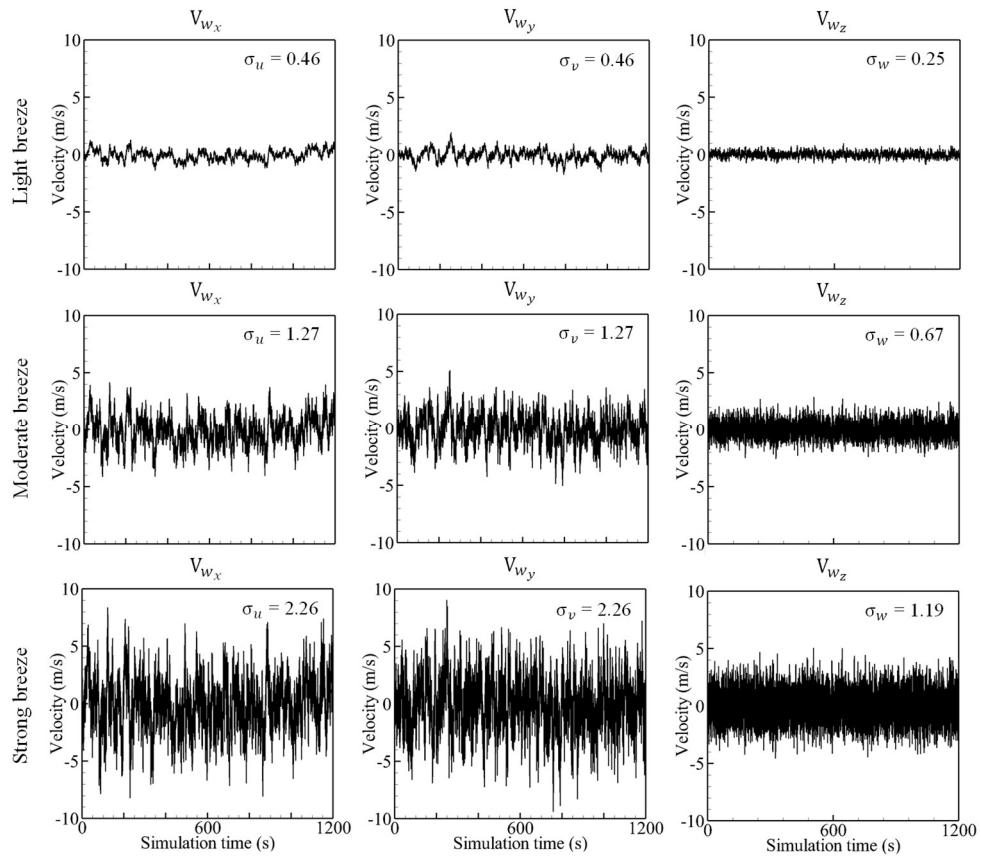
Fig. 4-3 Wind velocity profiles with respect to light, moderate, and strong

breezes

68

4.3   Simulation results

Flight performances of the middle and lightweight class quadrotors with respect to the wind conditions and ground speeds of the vehicle were investigated, such as overall flight endurance, the time averaged values of the rotation speed, thrust and mechanical power of rotors, electrical power, efficiency, and duty ratio of motors. Fig. 4-4 compares the performance variance ratio when the calm wind changes to light, moderate, and strong breezes. Each heptagon line means an amount of the ratio of the time averaged performance variance due to the wind. The zero percent line means that the performance variance due to the wind is not occur. When the middleweight class quadrotor operated at 3 m/s ground speed, the variations in the RPM, duty ratio, and motor efficiency were insignificant even if the intensity of the external wind was increased from calm wind to strong breeze. However, as the ground speed increased, a trend was shown that the required mechanical power increased and the overall flight endurance decreased, even the same strong breeze. The thrust increased by 8 %, required mechanical and electrical powers increased by 32 % during forward flight at 9 m/s, and the flight endurance decreased by 24 %.
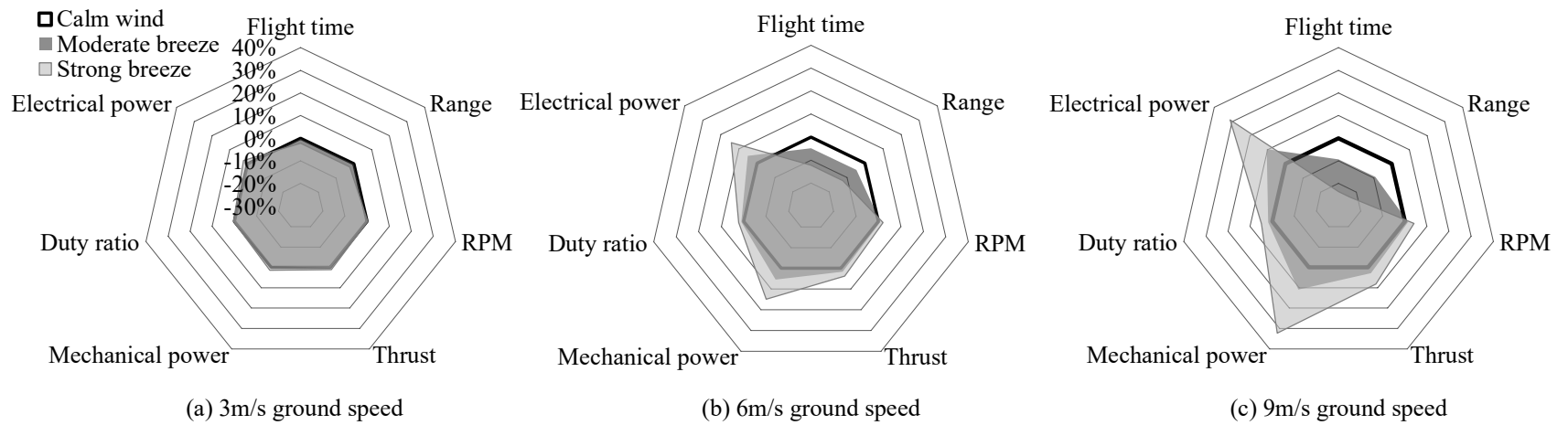
Fig. 4-4 Time averaged performances variance ratio of the hypothetical model

Legend:
□ Calm wind
■ Moderate breeze
□ Strong breeze

(a) 3m/s ground speed

(b) 6m/s ground speed

(c) 9m/s ground speed

Axis labels (each chart): Flight time, Range, RPM, Thrust, Mechanical power, Duty ratio, Electrical power

Scale (chart a): 40%, 30%, 20%, 10%, 0%, -10%, -20%, -30%

The consequences of the flight performance variance due to the winds were mainly induced by the excess thrust to cope with position error, resulting in the increased mechanical power. As shown in Fig. 4-5, Y-direction position error at 3 m/s forward flight in strong breeze was 5 m and the position error at 9 m/s forward flight in strong breeze was 14 m. Since the dynamic pressure was proportional to square of velocity magnitude, the distribution force of frame drag in Y-direction was higher when the ground speed increased, even if Y-direction wind speed was same. Consequently, the more horizontal position errors occurred at higher ground speed, the more thrust was required. The thrust was 1 % when the ground speed was 3 m/s in strong breeze, and the thrust was increased by 8 % when the ground speed was increased by 9 m/s with the same strong breeze. These increased thrusts required more fast rotational speed of rotors by the cascade PID control, and time averaged rotation speed of rotors was increased by 4 % when 9 m/s ground speed in strong breeze.
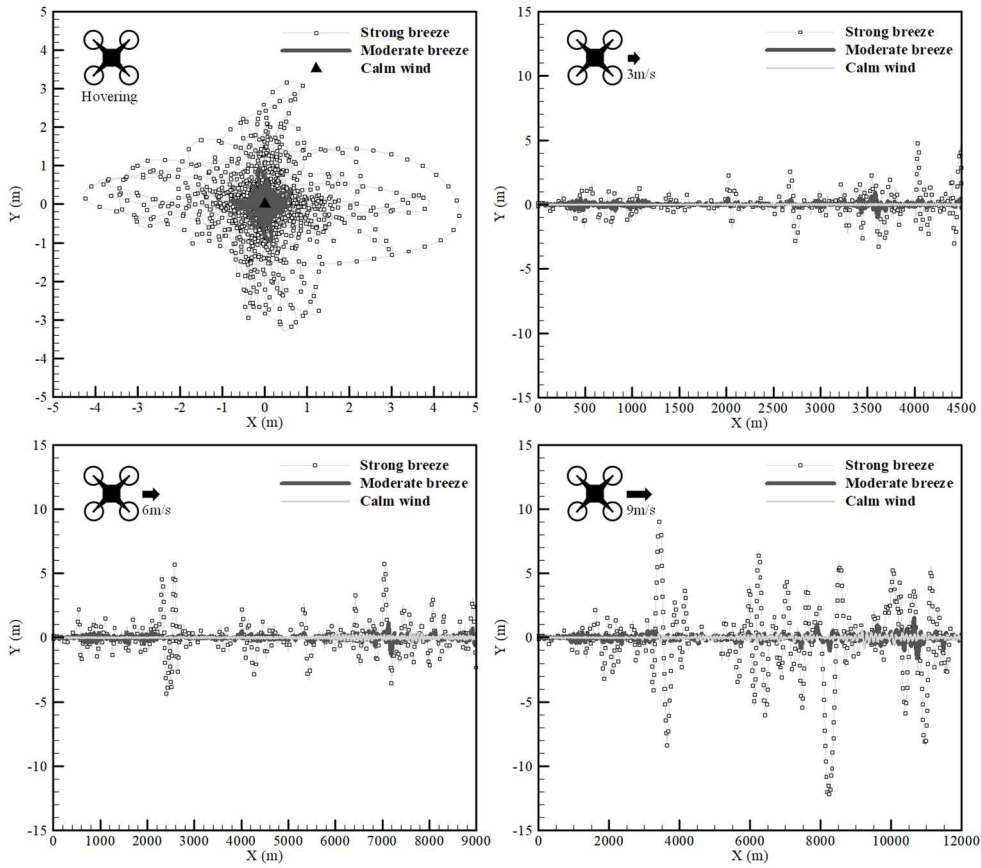
Fig. 4-5 Horizontal trajectories with respect to calm wind, moderate and strong breezes

The time averaged mechanical powers were breakdown to three powers: induced power, profile power, and parasite power, as shown in Fig. 4-6 and the results of overall flight endurance were in Fig. 4-7. When increasing the ground speed from hovering to 9 m/s, the induced power decreased by 122 W, but the profile power increased by 33 W and the parasite power increased by 48 W in calm wind. As a result, 6 m/s forward flight required minimum power of 272 W and maximum flight

endurance of 32 minutes among the ground speeds in calm wind. As the vehicle speed increased, the flight endurance reduction induced by light breeze was below 2 % until the 12 m/s ground speed. The flight endurance reduction induced by moderate breeze was below 1% until the 3 m/s ground speed, but the reduction increased to 5 %, 9 %, and 11 % at 6 m/s, 9 m/s, and 12 m/s ground speed, respectively. In addition, the flight endurance reduction induced by strong breeze increased by 12 % and 24 % at 6 m/s and 9 m/s forward flight, respectively. In conclusion, total mechanical power was more increased and overall flight endurance was more decreased when ground speed was increased, even if the same strong breeze. More flight endurance reduction induced by the winds at high ground speed was because of the increase in vertical flow in the rotor plane with respect to increase in the pitch angle. As the ground speed increased, the pitch angle for the flight increased as shown in Fig. 4-8. In strong breeze, the pitch angle was much more increased up to 16° than in calm wind to cope with the position error. This increase of the pitch angle led to increase of vertical flow of the rotor disk, which increased the induced power. Not only increasing induced power, increased pitch angle also increased frame drag and parasite power. Therefore, when the wind changes from calm wind to strong breeze at 9 m/s forward flight, induced power was increased by 11 W, profile power was increased by 25 W and parasite power was increased by 57 W. The total mechanical power increased from 289 W in calm wind to 382 W in strong breeze. And the electrical power of the electric propulsion system increased from 344 W in calm wind to 448 W in strong breeze. Subsequently, increase of the

electrical power made the battery discharge rate high and reduced the overall flight

endurance from 30 minutes in calm wind to 23 minutes in strong breeze. The 24 %

flight endurance reduction induced by the strong breeze was estimated to 18% of

total available battery energy and the excess battery energy for strong breeze was

significant magnitude to be considered before operation or in conceptual design

phase. To sum up the flight endurance results, 20 % excess battery energy could be

prevented for the overconsumptions due to the all breezes.
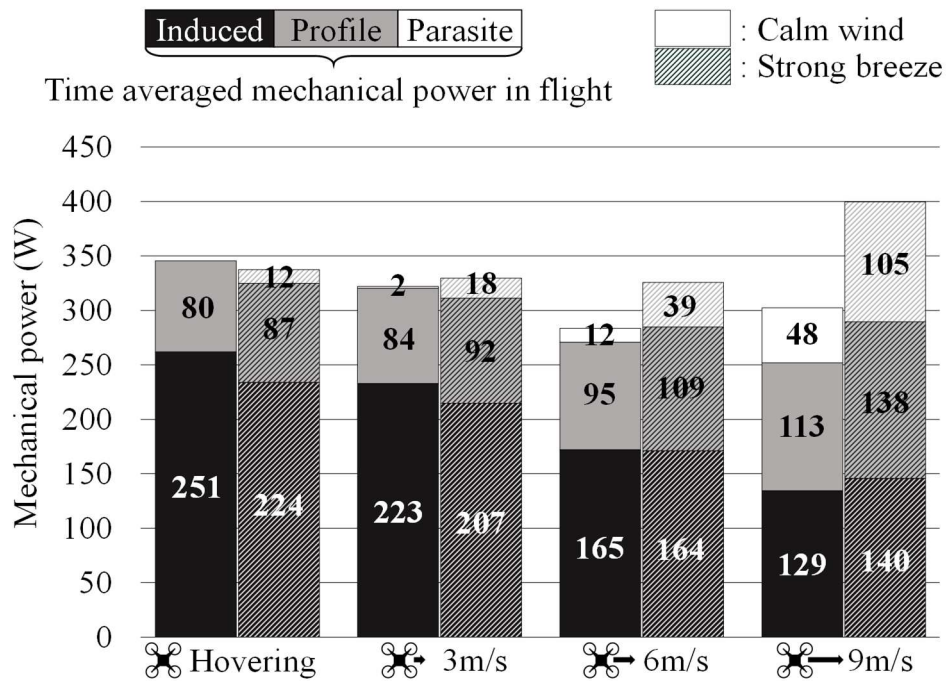
Fig. 4-6 Breakdown of the time averaged mechanical power
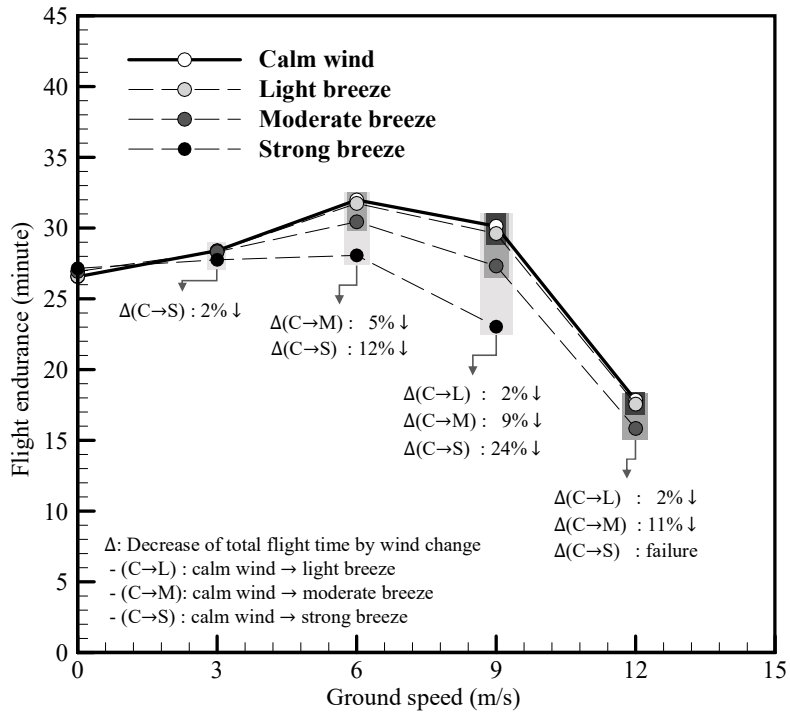
Fig. 4-7 Flight endurance variance with respect to ground speeds and winds
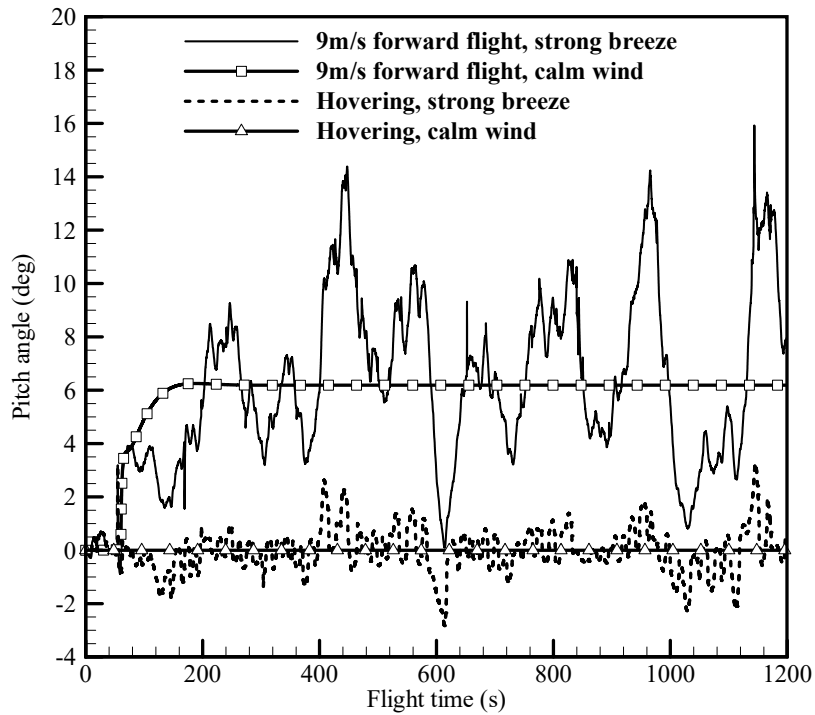
Fig. 4-8 Fluctuating pitch angle in strong breeze

For the ground speed from 3 m/s to 9 m/s in all breezes, the flight endurance of the middleweight class quadrotor decreased continuously. However, a discontinuous result was obtained at 12 m/s forward flight in strong breeze, indicating that the flight could not be completed. The flight failure was judged by the simulation algorithm since the maximum duty ratio during the flight exceeded 100 %. An increased duty ratio indicated that the power margin of the motor was reduced. The variance of the maximum duty ratio and flight endurance with respect to ground speeds and turbulence intensities are shown in Fig. 4-9. From the 6 m/s forward flight point in calm wind, the left-downward direction indicates wind changes to light, moderate, and strong breezes. The right-downward direction indicates increases in ground speeds from 6 m/s to 12 m/s. The Y-axis represents the overall flight endurance and the colored contour is the maximum value of the motor duty ratio during the flight. Under calm wind, the maximum duty ratio of the motors mounted on the middleweight class quadrotor was 60 % in 6 m/s forward flight. According to Fig. 16, the middleweight class quadrotor can operate up to a ground speed of 12 m/s in moderate breeze with a flight endurance of 16 minutes and maximum duty ratio of 88 %. Even though available battery energy remained in strong breeze, the middleweight class quadrotor was unable to complete the mission with 12m/s ground speed under strong breeze since the maximum duty ratio of motors exceeded 100 %. It was indicated that the rotation speed and aerodynamic torque of the rotors, which should be generated to withstand the wind and vehicle speed, were no longer generated by the motors at 12 m/s forward flight in strong breeze.

76
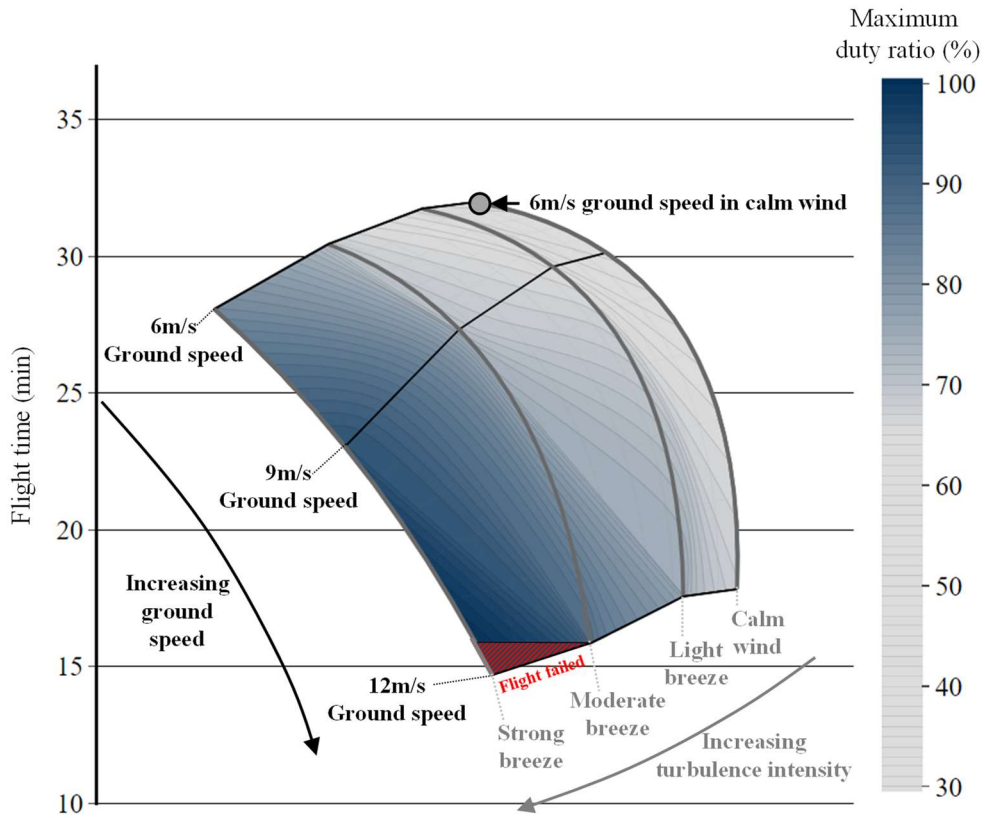
Fig. 4-9 Maximum duty ratio and flight endurance with respect to ground speeds and winds

Chapter 5.

Flight Performance of Wingless-type eVTOL for UAM Service with Respect to the Rotor Rotation Directions

A hypothetical model whose specification and configuration were similar to those of a Volocopter 2X was developed. Based on the hypothetical model, the effect of rotor–rotor interference for various rotation directions was investigated. Finally, the difference in flight performance for several ground speeds was investigated for a rotation direction with low aerodynamic performance and a direction with the desirable aerodynamic performance for operation.

5.1   Hypothetical model of a wingless-type eVTOL for UAM service

To evaluate the flight performance with respect to the rotor rotation directions for a hypothetical model of a wingless-type eVTOL which resembles a Volocopter 2X was designed. Fig. 5-1 shows geometric configuration of the hypothetical model. The model is composed of several main components such as rim, fuselage, landing gear, batteries, system requirements, and payload. Fig. 5-2 shows number of rotors and moment of inertia at the center of gravity. The bar length L_T from the center of gravity to the inner rotors (1st, 4th, 7th, 10th, 13th, and 16th), which are close to the fuselage, was 2.09 m. The bar length L_B from the inner rotor to the outer rotor was

1.88 m, the angle α between L_T and L_B was 30°, and the rotor radius was 0.9 m. The components weight and reference data are shown in Table 5-1. As the main components of the hypothetical model, the weights of the rim, fuselage, and landing gear were estimated in the CAD model for carbon fiber material with a density of 1,750 kg/m^3. Each rotor consists of two blades. The twist angle and chord length are shown in Fig. 5-3 for a T-motor 18 × 6.1 carbon rotor blade. The weight of a carbon material rotor was estimated in our previous study [88]. The motor parameters, such as internal resistance, no-load current, motor constant, and weight, were based on the specification and performance index data[†] of a commercially available brushless DC electric motor (T-motor U15 KV100). The parameters of the battery cell INR 18650-30Q were used in the validation of the linearly discharged model [80]. To supply the driving voltage of the motor, a battery of weight 80 kg was selected. This battery has 75 parallel cells, assuming 24 series cells and 250 W·h/kg specific energy at the pack level. The aircraft was fitted with fixed LED landing and taxiing lights, Garmin GRA500 radar altimeter, Genesys HeliSAS autopilot, electronic standby indicator, OuterLink CommPoint system, Jupiter audio controller system, GSR SatCom installation, airborne downlink system, and anti-collision light, as described in a brochure for an Airbus H-125 helicopter.[††]

[†] https://uav-en.tmotor.com/html/2018/u_0330/8.html

[††] https://us.airbus.com/sites/g/files/jlcbta141/files/2021-10/AHNA-Options-Catalogue%20%281%29.pdf
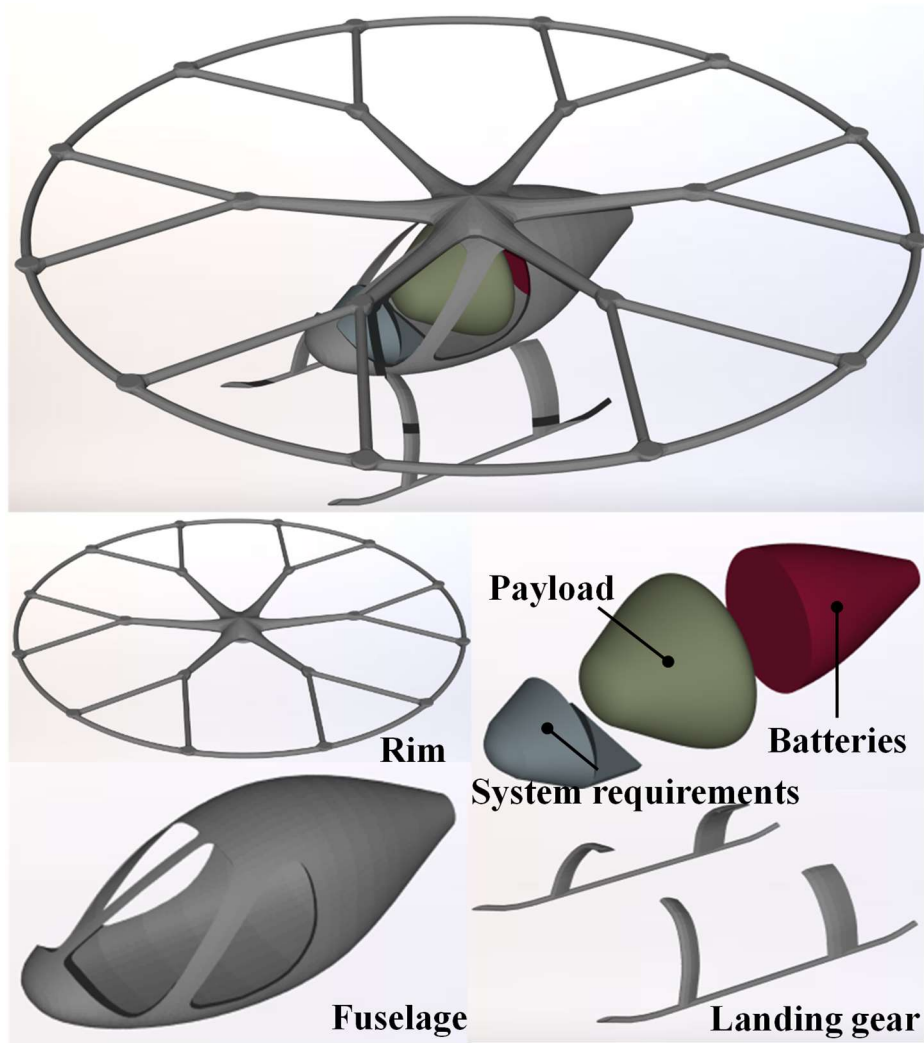
Fig. 5-1 Hypothetical model of a wingless-type eVTOL
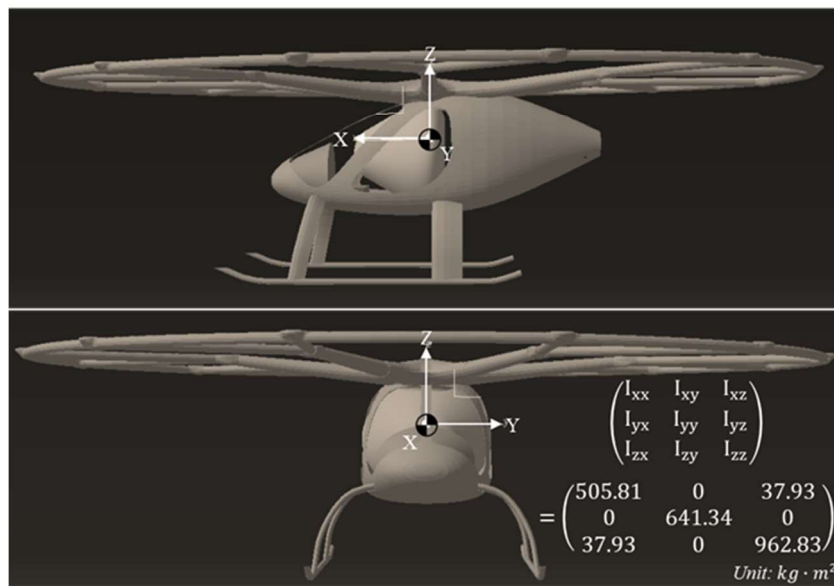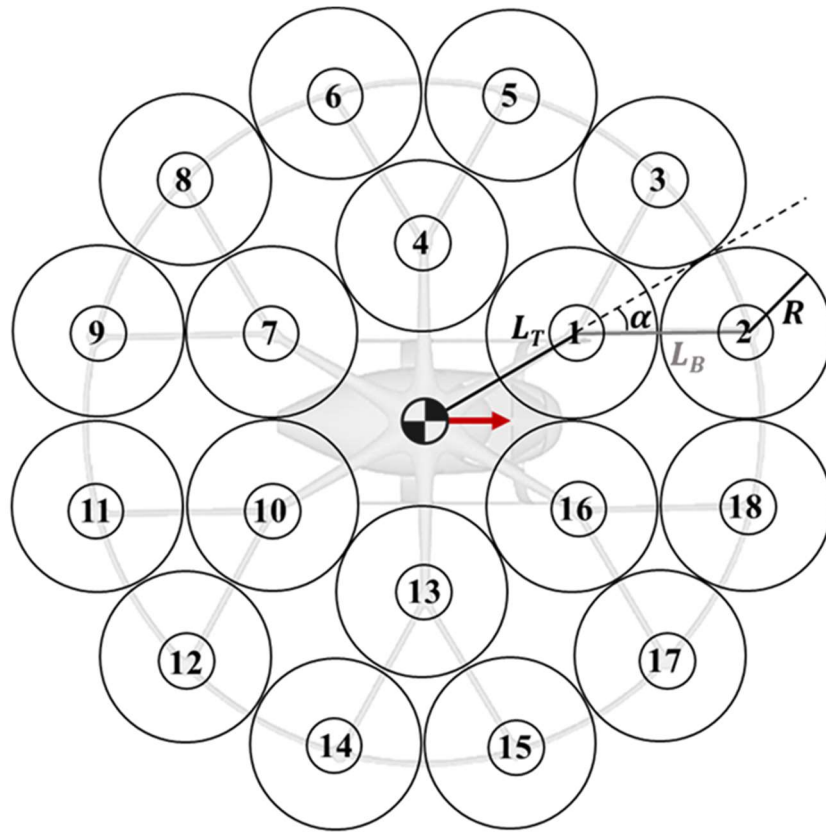
Fig. 5-2 Number of rotors and moment of inertia at the center of gravity

Table 5-1. Weight breakdown of the hypothetical model

Component	Weight, kg	Reference
Rim	87.1	CAD model with carbon fiber material
Fuselage	60.5	
Landing gear	16	
Rotors	14.6	Carbon fiber material [88]
Motors	31.3	T-motor U15 KV100[††]
Batteries	80	INR 18650-30Q [80] with specific energy 250 Wh/kg at pack level
System requirements	24.1	Airbus helicopter H-125 brochure [†]
Payload	160	2 passengers
Total	473.6	
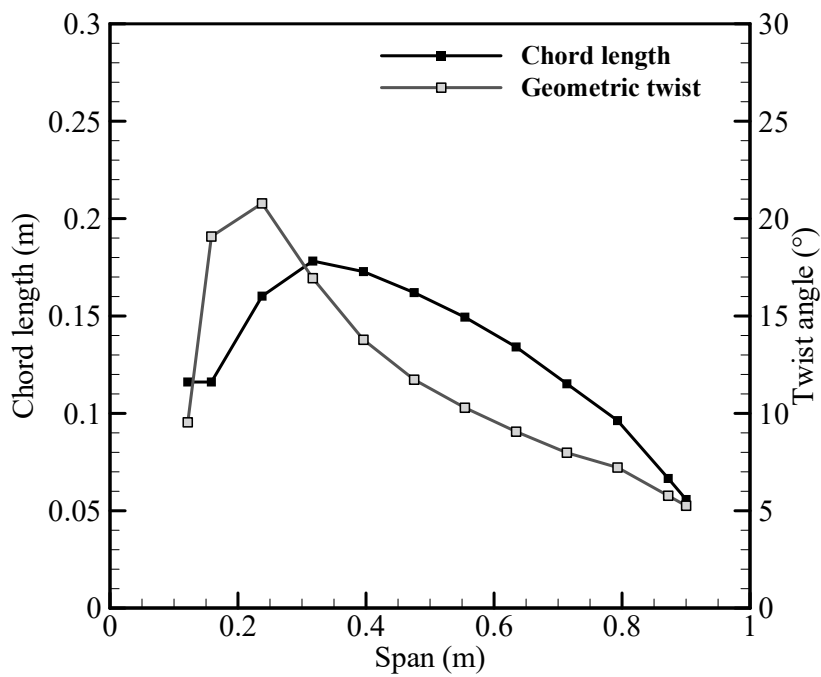
Fig. 5-3 Chord length and twist angle of the hypothetical model's rotor

blades

82

5.2　　Rotor rotation directions and aerodynamic performance

To investigate rotor-rotor interference of the hypothetical model based on the Volocopter-type eVTOL, the body frame consisted of rim, fuselage, and landing gear and virtual rotor disks of 18 rotors were imposed together on the same computational domain. The significance of the rotor-rotor interference is the concurrent interaction between the aerodynamic force of one rotor and induced velocities from the other rotors and body frame. A rotating front rotor generates its aerodynamic force and induced velocity. In forward flight, the induced velocity from the front rotor affects the aerodynamic forces of the rear rotors and the body frame. These induced velocities and aerodynamic forces of the rotors and body frame are needed to be concurrently and iteratively calculated in the same computational domain. Therefore, induced velocities and aerodynamic forces of the 18 rotors and body frame were concurrently analyzed by ADM in the same computational domain. It was considered that the induced velocities from one rotor affected the aerodynamic forces of the other rotors and body frame in forward flight as shown in Fig. 5-4.
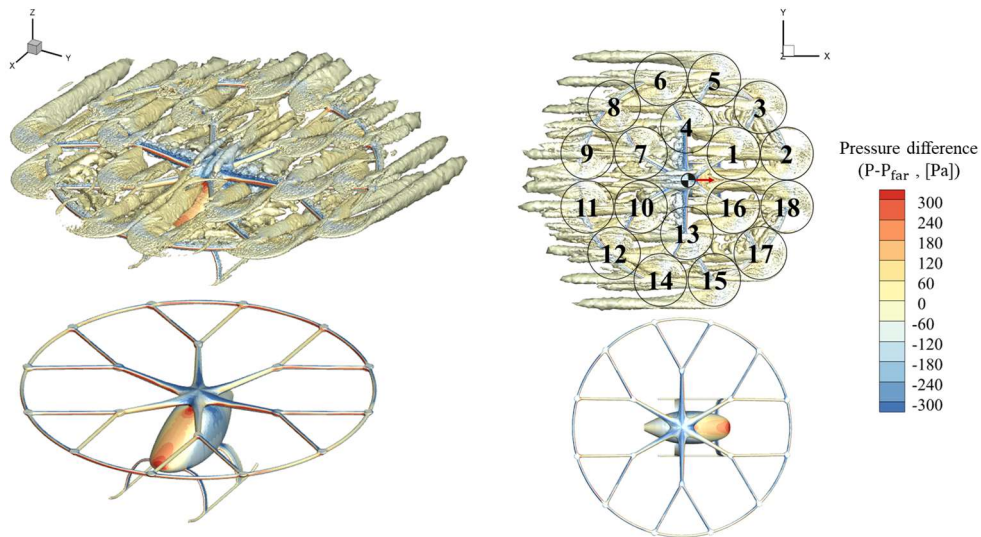
Fig. 5-4 ADM analysis including virtual rotor disks and fuselage of the hypothetical model in forward flight at 100 km/h (Iso-surfaces for Q = 50 with color-coded pressure difference)

The effect of rotor–rotor interference was investigated for three rotor rotation directions, called Hexa-like, Volocopter-like, and FRRA, as shown in Fig. 5-5. All configurations have eighteen rotors mounted on a frame that consists of an external rim and six Y-bars extending from the center point of the configuration to the rim. The only difference of each configuration is the direction of rotation of the rotors. In Heax-like, three rotors mounted on a Y-bar rotate in the same direction. In Volocopter-like, the direction is identical to a Volocopter 2X model described in the previous study [66]. In the FRRA direction, the retreating side of the front rotor and the advancing side of the rear rotor are aligned in a straight line during forward flight. This is a new direction proposed in this paper in Section 3.5.

84
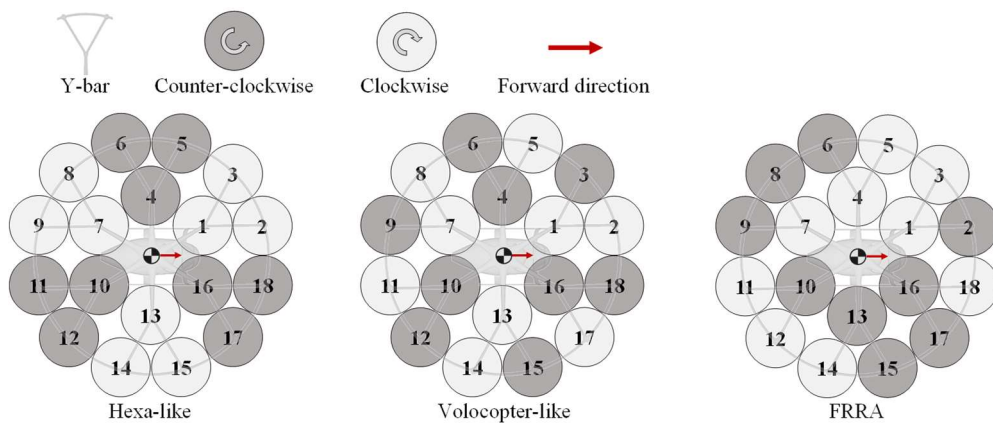
Fig. 5-5 Three combinations of rotation directions

For each direction, an ADM analysis was conducted for three flight conditions: hovering, forward flight at 100 km/h, and forward flight at 100 km/h with a yaw angle of 30° to represent a side wind. To compare the aerodynamic performance due only to rotor–rotor interference in the ADM analysis, the speed of all rotors was set to 928 rpm. Settings such as the rotor disk element size, far-field, and time step were the same as used to validate ADM. Iso-surfaces for Q = 500 with color-coded vertical velocities are shown in Fig. 5-6 for the FRRA direction for each flight condition, as calculated by ADM.

Hover flight

Forward flight at 100 km/h

Forward flight in side wind at 100 km/h

U_Z (- : downwash)

-10 -8 -6 -4 -2 0 2 4 6 8 10
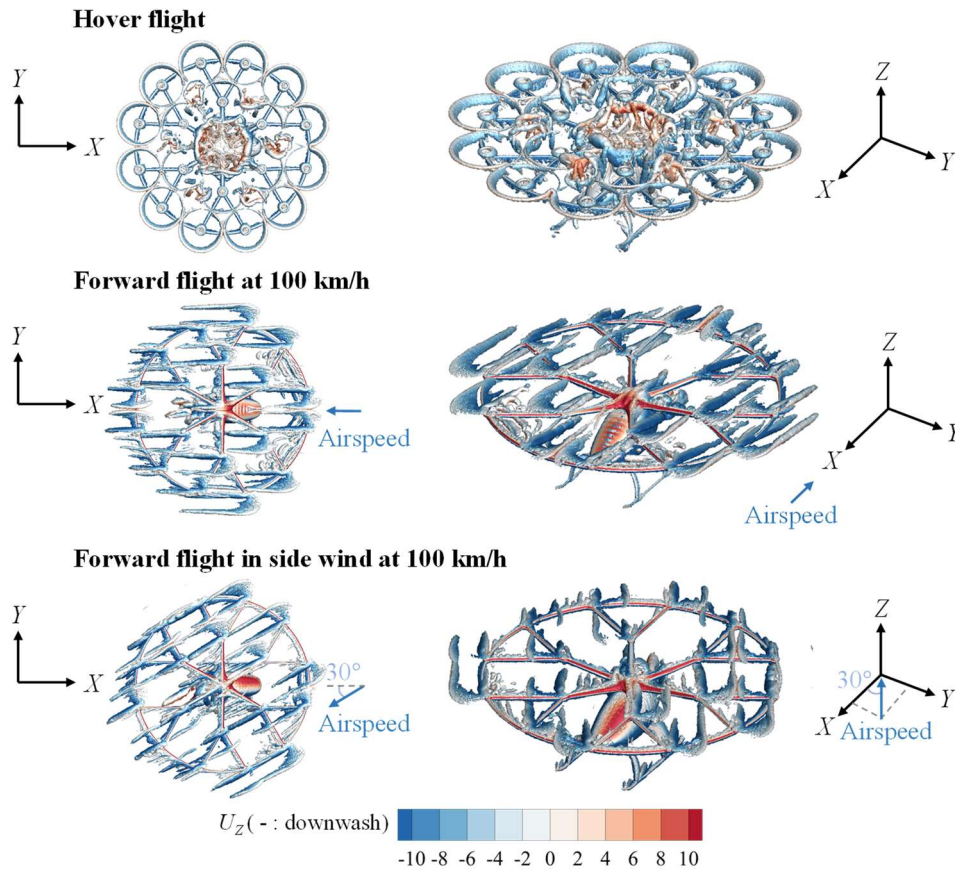
Fig. 5-6 Iso-surfaces for Q = 500 with color-coded vertical velocities for

FRRA

5.2.1 Hover flight

As shown in Fig. 5-7 for the three rotation directions, the difference in the average thrust and mechanical power coefficient of all rotors was below 1%, which is considered to be a negligible difference. When hovering, there is no advancing side and no retreating side for a rotor. Accordingly, the difference in aerodynamic performance due to the rotation directions was insignificant.

86

Hexa-like

Total thrust : 2.09 kN
Total power : 14.6 kW

Volocopter-like

Total thrust : 2.09 kN
Total power : 14.6 kW

FRRA

Total thrust : 2.07 kN
Total power : 14.5 kW

$\Delta C_T / \Delta r$

0   0.005   0.01   0.015   0.02   0.025   0.03
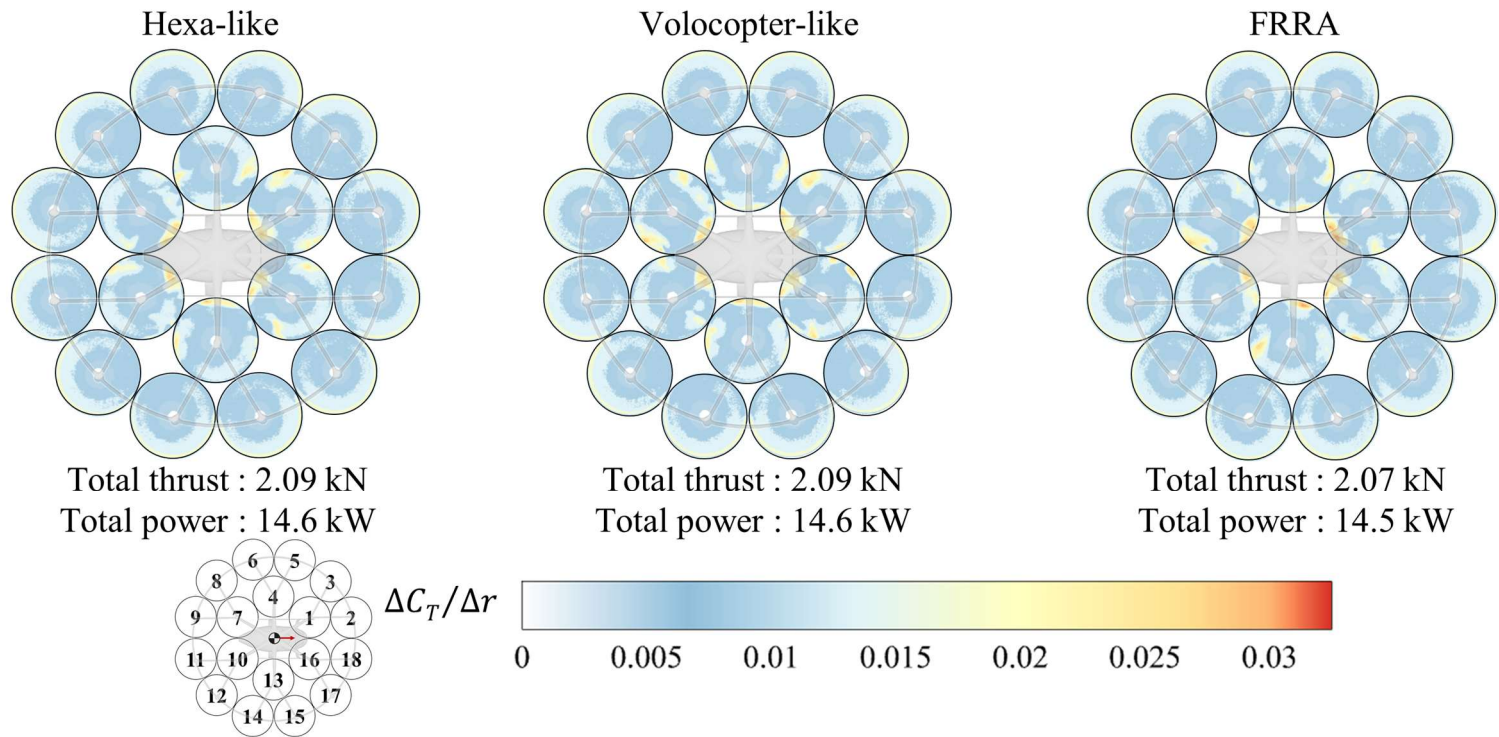
Fig. 5-7 Sectional thrust coefficient in hover flight(untrimmed rotor thrust)

5.2.2 Forward flight at 100 km/h

To evaluate a high-speed forward flight condition, the ground speed for forward flight was set to 100 km/h with a 8° nose-down pitch attitude. Unlike the results for the hover flight, the thrust for each rotor was mainly generated at the advancing side, as shown in Fig. 5-8. The front rotors (1st, 2nd, 3rd, 16th, 17th, and 18th) generated high thrust on the advancing side, regardless of the rotation direction. However, for the Hexa-like and Volocopter-like directions, the rear rotors close to the fuselage (7th and 10th) generated less thrust than in the FRRA direction. The reason is that the advancing sides of the 7th and 10th rotors were aligned in a straight line with the advancing sides of the 4th and 13th rotor placed in front of them. As shown in Fig. 5-9, the strong downwash generated from the advancing sides of the 4th and 13th front rotors flowed into the advancing sides of the 7th and 10th rear rotors. Thus, the thrust of these rear rotors was reduced due to the downwash. For this reason, the rearmost rotors (9th and 11th) in the Hexa-like direction generated less thrust than in the Volocopter-like and FRRA directions. The average thrust and mechanical power coefficient of all rotors in the Hexa-like direction were 0.00762 and 0.0005182, respectively. The Volocopter-like direction had a 4% higher thrust coefficient and 2% lower mechanical power coefficient than the Hexa-like direction. The FRRA direction had a 7.8% higher thrust coefficient and 4% lower mechanical power coefficient than the Hexa-like direction.

Hexa-like

Total thrust : 3.07 kN
Total power : 18.3 kW

Volocopter-like

Total thrust : 3.2 kN
Total power : 17.9 kW

FRRA

Total thrust : 3.31 kN
Total power : 17.5 kW

$\Delta C_T / \Delta r$
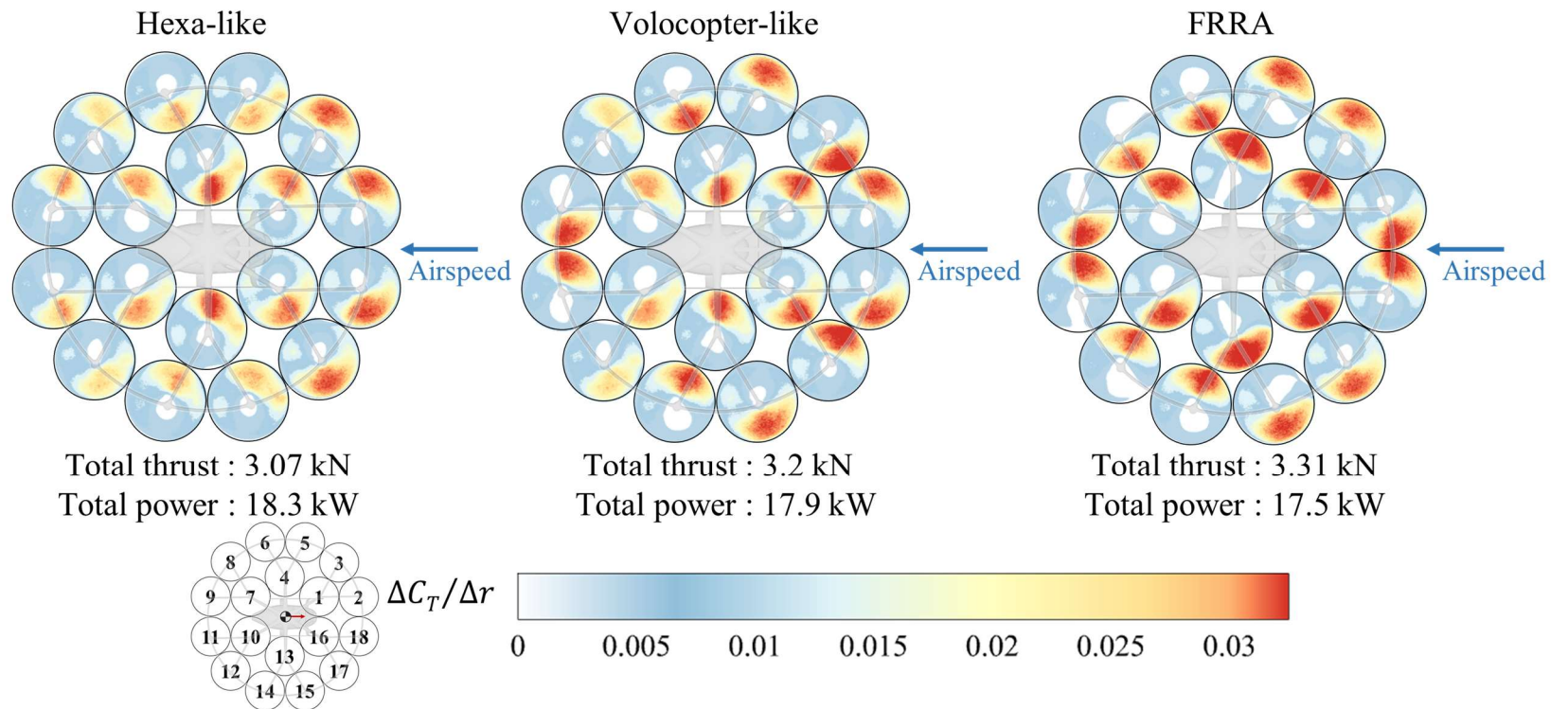
Fig. 5-8 Sectional thrust coefficient in forward flight at 100 km/h (untrimmed rotor thrust)

89
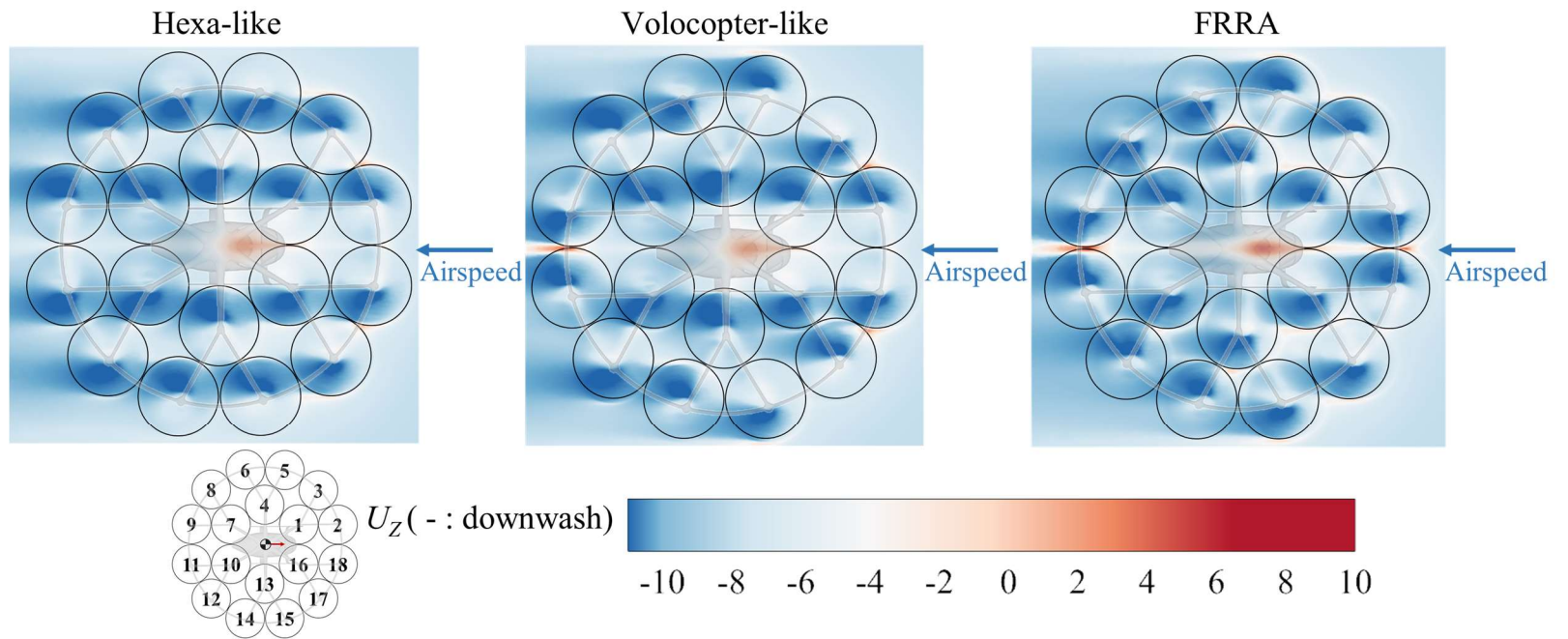
Fig. 5-9 Vertical velocity in forward flight at 100 km/h

The effect of downwash, which is the major factor in the thrust reduction of the rear rotors, is shown in Fig. 5-10. The vertical velocity difference ΔU_Z is negative (blue regions) on most of the advancing side of each of the rear rotors. This means that the most of the advancing sides of each of the rear rotors in the Hexa-like direction is affected by a strong downwash from the advancing sides of the front rotors. In contrast, ΔU_Z for the advancing sides of most of the rear rotors in the FRRA direction is positive (red regions). Thus, the strong downwash from the advancing sides of the front rotors did not flow into the advancing sides of the rear rotors. Therefore, the FRRA direction minimizes the thrust loss of the rear rotors due to rotor–rotor interference in a wingless-type eVTOL.
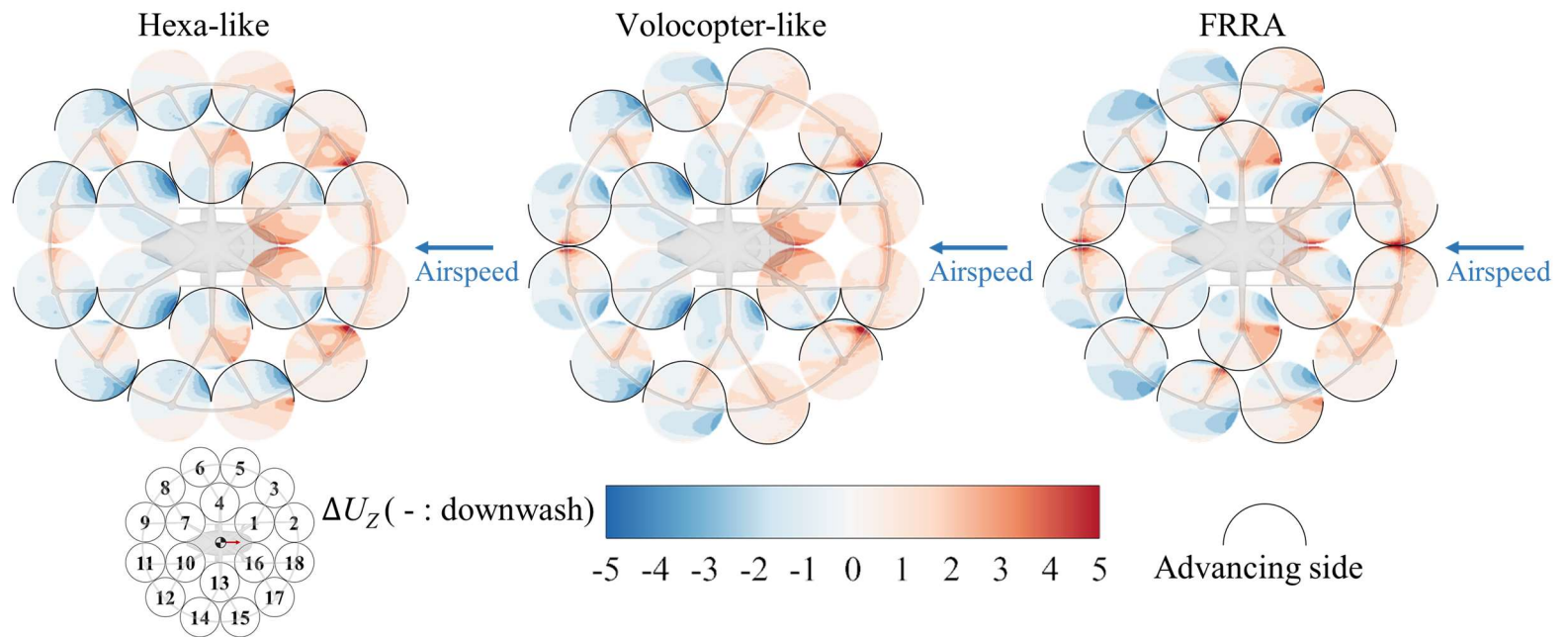
Fig. 5-10 Vertical velocity differences between multiple rotors and an isolated rotor in forward flight at 100 km/h

5.2.3 Forward flight in the airspeed of 100 km/h with 30° yaw angle

To investigate the aerodynamic performance of the rotors in a side wind, forward flight was analyzed when the airspeed was 100 km/h at a yaw angle of 30°. The sectional thrust coefficient is shown in Fig. 17. The average thrust coefficient of the rotors in the Hexa-like direction was 0.008349, and the mechanical power coefficient was 0.000502. In the Volocopter-like direction, the thrust coefficient was 1.4% lower and the mechanical power was 1.6% higher than for the Hexa-like direction. In the FRRA direction, the thrust coefficient was 2.8% lower and the mechanical power was 1.6% higher than for the Hexa-like direction. The results show that when the airflow was at a yaw angle of 30°, the aerodynamic performance was better for the Hexa-like direction than for the FRRA direction. The reason for the better performance of the Hexa-like direction is that, as shown in Fig. 18, the angle of influx of the downwash from the front rotors had changed due to the side wind, so that the downwash mainly flowed into the retreating side of the rear rotors. For the FRRA direction, the downwash from the front rotors flowed into the advancing sides of most of the rear rotors, which was disadvantageous in a side wind, such as an airflow with a 30° yaw angle. Therefore, the FRRA direction had the desirable aerodynamic performance when the airspeed was 100 km/h without a side wind, but when the airflow had a yaw angle, the aerodynamic performance was slightly worse.

93

Hexa-like

Total thrust : 3.36 kN
Total power : 17.7 kW

Volocopter-like

Total thrust : 3.32 kN
Total power : 18 kW

FRRA

Total thrust : 3.27 kN
Total power : 18.1 kW

$\Delta C_T/\Delta r$

0   0.005   0.01   0.015   0.02   0.025   0.03
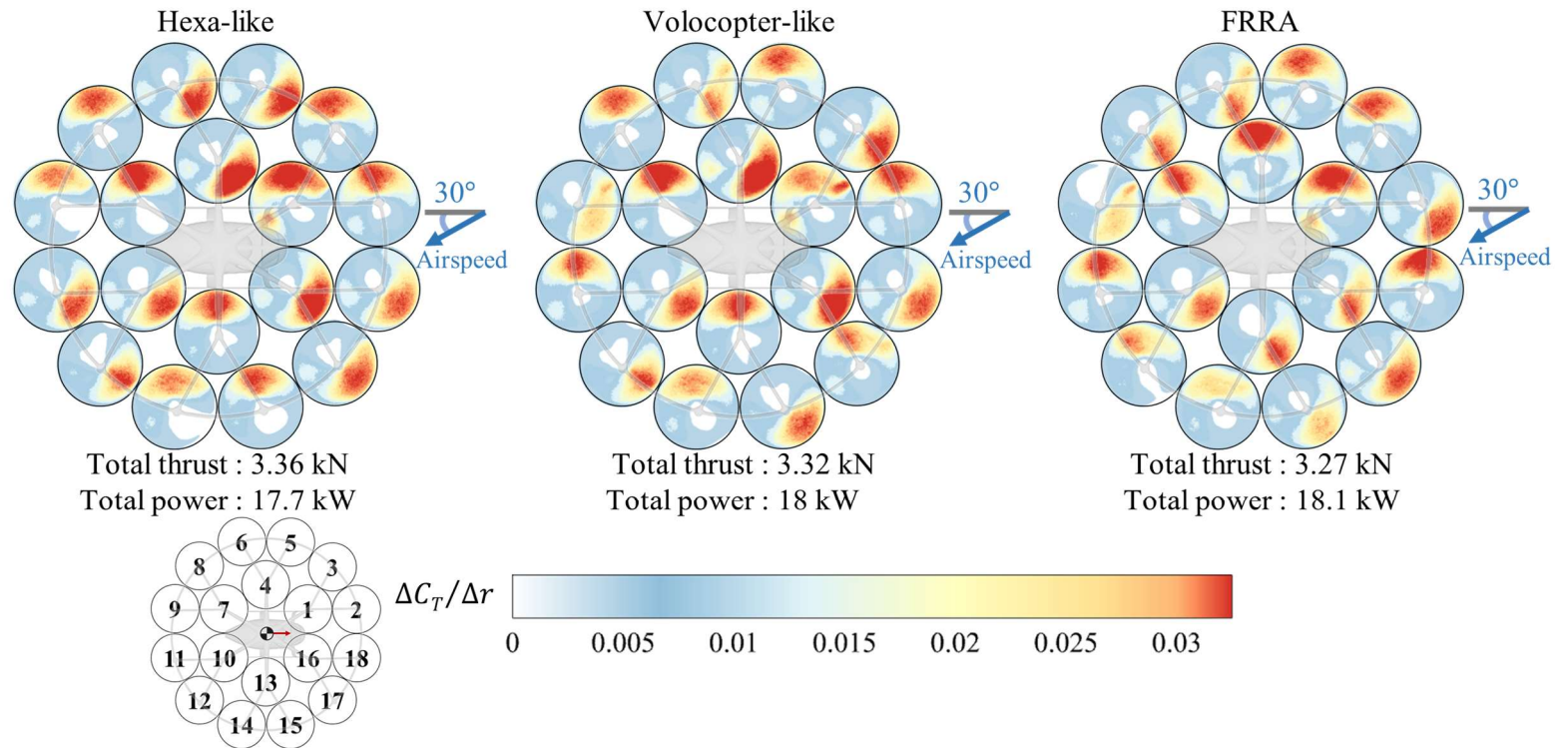
Fig. 5-11 Sectional thrust coefficient in the airspeed of 100 km/h with 30° yaw angle (untrimmed rotor thrust)
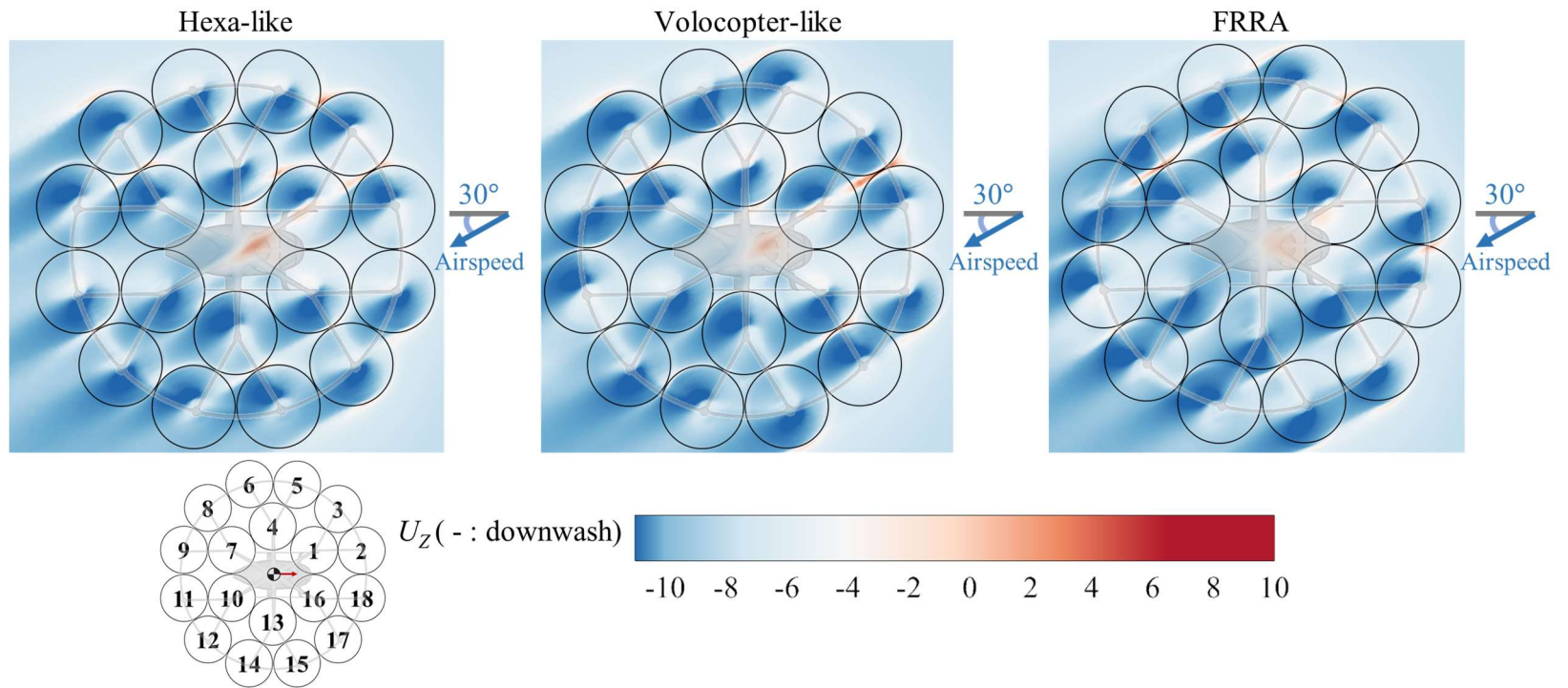
Fig. 5-12 Vertical velocity in the airspeed of 100 km/h with 30° yaw angle

In summary, the difference in the rotor thrust for the Hexa-like, Volocopter-like, and FRRA directions was insignificant in hover flight. However, in high-speed forward flight, the rear rotors lost some thrust due to the downwash from the advancing sides of the front rotors, which flowed into the advancing sides of the rear rotors. The angle of the downwash flowing into the rear rotors depends on the side wind. Even if there is no loss of thrust by the rear rotors in an environment without a side wind, some thrust will be lost in a side wind. In actual operation of a wingless-type eVTOL, it was judged that the speed of a side wind speed compared to the forward speed will be insignificant, so this study mainly focuses on flight performance without a side wind. If the speed of the side wind is low compared to the ground speed, then the Hexa-like direction performs less well aerodynamically due to rotor–rotor interference because the advancing sides of the front and rear rotors are aligned in a straight line. On the other hand, the FRRA direction has better aerodynamic performance as there is weaker rotor–rotor interference because the downwash from the advancing sides of the front rotors does not flow into the advancing sides of most of the rear rotors.

5.3 Surrogate models including the rotor-rotor interaction effect

It was judged that Hexa-like and FRRA rotation directions were representative directions of the worst and the best aerodynamic performance in generic mission operations, respectively. Flight performance was evaluated with the flight simulation framework developed by building surrogate models with ADM for the Hexa-like and

96

FRRA directions. The range of airspeeds and rotor speeds that cover the operable conditions of the hypothetical model are listed in Table 5-2. Latin hypercube sampling was used to choose 58 points for the ADM analysis of both the Hexa-like and FRRA directions. The surrogate model was constructed as a fourth-order RSM. Fig. 5-13 compares the values predicted by RSM with those from the ADM analysis. In the Hexa-like rotation direction, the R-squared values at climb were 0.97 and 0.91 for the average thrust and mechanical coefficients of all rotors, respectively. Also, the R-squared values at descend were 0.97 and 0.96 for the average thrust and mechanical coefficients of all rotors, respectively. In the FRRA rotation direction, the R-squared values at climb were 0.97 and 0.92 for the average thrust and mechanical coefficients of all rotors, respectively. Also, the R-squared values at descend was 0.99 for both average thrust and mechanical coefficients of all rotors, respectively. It was determined that the surrogate models were properly constructed. Detail values of the surrogate model are shown in Appendix B and C.

Table 5-2. Ranges of airspeeds and rotational speeds for the surrogate models

Dimension	Lower value	Upper value	Unit
Airspeed in X-axis of body frame, U_a	−30	10	m/s
Airspeed in Y-axis of body frame, V_a	20	−20	m/s
Airspeed in Z-axis of body frame, W_a	−5	2	m/s
Rotational speed of rotors	800	1800	rpm
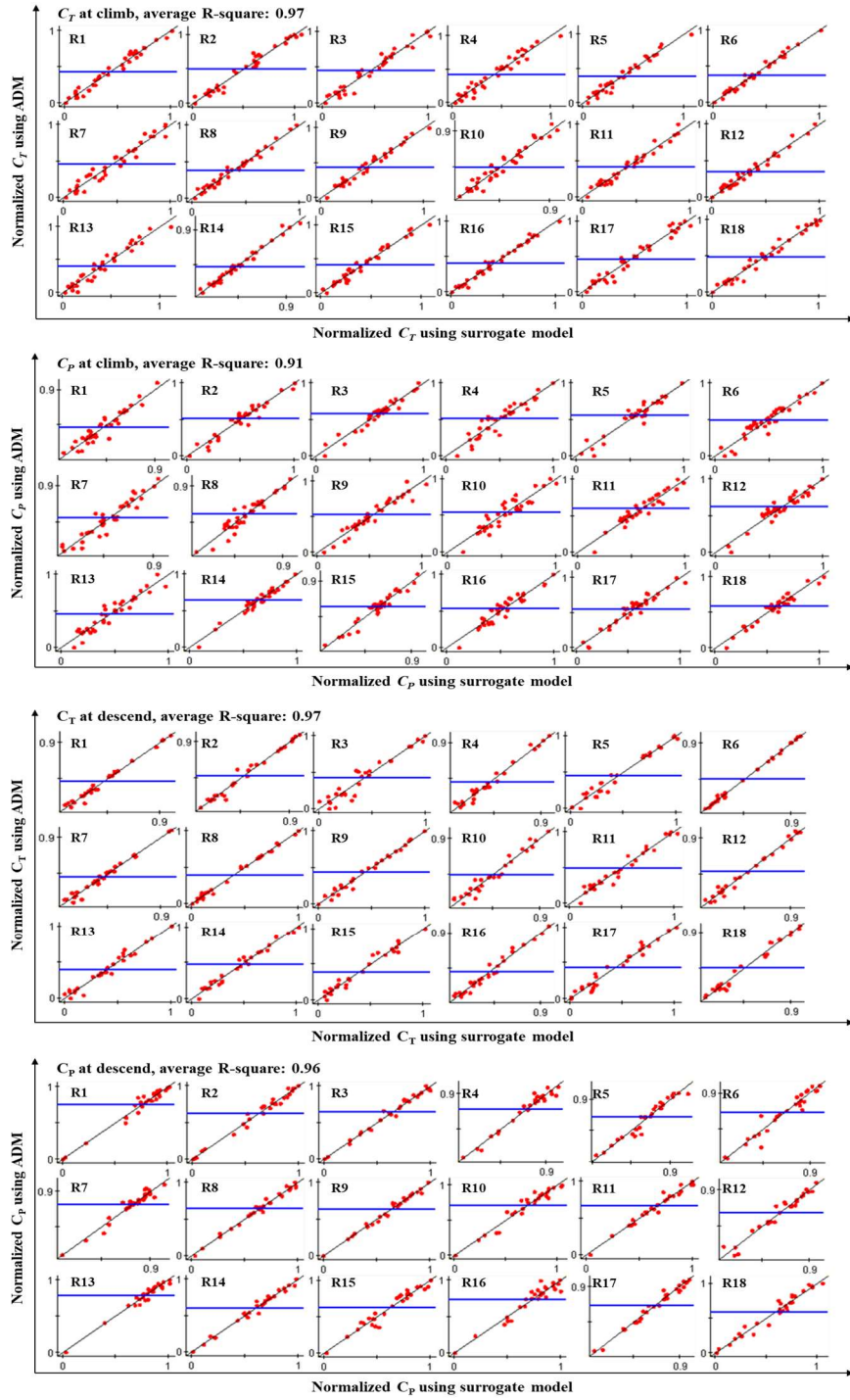
Fig. 5-13 RSM of normalized thrust and power coefficients of each rotor in the Hexa-like rotation direction

5.4   Simulation results

A generic mission profile shown in Fig. 5-14 was input as the target path and flight conditions into the flight simulation framework. The ground speeds when cruising mission were in the range 70 to 100 km/h, which is based on the maximum cruise speed of the Volocopter 2X model. The flight performance for the directions was evaluated by calculating the flight range to the point where the total depth of discharge of the battery in the landing mission segment was 80% for each ground speed.
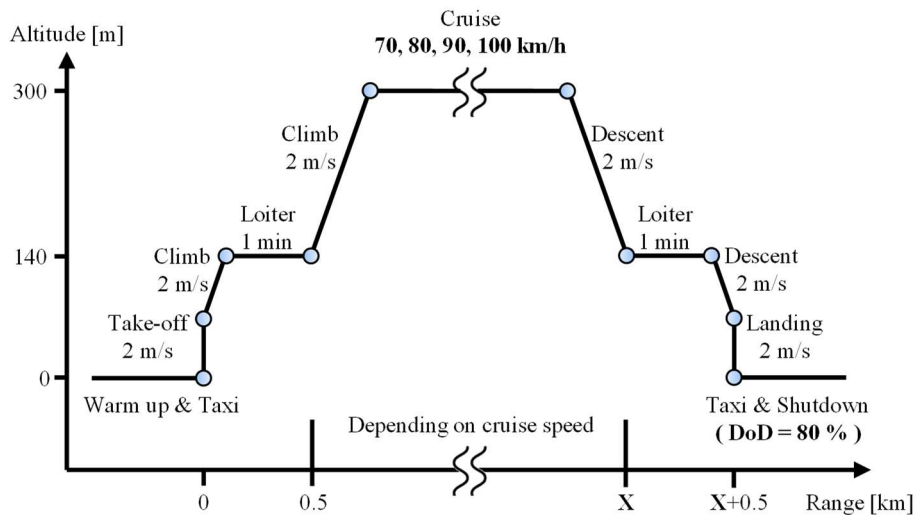
Fig. 5-14 Mission profile with ground speeds from 70 to 100 km/h

To evaluate whether there were differences in attitude control and trajectories for the Hexa-like and FRRA directions, a flight was simulated with a ground speed of 100 km/h and a range of 20 km. As shown in Fig. 5-15, Three cases of Hexa-like, FRRA, and FRRA (tuned PID gains) was simulated. Hexa-like and FRRA cases controlled with the same PID gains, and the FRRA (tuned PID gains) case controlled

99

with manually tuned PID gains as shown in Appendix-A. Although the rotation directions were different, the attitude angles, velocities, and trajectories of Hexa-like and FRRA (tuned PID gains) were similar and there was no significant position error from the target path.
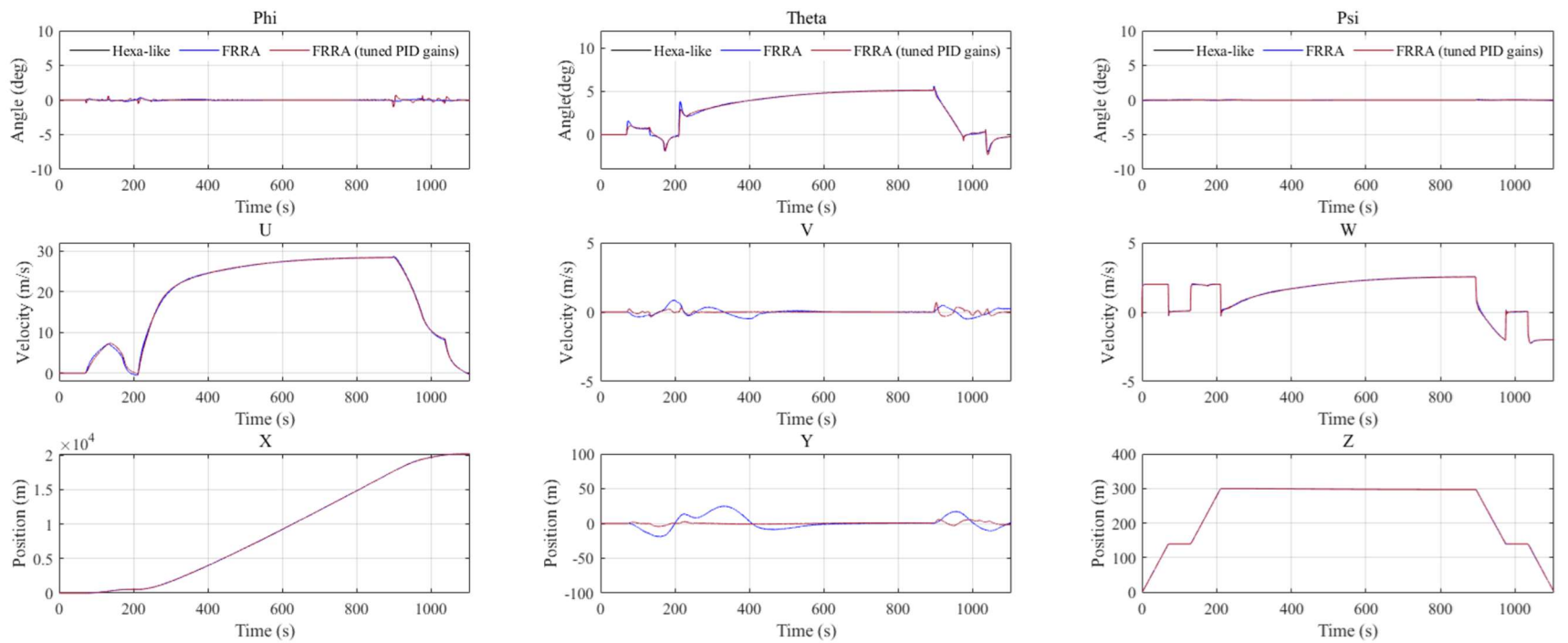
Fig. 5-15 Attitudes, velocities, and trajectories of the Hexa-like and FRRA for a ground speed of 100 km/h.

The detail results of the flight performance for each mission segment with trimmed rotor thrust fed back from control and dynamics analysis in Fig. 5-15 is shown in Table 5-3 and Fig. 5-16. In both rotation directions, the trend of the required mechanical and electric powers with respect to mission segment type was similar. In climb mission segment, the mechanical power of all rotors was 47 kW or more and the electric power of all motors was 56 kW or more, which was higher required powers than other mission segments. In the descent mission segment, the mechanical power of all rotors was 40 kW or less and the electric power of all motors was 47 kW or less. Although the same vertical velocity was required as the mission condition, such as the climb of 2nd and 4th segments and descent of 6th and 8th segment, the required powers of 4th and 8th segments were lower than those of 2nd and 6th segments, respectively. The reason for the lower powers was that if the previous mission segment was forward flight such as cruise or loiter, the decelerating forward velocity would result in a forward + upward or forward + downward motion, and the required mechanical power of rotors would be reduced by the forward freestream at this time.

After the mission operation, there was a difference of 7 % in the final depth of discharge(DoD) of batteries with respect to Hexa-like and FRRA rotation directions. This difference of DoD mainly was induced by the difference of required mechanical and electric powers in cruise mission segment, which occupied the most time of 63 % of the total operation time. In the cruise mission, the mechanical power of all rotors in Hexa-like and FRRA rotation direction was 27.4 kW and 23.9 kW, respectively,

102

with a 15 % difference, and the electric power of all motors was 35.3 kW and 31.7 kW, respectively, with an 11 % difference. Therefore, FRRA rotation direction required less mechanical and electric powers and was more desirable than those of Hexa-like in trimmed rotor thrust conditions.

Table 5-3. Comparison of flight performance with respect to Hexa-like and FRRA rotation direction in each mission segment

Performance	Rotation direction	Mission segment								
		Take-off	Climb	Loiter	Climb	Cruise	Descent	Loiter	Descent	Landing
Mechanical power (kW)	Hexa-like	50.8	50.8	41.1	45.1	27.4	19.5	30.4	40.2	45.9
	FRRA	51.5	51.5	36.2	47.9	23.9	16.7	27.8	35.6	39.5
Difference in mechanical power		1%	1%	-14%	6%	-15%	-17%	-9%	-13%	-16%
Electric power (kW)	Hexa-like	60.1	60.0	50.0	54.0	35.3	26.7	37.7	47.7	53.5
	FRRA	60.8	60.8	44.9	56.7	31.7	23.9	35.2	43.1	47.1
Difference in electric power		1%	1%	-11%	5%	-11%	-12%	-7%	-11%	-14%
Thrust (kN)	Hexa-like	4.68	4.65	4.63	4.66	4.66	4.62	4.66	4.61	4.64
	FRRA	4.68	4.65	4.63	4.66	4.66	4.62	4.66	4.61	4.64
DoD until the mission segment	Hexa-like	3%	6%	11%	18%	56%	59%	63%	67%	71%
	FRRA	3%	7%	11%	18%	51%	54%	58%	60%	64%
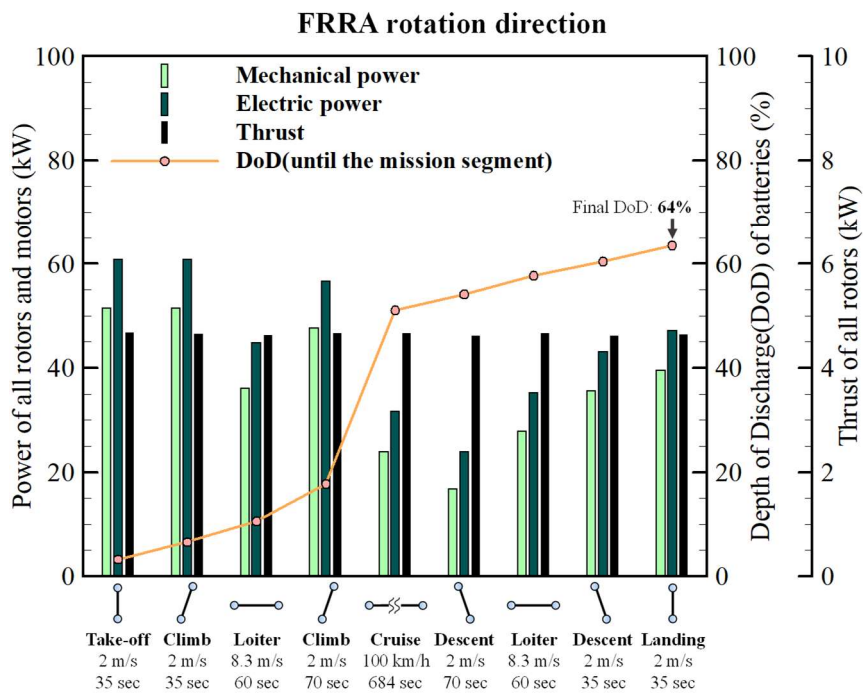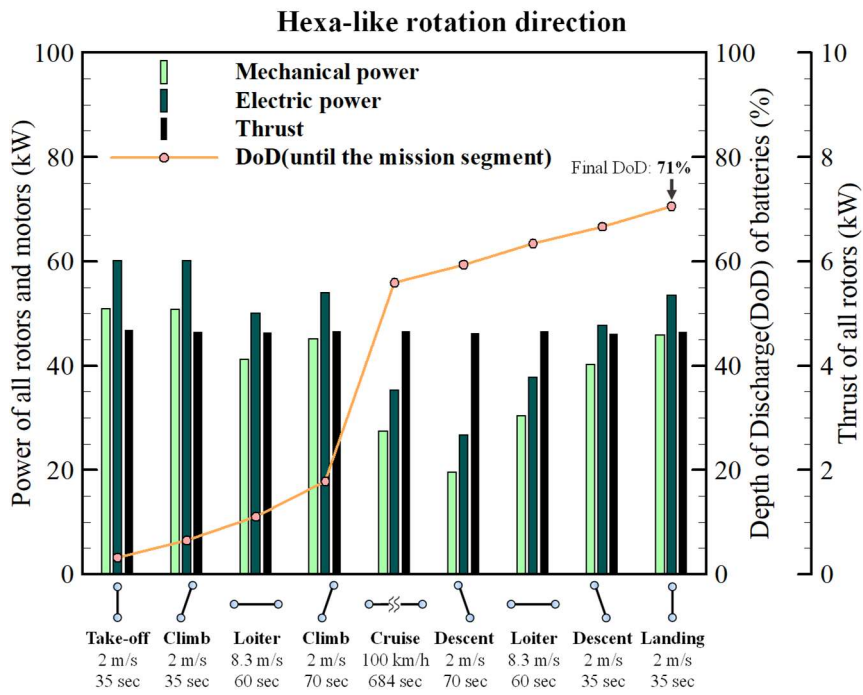
Fig. 5-16 Required powers and depth of discharge in each mission segment

(trimmed rotor thrust)

In the cruise mission segment, there was a difference in the rotational speed and mechanical power of each rotor between the Hexa-like and FRRA directions. When the ground speed reached 100 km/h, as shown in Fig. 5-17, the maximum thrust for both directions was for the 11th rotor, one of the rearmost rotors. The maximum thrust was 295.8 N in the Hexa-like direction and 284.4 N for the same rotor in the FRRA direction. The minimum thrust in the Hexa-like direction was 234.8 N, which occurred for the 7th rotor. For the FRRA direction, it was 238 N, which occurred for the 1st rotor. The total thrust of all rotors was 4,665 N for both directions, but due to rotor–rotor interference, the converged thrust of each rotor had a larger deviation in the Hexa-like direction than in the FRRA direction.

In the Hexa-like direction, the maximum rotational speed of 1,219 rpm occurred for the 11th rotor, and the minimum rotational speed of 965 rpm occurred for the 2nd rotor. The average rotational speed of all rotors converged to 1,092 rpm in the Hexa-like direction and 1,035 rpm in the FRRA direction. The rotational speed of each rotor had a larger deviation in the Hexa-like direction than in the FRRA direction. Even though the total thrust for all the rotors was identical for both directions, the mechanical power required to maintain the thrust and rotational speed of each rotor also depends on the direction. In the Hexa-like direction, the maximum mechanical power was 2,399 W, which occurred for the 11th rotor, a rearmost rotor. The minimum mechanical power was 1,105 W, which occurred for the 2nd rotor. In the FRRA direction, the maximum mechanical power was 1,803 W for the 9th rotor, the other rearmost rotor, and the minimum mechanical power was 885 W for the 18th

rotor. The maximum thrust, rotational speed, and mechanical power were generated in the rearmost rotors for both directions, since better control is achieved by generating a pitching moment with those rotors. Even at the same ground speed, rotor–rotor interference causes a difference in aerodynamic performance for the directions. The mechanical power for each motor and the rotational speed to be maintained are different for the directions.
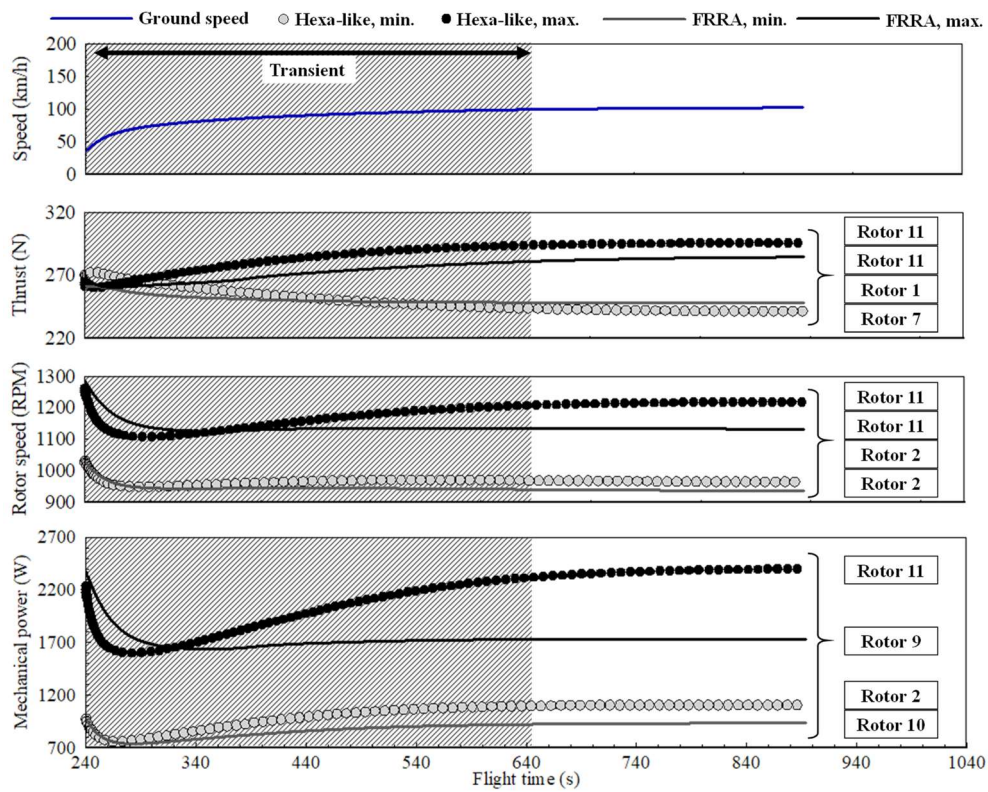
Fig. 5-17 Minimum and maximum values of rotor speed control, thrust, and required mechanical power of the Hexa-like and FRRA directions for a ground speed of 100 km/h

107

From the flight performance analysis for several ground speeds, the average performance of all rotors and motors for each ground speed compared to a ground speed of 70 km/h is shown in Fig. 5-18 for both directions. In both, the required mechanical and electric power increased as the ground speed increased. For the Hexa-like direction, when the ground speed was increased from 70 to 100 km/h, the mechanical power increased by 50%, the electric power increased by 37%, and the driving current increased by 48%. To compensate for the thrust loss of the rear rotors due to rotor–rotor interference at a ground speed of 100 km/h, the rotational speed of the rear rotors was increased by 7% to maintain the pitch attitude. For the FRRA direction, when the ground speed was increased from 70 to 100 km/h, the mechanical power increased by 14%, the electric power increased by 11%, and the driving current increased by 13%. Unlike the Hexa-like direction, the difference in rotational speed due to rotor–rotor interference at a ground speed of 100 km/h was negligible in the FRRA direction.

The difference in performance between the Hexa-like and FRRA directions is shown in Fig. 5-19. There was no significant difference in performance for a ground speed of 70 km/h. The rotational speed, mechanical and electric power, and driving current became lower for the FRRA direction as the ground speed increased. At a ground speed of 100 km/h, the rotational speed, mechanical power, electric power, and driving current were reduced for the FRRA direction by 5%, 21%, 17%, and 21%, respectively.
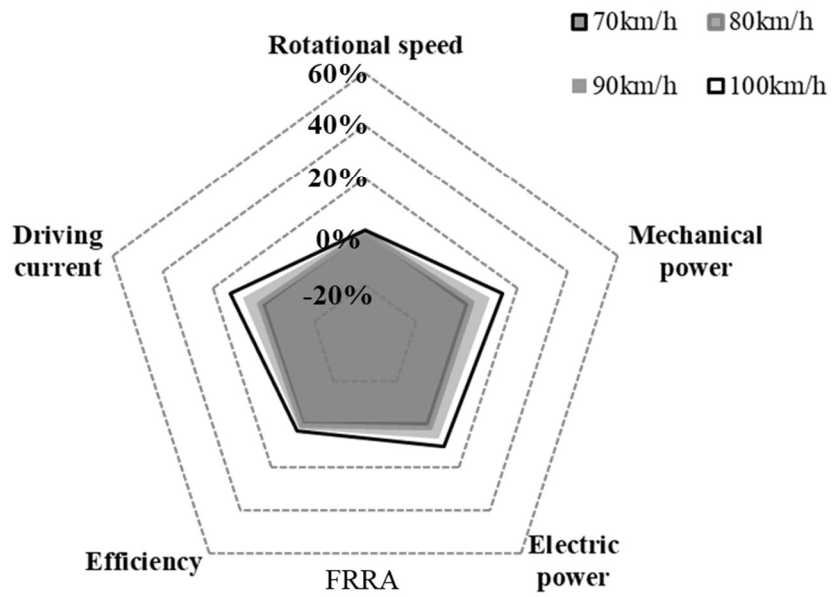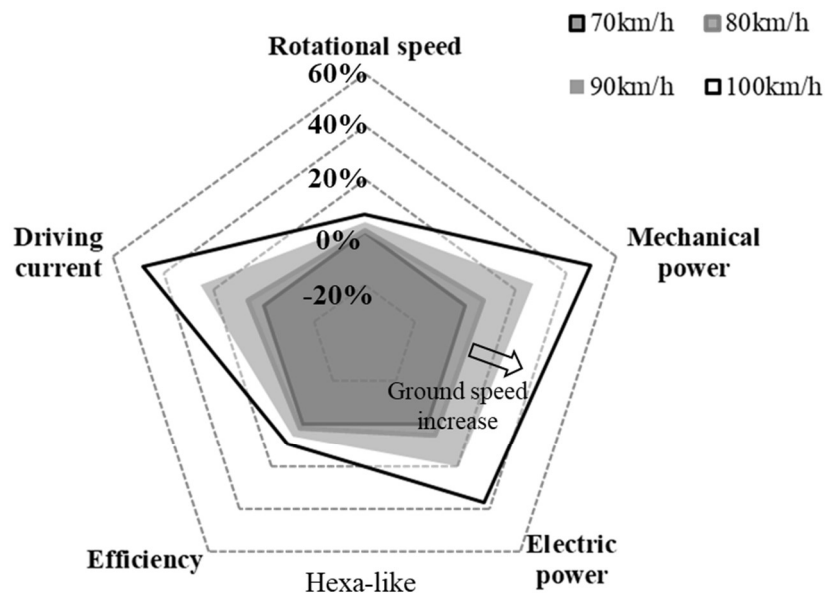
Fig. 5-18 Average performance for ground speeds from 70 to 100 km/h for the Hexa-like and FRRA directions
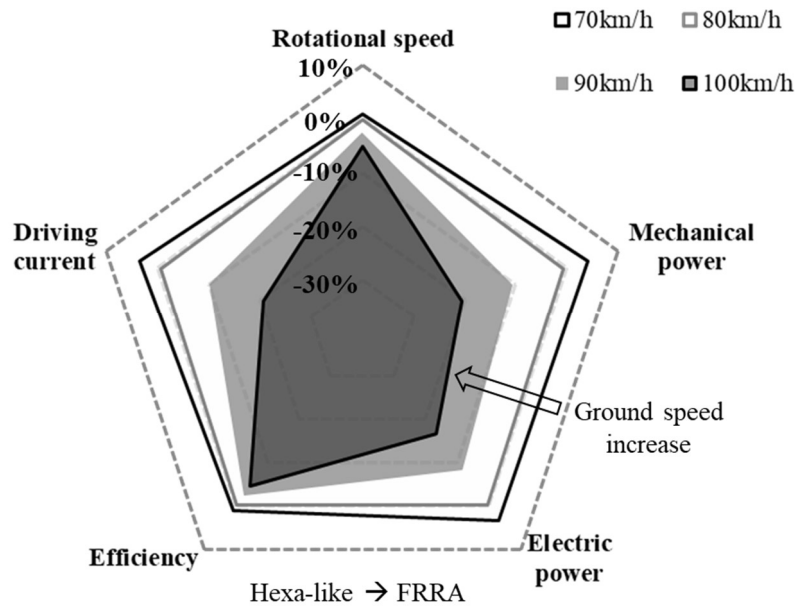
Fig. 5-19 Difference in performance between Hexa-like and FRRA directions

Based on the mission profile in Fig. 5-20, the range was calculated based on when the depth of discharge of the battery was 80% after landing, as shown in Fig. 26. With the Hexa-like direction, the range was predicted to be 20.8 km for a ground speed of 70 km/h. As the ground speed increased, the range also increased. For this direction, the range was 24.2 km for a ground speed of 100 km/h. For the FRRA direction, the range was predicted to be 21.3 km for a ground speed of 70 km/h. As the ground speed increased, the range again increased. It was 28.7 km for a ground speed of 100 km/h. The increase in range was minimal when changing from the Hexa-like to the FRRA direction for a ground speed of 70 km/h, but as the ground speed increased, the difference in the range increased to 18%.
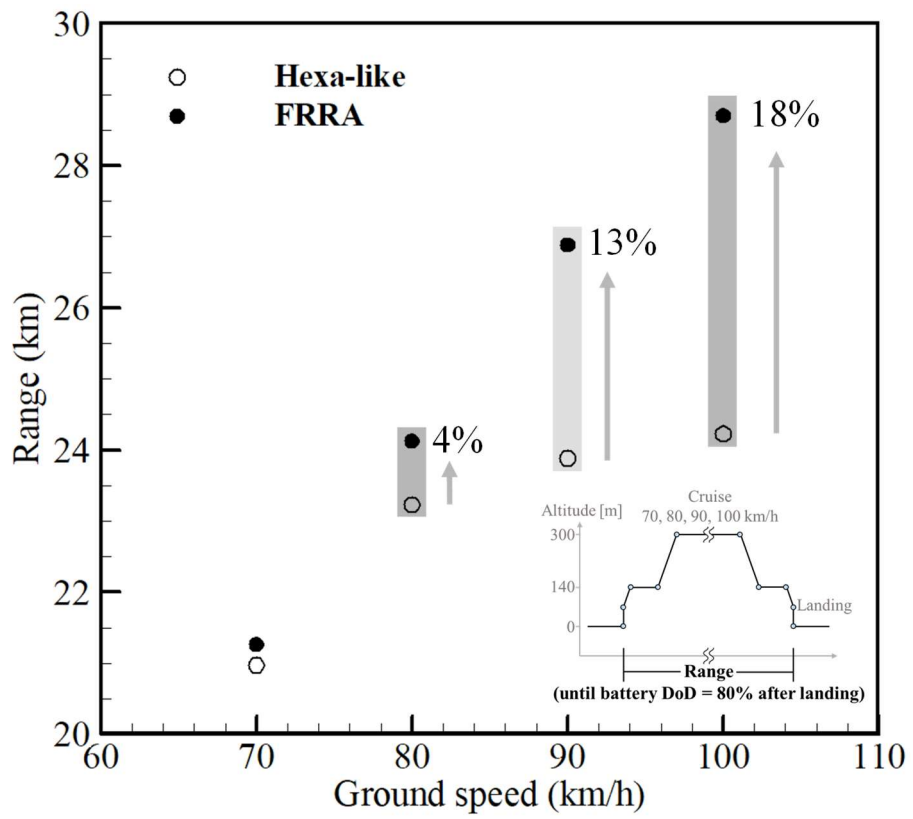
Fig. 5-20 Ranges with respect to Hexa-like and FRRA directions

111

Chapter 6.

Conclusion

6.1   Summary

Wingless-type eVTOL has the various advantages of efficient hover performance, low noisiness, and safety. The wingless-type eVTOL controls the rotating speed of its multiple rotors to maintain its ground speed and a stable attitude for a given flight path. The rotating speed of the rotors has to be changed continuously to achieve stable flight. Concurrently, the rotating speed and the loaded torque of the motors are also continuously changed. To predict the overall flight performance of a wingless-type eVTOL, a novel flight simulation framework is developed in this study. The framework is based on a series of multidisciplinary analysis including control, aerodynamic, EPS, and 6-degree-of-freedom (6-DOF) dynamics. In addition, the flight performance in actual operation can be properly predicted, considering the effects of external wind for the small UAVs and rotor-rotor interference for UAM service are considered.

Using the flight simulation framework with the add-on module of von Kármán wind turbulence model and Beaufort wind force scale, the tendency of excess battery energy and operable wind conditions is identified with respect to ground speed and wind speed of a wingless-type eVTOL for small UAV. Also, using the flight simulation framework with the add-on module of ADM for rotor-rotor interference,

variations in flight performance and operation range with respect to rotor rotation directions are predicted to investigate the desirable rotation direction of a wingless-type eVTOL for UAM service.

6.2   Originalities of the dissertation

The main originality of this dissertation is the development of a flight simulation framework to predict the flight performance of a wingless-type eVTOL including the control for the disturbances such as external winds and rotor-rotor interference. Moreover, the simulation framework has been validated, compared with experimental data of single rotor and wind resistance tests and numerical analysis results of tandem rotors and a quadrotor. Below are the detailed originalities and answers to three research questions of this dissertation.

1. This dissertation proposes a new flight simulation framework based on multidisciplinary analysis. In contrast to the traditional flight performance analysis tools based on steady level flight without considering the disturbances of wind and rotor-rotor interference, the proposed framework can predict the flight performance of a wingless-type eVTOL including the control for those disturbances. This is because the concurrent analyses are conducted in the framework:

   1) Rotation speeds of multiple rotors constantly controlled in the simulation for a stable flight under the disturbances using control analysis

   2) Aerodynamic thrust and torque by the controlled rotation speed

3) Electric propulsion performance by the controlled rotation speed and the torque loaded on the motors

Compared with experimental data and numerical benchmark tests, analysis modules of control, aerodynamic, and EPS in the simulation were validated to predict the flight performance such as attitude control, thrust and mechanical power of rotors, and the magnitude of voltage drop of batteries. In Chapter 3, the details are discussed.

2. This dissertation proposes a main characteristic of the flight performance of a wingless-type eVTOL for small UAV operating in wind disturbance. The characteristic is that even under the same wind condition, the flight performance is more inferior, when the ground speed of a wingless-type eVTOL is increased. Usually under the calm wind condition, flight performance is more superior in forward flight than in hover, until a certain ground speed. This is because required mechanical power, especially induced power of rotors, is decreased. In contrast of the calm wind condition, the wind disturbance fluctuates the pitch angle of the wingless-type eVTOL and the magnitude of the pitch angle is increased. In addition, the more increased ground speed is, the more increased the magnitude of the pitch angle is. As a result, required mechanical power is more increased at higher ground speed, even under the same wind disturbance. When the duty ratio is over 100 % at certain wind and ground speed conditions, it can be judged that a wingless-type eVTOL is not operable at the conditions. The duty ratio of motor is one of the standard indicators for evaluating the wind

resistance of a wingless-type eVTOL. The duty ratio usually has a lower value, when speed of rotor is lower and driving voltage of motor is higher at a same required thrust. It could be helpful to increase the wind resistance by large radius of rotors, high speed constant of motors, and high voltage of batteries. In Chapter 4, the details are discussed.

3. This dissertation proposes a concept of rotation direction, FRRA (Front rotor's Retreating side and Rear rotor's Advancing side). The loss of aerodynamic performance due to rotor-rotor interference is minimized in the FRRA concept, because the strong downwash from the front rotor's advancing side avoids the rear rotor's advancing side which most thrust of the rear rotor is generated. Multiple rotors rotated in FRRA shows desirable flight performance of decrease in mechanical power and consequently increase in operable range at high speed forward flight, compared with other rotation directions. The scale of benefits in flight performance using the FRRA concept have some uncertainty in yawed flow such as side wind condition. However, the uncertainty will be lower when the ground speed is higher, consequently the magnitude of yaw flow is negligible. In Chapter 5, the details are discussed.

4. In summary, the proposed framework achieves that it is a new methodology to overcome the limitation of conventional flight performance prediction methods available only in ideal conditions such as calm wind and no interference between rotors. This dissertation shows the flight performance of a wingless-type eVTOL including the control for wind disturbance and rotor-rotor

interference. As a result, remarkable characteristic and indicator for wind resistance and desirable rotation direction concept for rotor-rotor interference are suggested, which can be numerically predicted only by the concurrent analyses of control, aerodynamic, and EPS.

6.3   Future works

The flight simulation framework for wingless-type eVTOLs was successfully developed. However, there is still room for generality of eVTOL configuration and disciplinary.

In the generality of eVTOL configuration, there are various eVTOL concepts including a fixed wing, such as tilt-rotor and lift+cruise. To predict the flight performance for those concepts, control, aerodynamic and EPS analyses for operating the control surfaces in fixed wing aircrafts such as ailerons, elevators, and rudders is required. Moreover, the consideration of aerodynamic interference between wings and rotors is also required.

In the generality of disciplinary, structure analysis for fuselage, supporting bars, and landing gear is required. The FRRA direction, proposed rotation direction of rotors, is desirable for operation. However, it might be unfavorable for structures. The FRRA direction is specialized to minimize the thrust loss of rear rotors, but it would generate large bending moment in the supporting bars.

The flight performance results of the hypothetical model based on Volocopter 2X were mainly focused on the operation in no side wind condition. There is some

uncertainty over the scale of benefit that would actually be achieved in real flight with yaw flow. The effect of rotor-rotor interference under the operation in the yawed flow is needed to be an area for further study.

Appendix

Appendix-A. PID gain list

		Wingless type eVTOL for small UAV(Quadrotor)			Wingless type eVTOL for UAM service (tuned for Hexa-like)			Wingless type eVTOL for UAM service (tuned for FRRA)		
		P gain	I gain	D gain	P gain	I gain	D gain	P gain	I gain	D gain
Position	X_b	0.5	-	-	0.5	-	-	0.5	-	-
	Y_b	0.5	-	-	0.1	-	-	0.1	-	-
	Z	1	-	-	2	-	-	2	-	-
Velocity	U	1	0.1	1	0.5	0.001	0.1	0.5	0.001	0.1
	V	1	0.1	1	0.2	0.001	0.1	1	0	0.01
	$\dot{Z}$	1	-	-	5	-	-	5	-	-
Acceleration	$\ddot{Z}$	0.5	0.3	0.5	5	0.02	0.05	5	0.02	0.05
Angle	ϕ	1	-	-	1	-	-	1	-	-
	θ	1	-	-	1	-	-	1	-	-
	ψ	4	-	-	2	-	-	2	-	-
Angular velocity	P	1	0.02	0.05	1	0.02	0.05	1	0.02	0.05
	Q	1	0.02	0.05	1	0.02	0.05	1	0.02	0.05
	R	0.19	0.02	0	1	0.02	0.05	1	0.02	0.05

118

Appendix-B. Coefficients matrix of Hexa-like rotational direction

Table B.1. $\mathbf{C_{RSM}}$ matrix and E matrix of $\bar{\mathbf{C}}_\mathbf{T}$ in climb

E matrix	$\mathbf{C_{RSM}}$ matrix																					
0.9191	-0.4205	-1.0771	-0.9699	1.0628	-2.7660	5.2586	-1.1329	-2.5312	0.1505	0.4073	-0.5785	-0.2250	-0.0832	-0.3103	8.7391	-12.4263	4.2543	5.7802	-5.9064	7.9189	-2.1156	-3.6714
0.8829	0.7870	-2.8454	-1.6036	0.7987	-6.2479	13.7948	4.1027	-1.6922	0.1027	0.2900	-0.4711	-0.2803	-0.2792	-0.2025	12.1296	-24.7312	-5.7883	4.9322	-6.7343	13.3035	3.4596	-3.2828
0.9670	0.1735	-3.4544	-1.8623	0.8039	-3.7002	14.3431	6.9640	-0.2396	0.2069	0.1872	-0.4905	-0.2516	-0.3061	-0.5915	7.9908	-24.3431	-11.7844	1.8807	-4.5014	12.9678	6.8671	-1.4883
1.4088	-0.1093	-3.8519	-2.5029	1.0766	-5.6233	13.5793	3.5744	-2.8706	0.3964	0.7250	-0.7501	0.4582	-0.3497	-0.5210	12.9423	-22.7255	-4.6665	7.5518	-7.7217	12.3614	3.1644	-4.8264
0.7141	-0.0815	-2.0140	0.4325	1.5765	-0.5265	6.7165	-4.9316	-2.2933	0.3063	-0.2607	-0.4619	0.0631	-0.1352	-0.6483	2.4417	-11.8617	6.9669	3.2083	-1.7321	6.6497	-2.3528	-1.5284
0.7597	1.3857	-1.3084	-0.6029	0.8789	-7.9897	4.5692	-2.4056	-2.6464	0.2039	0.0131	-0.5481	0.0606	-0.0372	-0.2626	14.6165	-9.3445	3.9103	6.8269	-7.9835	5.7916	-1.0996	-4.4925
1.1586	-0.6322	-2.9454	-3.1154	0.6001	-3.8119	14.1888	5.4774	-2.0171	-0.0959	0.8223	-0.7376	-0.3992	-0.0699	-0.3773	12.1481	-24.9630	-4.4477	6.9236	-8.0884	13.7492	2.1100	-4.8837
0.9886	2.0732	-2.0820	-3.6681	0.8025	-13.5167	8.4612	7.5147	-4.2125	0.2225	0.5182	-0.9248	-0.2815	0.0041	-0.1617	24.5266	-15.0295	-7.4559	12.1183	-13.3027	8.6574	3.2154	-8.2891
0.6696	0.3229	-0.9194	-1.8111	0.9519	-5.2025	3.1745	3.1814	-2.1342	0.2464	0.2217	-0.6894	-0.7780	0.0710	-0.3616	11.8041	-7.2362	-1.2167	5.7601	-7.1352	5.2645	0.3171	-3.9605
0.5209	0.9677	-1.6512	0.4035	1.5864	-5.7860	6.0382	-6.0329	-3.6125	0.0571	-0.2084	-0.4692	0.6369	-0.2439	-0.2827	11.5237	-12.1729	9.3884	6.3112	-6.5609	7.3911	-3.4789	-3.4791
0.7910	1.4206	-1.8049	-0.4067	0.7077	-7.9547	3.4760	-3.1901	-1.4770	0.1507	0.0412	-0.6922	0.9579	-0.1858	0.0604	14.2091	-7.1392	4.6504	4.6785	-7.6014	5.0418	-1.3062	-3.3842
0.4423	1.3499	-1.5438	0.1360	1.1676	-7.2180	3.5195	-6.1312	-3.6713	0.4334	-0.1204	-0.5355	0.6146	-0.1181	0.2312	12.3614	-6.8352	12.5712	7.6130	-6.5289	4.3796	-6.5539	-4.6919
0.7308	1.0722	-2.7615	-2.4330	1.8130	-10.7887	11.5972	6.8471	-6.9424	0.3553	0.3949	-0.8097	-0.0203	-0.2927	-0.3522	21.7445	-21.0203	-7.9036	14.6823	-12.3755	11.8494	3.9196	-8.7596
0.4498	0.8519	-0.5972	-1.2780	1.1728	-6.2654	1.8677	-0.1322	-4.2376	0.2706	0.2253	-0.5774	0.1318	-0.0146	0.2383	12.1367	-6.0266	5.2208	8.7126	-6.8891	4.4891	-3.6411	-5.3169
0.6081	-0.7110	-1.3809	-1.6256	1.2514	0.2328	4.7851	3.5805	-3.2543	0.1758	0.1472	-0.4322	0.0249	-0.1930	0.0515	2.3112	-9.4110	-2.3539	5.5838	-1.9518	5.6537	0.8052	-3.0170
0.6310	0.5267	-1.2199	0.4272	1.0677	-4.7641	5.0910	-4.4309	-3.1007	0.0792	0.1356	-0.4508	0.2537	-0.2388	-0.1070	9.9983	-11.6733	6.6062	6.4636	-5.8376	7.3638	-2.3435	-3.8595
0.8136	-0.9412	-3.3756	0.2047	1.4248	2.4296	11.1703	-2.8597	-2.5972	0.4516	-0.1604	-0.4245	0.5903	-0.4452	-0.1306	-2.1847	-19.1880	5.0376	4.1060	0.6713	10.4523	-2.1180	-1.9815
0.9372	-0.0339	-3.8356	0.6379	0.5666	-0.8509	14.7389	-6.2145	0.1761	0.3058	-0.0615	-0.4257	0.6305	-0.3532	-0.0787	2.4051	-25.2079	9.5197	0.9363	-1.4667	13.3140	-3.9472	-0.8774

Min. and Max. value of C_T in climb

		Rotor 1	Rotor 2	Rotor 3	Rotor 4	Rotor 5	Rotor 6	Rotor 7	Rotor 7	Rotor 9	Rotor 10	Rotor 11	Rotor 12	Rotor 13	Rotor 14	Rotor 15	Rotor 16	Rotor 17	Rotor 18
Min.		0.004361	0.004317	0.004318	0.004321	0.004316	0.004314	0.004317	0.004317	0.00431	0.004319	0.004317	0.004312	0.004314	0.004314	0.00432	0.004356	0.004314	0.004311
Max.		0.011316	0.011581	0.012211	0.010682	0.011823	0.011385	0.009771	0.010566	0.009746	0.010606	0.010167	0.011597	0.011057	0.011544	0.011887	0.011774	0.012117	0.011757

Table B.2. $\mathbf{C_{RSM}}$ matrix and E matrix of $\bar{\mathbf{C}}_\mathbf{P}$ in climb

E matrix	CRSM matrix																					
1.6527	-3.9781	-2.8165	0.3369	-2.5229	21.0849	2.8153	-2.8324	9.7639	0.7940	-1.4783	1.3980	0.6995	0.4456	0.7331	-39.6687	-0.8043	4.0399	-21.2157	22.7851	-0.4038	-1.7197	12.6823
1.4524	-2.9968	0.2684	0.7379	-2.2465	13.5130	-9.0673	-2.8921	6.1560	0.0880	-0.2890	0.5014	0.0450	0.8008	0.5633	-23.4313	18.2497	3.1668	-11.8274	12.7723	-10.0421	-1.1493	6.5217
1.4685	-3.6033	-0.8194	2.9661	-2.2925	16.8327	-4.1503	-13.3820	5.2200	0.2626	-0.5992	0.7046	0.2487	1.1049	1.0367	-28.8183	10.2569	19.1541	-10.7877	15.4960	-6.1419	-8.9536	6.1819
1.4425	-1.3290	-2.6465	-1.1243	-1.9819	1.5112	11.5251	7.1788	5.0247	0.2804	0.5362	0.6942	-1.0652	1.1161	0.5452	-2.0083	-19.3207	-14.6045	-10.3179	1.1898	10.1323	8.8997	5.8938
1.8093	-3.8346	-1.1105	-1.4713	-1.6387	12.4375	-1.9512	3.2975	0.0589	0.0630	0.4422	0.2451	-0.1861	0.7162	1.3571	-17.7703	7.3614	-4.2973	0.0786	8.5309	-4.7429	1.9318	-0.1213
1.3360	-0.3211	-0.1448	-2.6731	-0.5719	-0.0718	-4.2067	9.4876	0.9638	0.1006	0.4633	0.1253	-0.3838	-0.0689	1.5323	-1.9619	9.5256	-14.7255	-4.3132	1.9346	-5.4216	7.3489	2.9078
2.0371	-1.7118	-6.0016	0.0980	-5.6189	5.1758	20.0631	0.4094	20.5719	0.4831	0.1256	0.2022	0.4795	-0.2877	0.5011	-8.9458	-30.1296	-6.4058	-30.1483	5.3141	15.2515	5.6212	14.6084
1.6835	-2.2861	-2.5511	0.1648	-1.3677	9.9413	1.9779	-4.4337	4.9400	-0.0042	-0.2449	0.3808	0.4944	-0.3597	1.4323	-17.7445	2.5236	6.3871	-10.6052	10.0776	-2.7427	-2.9190	6.2716
1.7520	-3.1845	-0.7891	0.5563	-4.9740	16.3596	-4.5430	-5.3302	21.7099	0.2561	-0.1717	0.7422	0.5107	-0.7554	1.0310	-30.6854	11.0074	6.8978	-35.7495	17.4438	-6.4964	-2.9072	18.5261
1.4489	1.0123	-5.4866	-0.5992	0.4660	-6.8988	21.0144	-1.3747	-1.1580	0.5429	0.6182	0.0794	0.2263	0.4913	-0.4995	9.0774	-33.1938	3.7965	0.4284	-3.7145	16.8024	-2.2455	0.0650
0.9436	0.7273	0.0980	0.0739	-0.4709	-1.6059	-2.2229	-1.0974	5.1850	0.0366	0.0477	0.6028	-0.3273	-0.3389	0.1814	-1.7532	4.5122	1.1466	-11.7830	2.4836	-2.6236	-0.3044	6.9149
0.9323	-0.1508	-0.8402	-0.1782	-0.4495	1.2528	0.5634	3.1217	6.2040	-0.2217	-0.0311	0.4878	-0.4399	-0.7231	-4.9015	2.2394	-6.3789	-13.1862	3.8319	-2.0895	3.7787	7.6083	
1.1178	-1.7656	-3.8056	4.6540	0.2927	5.4809	12.8955	-19.1973	-0.6998	0.6131	-0.3977	0.4703	1.1982	0.6328	-1.0404	-8.9116	-22.3629	26.9360	-0.7217	4.9204	12.0509	-12.3168	0.8952
1.1379	-1.0116	-1.4074	-0.1395	-0.8457	5.1613	0.7075	2.1407	6.6280	0.0895	-0.3144	0.2599	0.2492	-0.0205	-0.9165	-10.4205	1.9122	-4.4351	-11.9859	6.3519	-1.7183	2.5526	6.4046
1.3863	-0.8411	-1.4366	-0.4494	-1.5449	2.9229	0.2396	1.5599	4.4937	0.0197	-0.1877	0.4776	0.1868	0.8372	-0.5318	-5.9365	2.9785	-2.7929	-7.5006	3.7394	-2.4201	1.5459	3.7221
1.6053	-0.8121	-2.2290	-2.0718	-1.6653	-0.7451	8.5242	7.6823	3.2095	0.2961	0.5190	1.0391	-0.2271	0.6777	-0.0991	-0.2247	-13.5389	-12.2147	-6.0527	1.0267	6.8583	6.4166	3.4260
1.1706	-0.8280	1.2793	-1.0783	-1.6529	2.1622	-7.5328	6.0288	3.7997	-0.2417	0.2639	0.7322	-0.6384	0.9933	-0.2432	-4.4686	13.1989	-10.2384	-7.3038	2.7461	-7.0050	5.3816	3.9287
1.3990	-1.4303	-0.6912	-0.7630	-1.8582	5.9054	-2.1406	4.8275	5.6756	-0.0401	-0.0421	0.5617	-0.2182	0.8468	-0.1089	-11.4528	6.6318	-9.4235	-10.5168	6.8156	-4.2323	5.4069	5.5953

Min. and Max. value of C_P in climb

	Rotor 1	Rotor 2	Rotor 3	Rotor 4	Rotor 5	Rotor 6	Rotor 7	Rotor 7	Rotor 9	Rotor 10	Rotor 11	Rotor 12	Rotor 13	Rotor 14	Rotor 15	Rotor 16	Rotor 17	Rotor 18
Min.	0.000393	0.000322	0.000295	0.000368	0.000316	0.000358	0.000394	0.000374	0.000384	0.000364	0.000355	0.000333	0.000373	0.000286	0.00031	0.000351	0.00029	0.000286
Max.	0.000518	0.000526	0.000525	0.000514	0.000524	0.000526	0.000515	0.000515	0.000509	0.000517	0.000513	0.000515	0.000515	0.000525	0.000524	0.000518	0.000526	0.000527

Min. and Max. value in sampling points of rotational speed and airspeed

	RPM	U_a	V_a	W_a
Min.	823	-30	-18.97	-4.82
Max.	1,700	8.97	-18.97	0

120

Table B.3. C_{RSM} matrix and E matrix of $\bar{c}_T$ in descent

E matrix	C_{RSM} matrix																					
1.379831	2.663975	2.295927	-3.31896	-2.70174	-5.80753	-14.6243	11.74574	8.137791	-0.40714	-0.24126	0.321511	-0.68247	0.407803	0.831144	3.598233	20.74172	-18.0096	-11.5085	-0.11872	-8.72432	9.413403	5.104847
1.314693	1.103831	-5.61715	3.763535	-3.13194	-3.28344	24.40483	-16.8014	11.67905	-0.4114	0.084728	0.359831	-1.31807	0.673353	0.062039	2.771661	-37.4365	24.62427	-17.7203	-0.61385	18.26162	-11.1486	8.578385
0.236899	1.135228	4.438151	2.816274	2.828987	-12.3241	-16.3608	-18.6864	3.103696	1.229483	1.490565	-0.08764	-0.81258	-1.28226	-1.70783	15.85512	20.81652	31.89827	-7.79927	-6.35726	-8.53768	-16.2543	4.344732
0.163572	0.699739	3.883998	2.985073	7.380553	-17.3502	-9.10384	-23.8843	-14.5928	2.052728	2.498523	-1.31641	-0.27243	-2.0751	-3.42536	26.09571	5.056508	39.35636	22.33895	-11.6198	1.165165	-18.6476	-10.6833
0.847839	1.670647	3.524265	-3.06991	0.775885	-4.77201	-18.5749	17.43979	-0.55042	-0.4269	-0.27632	0.736442	-0.87588	0.393186	0.559421	4.929025	27.62766	-31.7674	-3.32712	-1.81501	-12.587	17.23904	2.594329
0.588225	0.571743	5.80344	-1.19885	2.52588	-7.30068	-17.3118	8.227251	-9.01842	1.237871	0.415583	-0.82713	-0.26347	-1.09061	-0.99091	10.4687	17.3534	-20.6478	17.2577	-4.40903	-5.04286	13.29922	-9.07141
1.00458	1.969587	-0.87802	-0.45995	-1.58194	-4.96166	2.045558	-2.08014	4.949229	-0.44942	-0.06815	0.136689	-1.83528	0.538837	0.201126	4.173879	-2.62734	5.419333	-7.3332	-0.86591	2.159048	-2.34479	3.448699
1.325451	4.472863	1.280415	-5.45213	-6.2256	-2.9246	-11.3997	29.44213	10.95698	-2.16167	-1.74862	0.16972	-1.83304	1.839342	2.168754	-0.51905	20.90691	-50.4388	-13.4123	1.602353	-10.1327	26.74564	5.730538
0.802947	5.15332	6.501233	-9.66732	-5.03809	-3.9789	-35.0188	45.70357	9.186676	-2.10535	-1.68889	0.392651	-1.93601	1.372633	2.636706	-1.407	56.23619	-70.2862	-12.067	2.752611	-26.6086	34.60814	5.076497
-0.05658	1.707226	4.498013	1.890552	6.550257	-20.9247	-10.3454	-18.7662	-9.2452	2.210105	2.343738	-1.36312	0.49307	-2.60404	-3.35241	30.37617	4.963095	31.33903	14.84348	-13.2775	1.820149	-14.7583	-7.40132
0.927515	2.203323	3.697681	-6.62461	1.76558	-8.78197	-22.5357	22.82756	-4.65137	-0.31584	0.462596	0.271047	0.470664	-0.62744	-0.1182	10.27465	34.45486	-32.8249	7.309099	-3.85334	-15.1987	16.01572	-3.96199
0.529083	1.243504	5.13621	-0.7586	7.910395	-20.9427	-17.2387	-9.7579	-23.0548	2.612476	1.919697	-2.04565	2.020479	-2.1902	-2.53295	33.3931	14.37847	17.18582	37.99746	-15.4707	-2.10232	-7.48482	-18.7894
1.323689	3.036896	-2.75854	-3.48957	-6.17739	2.687886	4.746457	19.79569	12.38331	-1.95068	-2.01738	1.147386	-1.79829	1.383596	2.660383	-9.78966	-2.01384	-33.6941	-16.997	6.018084	0.198584	18.40435	7.474156
0.267658	1.911669	-0.96328	5.530398	2.105728	-14.7576	6.25368	-35.0901	-0.98098	1.416682	1.412242	-0.95593	-0.21538	-1.21731	-1.85546	20.41214	-12.4919	59.25102	3.192663	-8.72175	7.798854	-29.2175	-1.82872
-0.49873	1.953139	-1.07333	6.261199	4.359769	-15.2585	5.962373	-38.9935	-1.71446	1.051434	1.789705	-0.51558	-1.20408	-1.52587	-2.59185	20.99723	-7.73486	68.69189	0.422328	-9.05519	3.804821	-34.863	0.235292
-0.51429	0.045264	2.842443	6.462416	8.140879	-17.3228	-2.11695	-39.6501	-10.1648	2.672505	2.644632	-0.96978	-0.36545	-2.89431	-4.3165	26.29701	-6.50992	66.26533	14.08167	-11.9203	7.069797	-32.6931	-6.53202
-1.08126	-0.11089	3.126492	8.692162	9.769972	-17.9986	0.193186	-51.2193	-13.1758	3.217335	2.880659	-1.14527	-0.14626	-3.46899	-4.30112	26.91264	-11.5041	86.59955	18.25409	-12.0473	9.282908	-43.5148	-8.75527
0.178431	-1.39496	-3.39298	8.75397	7.932008	-15.6813	28.07893	-51.8767	-12.6747	2.740111	2.850158	-0.90867	0.177123	-2.51175	-4.29304	26.8775	-53.8422	85.55282	18.50469	-13.0796	29.46996	-42.3352	-8.63435

Min. and Max. value of C_T in descent

	Rotor 1	Rotor 2	Rotor 3	Rotor 4	Rotor 5	Rotor 6	Rotor 7	Rotor 7	Rotor 9	Rotor 10	Rotor 11	Rotor 12	Rotor 13	Rotor 14	Rotor 15	Rotor 16	Rotor 17	Rotor 18
Min.	0.004574	0.004458	0.004284	0.004585	0.003883	0.004571	0.004478	0.004795	0.004111	0.004366	0.003591	0.004396	0.004346	0.004017	0.004412	0.004534	0.004238	0.004453
Max.	0.01249	0.013179	0.013455	0.011938	0.012965	0.012598	0.012137	0.012616	0.012536	0.011421	0.011969	0.011464	0.011329	0.012163	0.013074	0.012125	0.013125	0.013222

Table B.4. C_{RSM} matrix and E matrix of $\bar{C}_P$ in descent

E matrix	C_{RSM} matrix																					
1.7922	-4.7513	-2.4397	0.3269	-3.9528	26.5276	-2.1284	-3.8586	17.6640	0.9157	-2.0995	1.7435	0.8065	0.4043	1.1086	-50.5269	9.4705	6.6283	-35.4731	29.2794	-6.3354	-3.4165	20.0904
1.6945	-1.5745	-2.3463	-1.2516	-1.8518	1.3721	6.1682	4.6394	4.3267	0.4850	0.0910	0.1221	0.2832	0.5621	0.1624	-0.1761	-10.4163	-8.4101	-7.4528	-0.1335	5.9880	4.9315	3.9027
1.5921	-2.3223	-2.6108	1.6201	-1.5837	6.9581	6.4624	-7.9237	0.9478	0.5392	-0.1284	0.2730	0.3935	1.1251	0.7453	-10.4954	-10.1200	10.2763	-2.3717	5.4206	5.3659	-4.1834	1.5155
1.5010	1.5080	-2.6607	-3.7328	-3.6022	-13.2988	13.4527	17.0521	15.1141	0.5626	0.5587	0.4436	-0.9126	0.8885	0.6796	22.3788	-24.4358	-28.7014	-27.4965	-11.1695	13.3092	15.4635	14.8525
1.9207	-2.0349	-3.1407	-3.4615	-0.7062	-0.4293	11.0730	11.2683	-3.9051	0.3300	0.9617	-0.2478	-0.0452	0.5192	0.8651	6.0676	-17.6203	-16.6086	7.6725	-4.5712	9.3293	8.3165	-4.1407
1.6152	-0.5929	-1.9600	-3.3494	-0.8775	-1.5459	4.2193	10.9603	3.0616	0.3367	0.3038	0.2002	-0.1922	-0.2474	1.3877	2.1819	-4.9951	-16.3506	-7.9806	-0.5239	2.3979	8.2210	4.8446
2.3523	-0.2485	-6.7207	-2.5285	-7.6764	-4.0419	23.3152	9.8712	31.5744	0.7356	0.1314	-0.0193	0.6373	-0.4430	0.5762	6.7718	-36.4158	-20.0040	-48.5717	-2.5830	18.9213	12.1449	24.2842
1.9728	-5.1949	-3.1464	1.6388	-2.1956	24.0818	0.8899	-11.8597	8.7547	0.0024	-0.9083	0.9294	0.5773	-0.3892	1.5997	-40.9793	7.1546	18.4429	-17.7657	22.2793	-5.8748	-8.9448	10.0203
1.9997	-3.8125	-1.7391	0.2080	-5.7585	17.5443	-0.7576	-4.9635	25.2934	0.4149	-0.3783	0.8372	0.6418	-0.8640	1.0244	-31.4569	4.7671	6.8540	-41.0539	17.6625	-3.1770	-2.8901	20.8781
1.5113	-0.5212	-4.6887	0.7730	-1.1585	2.4920	14.4816	-7.7048	7.1987	0.5669	-0.0645	0.6184	0.2831	0.4135	-0.0197	-7.6690	-19.9948	14.0431	-14.5238	5.4467	9.1681	-7.6129	7.8385
1.1556	1.7843	-1.7318	-1.5146	-0.6167	-10.1392	8.0388	4.4632	6.4265	0.3174	0.1664	0.4088	-0.1368	-0.5263	-0.0260	14.3504	-14.4909	-6.8996	-13.2841	-6.3027	7.9252	3.7699	7.5168
1.2067	-1.4899	-1.5297	0.0612	-1.7293	6.9011	1.6293	0.7323	12.6152	-0.1039	-0.5138	0.8259	-0.3067	-0.3018	-0.5150	-13.7453	1.7856	-1.9077	-24.3609	8.5012	-2.1632	1.4406	13.3718
1.1650	0.1539	-4.0548	3.1302	-0.6179	-5.3500	14.5228	-13.0015	4.9580	0.7854	-0.0630	0.0447	1.4429	0.7868	-1.3287	8.8966	-27.0048	17.3004	-10.4998	-4.0529	15.1302	-7.5490	6.3387
1.2870	-2.3580	-1.6946	0.5845	-1.5626	11.6880	0.2069	-1.6196	9.9881	0.1449	-0.7174	0.5745	0.3241	-0.0865	-0.7204	-21.1399	4.0695	1.7451	-17.8553	12.0040	-3.2030	-0.5788	9.3495
1.4812	0.3818	-2.9960	-1.6051	-1.3775	-5.9150	9.9565	5.8898	4.2290	0.3158	-0.0299	0.2762	0.3663	0.5888	-0.6996	10.4978	-15.4696	-9.3330	-6.3096	-5.2798	7.8648	4.9221	2.8534
1.6976	0.1733	-2.1690	-3.1373	-3.2801	-6.3226	8.8948	11.4151	12.2076	0.5037	0.3866	0.9935	-0.1046	0.4896	0.0876	9.2512	-14.9909	-17.3728	-21.0837	-3.8117	7.8229	8.7398	11.1169
1.3144	2.5747	-1.4392	-4.3668	-1.0962	-20.2426	10.8516	19.0834	2.1311	0.2296	0.9406	0.0349	-0.3800	0.6436	-0.7513	36.1119	-22.6402	-30.1791	-2.9257	-19.2808	13.2636	15.5405	1.3444
1.5448	0.1778	-2.6006	-2.3999	-1.8915	-5.6729	9.7578	10.9182	6.5363	0.3221	0.1618	0.3028	0.0055	0.5530	-0.3244	10.0338	-16.0232	-18.5622	-10.9732	-4.9425	8.4272	10.0846	5.5005

Min. and Max. value of C_P in descent

	Rotor 1	Rotor 2	Rotor 3	Rotor 4	Rotor 5	Rotor 6	Rotor 7	Rotor 7	Rotor 9	Rotor 10	Rotor 11	Rotor 12	Rotor 13	Rotor 14	Rotor 15	Rotor 16	Rotor 17	Rotor 18
Min.	0.0002197	0.0002287	0.0002099	0.0002973	0.0002201	0.0002289	0.0002726	0.0002298	0.0002247	0.0002919	0.0002097	0.0002645	0.0002824	0.0002457	0.0002152	0.0002585	0.0002302	0.0002359
Max.	0.0004603	0.0004476	0.0004492	0.0004634	0.0004534	0.0004365	0.0004634	0.0004551	0.0004690	0.0004643	0.0004510	0.0004578	0.0004536	0.0004708	0.0004646	0.0004560	0.0004505	0.0004429

Min. and Max. value in sampling points of rotational speed and airspeed

	RPM	U_a	V_a	W_a
Min.	800	-24.87	-20	0.705
Max.	1,800	9.09	10	2

Appendix-C. Coefficients matrix of FRRA rotational direction

Table C.1. C_{RSM} matrix and E matrix of $\bar{C}_T$ in climb

E matrix	C_{RSM} matrix																					
0.7748	-0.2268	-0.7770	-1.7990	3.9561	-0.5639	0.7491	0.2824	-13.1986	0.4991	-0.5885	-0.1598	0.4917	-0.4522	-0.0132	2.7831	-4.7140	4.8554	18.8358	-2.0351	4.0734	-3.5732	-8.7724
0.9452	0.1324	-3.1420	-2.6613	1.1074	-2.2563	12.7045	8.5852	-1.7338	0.3320	-0.1671	-0.3021	-0.0940	-0.3495	-0.2606	5.0839	-22.7573	-11.8258	3.4714	-2.8688	12.4629	6.1071	-1.9654
0.6595	0.0161	-2.2345	-1.6286	1.5244	-2.0740	10.3871	7.1963	-1.8384	0.2821	-0.0148	-0.4072	-0.6867	-0.4553	-0.5631	4.9067	-19.2013	-11.7811	2.9791	-2.8089	10.7946	6.7594	-1.5524
1.1345	-1.6170	-3.0086	-1.6330	3.5105	5.9192	5.6320	-1.2623	-11.4873	0.8888	-1.1598	-0.2868	1.1216	-0.7283	0.1438	-7.6602	-9.6097	7.3762	16.5540	3.4952	5.9517	-4.8519	-7.6085
0.7817	-0.6736	-3.3931	0.3940	1.8134	5.1991	9.1978	-4.8533	-1.6550	0.6787	-1.1212	-0.1908	0.4127	-0.3246	-0.4503	-9.1209	-14.2788	8.3421	-0.0980	5.0368	7.5628	-3.8106	1.0101
1.3110	-1.7060	-3.7402	-2.0930	0.9523	6.4835	8.8403	1.4759	-2.8130	0.5579	-0.6379	-0.2020	0.2474	-0.2855	-0.2194	-8.6621	-11.8820	1.3651	5.5137	3.9737	6.1245	-1.0414	-3.0010
0.9213	-0.5812	-1.8094	-3.8402	3.1527	-0.9593	7.1027	9.0597	-10.3331	0.3924	-0.1790	-0.3499	-0.1933	-0.5091	-0.1314	5.0972	-14.7719	-7.5829	16.1127	-3.7096	9.4098	2.4810	-8.0445
0.7971	1.6550	-0.8973	-5.1489	2.3698	-9.8901	2.5685	13.6212	-9.9625	0.6212	-0.0953	-0.6616	-0.3454	-0.2578	0.1102	17.6828	-6.7978	-14.5993	18.8094	-9.5732	5.1792	5.9039	-10.6837
1.0239	-0.7010	-2.2020	-5.0302	0.3420	-3.1991	6.4634	20.0028	-1.3836	0.3333	0.5689	-0.7016	-1.1012	-0.0397	-0.2953	9.9322	-10.5031	-28.8792	5.4730	-6.5075	6.6000	14.5285	-3.9371
0.8337	-1.4785	-1.9879	-1.6413	2.0435	8.5557	1.5944	1.0802	-3.8814	0.6941	-1.5231	-0.0440	1.1761	-0.6371	0.2407	-13.3452	-4.1173	3.0988	2.9272	6.7730	3.6100	-2.3709	-0.2268
0.9072	-1.3020	-3.3626	0.4524	3.6133	5.3051	2.8903	-9.3361	-12.0875	0.8869	-1.0962	-0.3754	1.7734	-0.3009	0.0357	-7.0842	-3.8428	18.2736	17.4931	3.2293	3.1476	-9.7837	-8.1872
0.3783	0.1011	-0.7389	-1.2107	2.7664	2.0888	-3.9250	-3.3018	-9.2566	0.9364	-1.4688	-0.0726	1.2258	-0.4706	0.6633	-4.2894	5.0090	13.7475	12.8802	2.4603	-1.1370	-9.3816	-5.8633
0.7606	-0.0792	-1.8284	-4.7025	2.2019	-3.9108	5.7448	16.3020	-7.2214	0.5618	-0.0017	-0.4129	-0.2104	-0.4945	-0.1175	9.3880	-10.8955	-20.3118	11.8797	-5.6866	6.6613	9.1608	-6.0811
0.5040	-0.5539	-0.9934	-2.1537	2.8028	3.1207	-1.3036	2.1517	-10.4344	0.5992	-0.9734	0.0027	0.6251	-0.3184	0.8008	-4.8552	1.5159	4.7919	14.3614	2.4892	0.2065	-4.7368	-6.4788
0.5875	-1.3711	-1.2664	-2.7835	2.6056	3.5377	2.7059	8.9628	-8.7774	0.3496	-0.1450	-0.2671	0.0815	-0.6383	0.2893	-3.1945	-5.5141	-9.3583	13.0022	0.9052	3.7319	3.5873	-6.1063
0.7696	-0.9833	-1.8540	-1.9228	0.8673	3.1958	4.8040	5.1513	-1.7948	0.4044	-0.4143	-0.4317	0.2054	-0.4878	-0.0554	-3.0455	-9.2186	-4.7588	3.8381	0.9393	5.6903	1.9365	-2.2110
0.6775	-1.3648	-2.3640	0.1293	2.7652	6.1968	5.4671	-3.9898	-6.1818	0.6410	-0.6686	-0.2833	0.9877	-0.6632	-0.1281	-9.1386	-10.9140	8.6346	7.4284	4.4605	6.6879	-4.6121	-2.8080
0.7036	-1.0504	-2.2115	0.1072	2.8096	5.1460	5.6219	-5.0054	-7.9395	0.6212	-0.7923	-0.2624	0.7850	-0.6863	0.2198	-7.4367	-11.4892	11.1547	10.8168	3.5458	7.0154	-6.1841	-4.6909

Min. and Max. value of C_P in climb

	Rotor 1	Rotor 2	Rotor 3	Rotor 4	Rotor 5	Rotor 6	Rotor 7	Rotor 7	Rotor 9	Rotor 10	Rotor 11	Rotor 12	Rotor 13	Rotor 14	Rotor 15	Rotor 16	Rotor 17	Rotor 18
Min.	0.00480742	0.00506365	0.00489038	0.00452606	0.00463314	0.00512652	0.00454450	0.00491536	0.00473941	0.00455343	0.00512612	0.00489837	0.00473797	0.00476182	0.00471495	0.00461455	0.00479173	0.00503121
Max.	0.01145427	0.01179157	0.01200062	0.01112972	0.01200453	0.01069101	0.00950552	0.01027615	0.01008996	0.01021998	0.01055785	0.01154683	0.01176866	0.01151285	0.01194157	0.01203053	0.01202408	0.01184347

Table C.2. C_{RSM} matrix and E matrix of $\bar{C}_P$ in climb

E matrix	C_{RSM} matrix																					
1.8573	-1.4475	-4.8016	-0.7739	-2.8554	0.0892	19.9154	5.7187	7.2539	-0.0962	1.2650	0.2393	-0.4668	1.2050	-0.3843	0.5438	-31.3930	-15.5486	-9.6489	0.1577	15.8533	10.8388	3.9509
1.4728	-2.6716	-0.3512	1.2381	-1.1896	11.3720	-5.5312	-5.8390	1.1813	0.1477	-0.2147	0.5336	0.3124	0.8822	0.2965	-19.3057	12.5040	7.5108	-3.7308	10.3329	-7.2906	-3.1731	2.4187
1.4323	-3.7340	-0.1348	2.0955	-1.5390	18.2088	-8.2667	-10.9082	2.3528	0.4515	-0.9269	0.7768	0.3433	0.8899	1.1750	-31.4060	16.7120	17.6819	-6.9719	16.9090	-9.2284	-9.1976	4.5709
0.7438	-1.0809	0.4192	0.0456	0.2671	0.8252	1.6537	2.7050	-3.5630	-0.2988	-0.0970	0.8937	-1.0371	0.9028	0.2604	0.9744	-5.6882	-7.1411	1.7206	-0.8805	3.9457	5.2872	0.4158
1.4006	-2.5377	1.2812	-0.2977	-1.5311	10.0889	-10.3728	-0.0495	0.2522	0.0442	-0.1677	0.6654	-0.3807	0.7737	1.7605	-16.5534	18.5219	0.0472	-2.1421	8.7269	-9.7949	0.0535	1.5123
0.9009	0.7470	1.6993	-0.1229	-0.9365	-7.2955	-6.0004	1.3696	-0.1382	-0.5827	1.4304	-0.3574	-0.9032	0.5424	0.9192	12.3887	9.6355	-6.5274	1.7983	-6.4009	-5.0447	5.1870	-1.9601
2.0977	-1.3018	-6.5207	-0.6875	-3.0845	-2.0179	24.1625	4.4110	8.3487	0.0315	0.8998	-0.3062	0.2761	0.3826	-0.0613	7.4968	-37.4130	-13.3466	-8.7606	-4.6838	18.9004	9.5245	2.8401
1.3306	-0.1038	-1.3469	1.1758	-2.4221	-3.8834	6.2805	-5.1888	6.5976	-0.5140	1.4658	-0.2670	-0.1195	0.1591	0.8158	7.9444	-9.6467	1.9705	-7.9338	-4.5573	4.6202	1.5676	2.9234
1.3804	-3.7887	1.6566	1.1664	-3.0398	22.5547	-15.2111	-8.8739	12.3557	0.2765	-1.6690	1.0182	0.9392	-0.8996	1.7603	-40.1681	25.9825	16.3004	-23.1049	21.9922	-13.1359	-9.3529	13.1311
1.6864	2.0497	-6.1083	-0.7249	-1.3155	-16.1084	26.2286	0.1681	3.9031	0.3329	1.3983	-0.2641	-0.2934	0.7894	-0.5379	26.8313	-43.0601	-1.0258	-4.0649	-13.6475	22.2439	1.2532	0.9735
0.8760	1.7109	-0.9788	1.6080	-0.6685	-12.2682	8.8635	-5.7640	2.5356	-0.4228	1.5067	0.0988	-1.2042	0.5956	-0.3436	20.0140	-15.0551	4.7787	-3.9779	-10.3089	7.2699	-0.4663	1.5509
0.7560	1.9531	1.2464	-0.5924	-0.3281	-12.8110	0.3666	6.2712	1.8218	-0.7682	0.1216	-0.7865	-0.0343	-1.1279	21.6452	-2.8908	-15.2086	-1.6386	-11.4026	1.8977	9.7892	0.2585	
1.7433	-5.0544	-1.8486	3.0647	-2.4572	19.1008	4.2569	-16.4518	8.4124	-0.0475	0.3002	0.6096	0.9770	1.6143	-1.1812	-27.8839	-8.4486	24.5300	-14.8802	13.4383	4.8802	-11.3274	8.0218
1.0991	-0.3257	-0.7675	1.3701	-1.7781	1.1411	2.1669	-3.8553	10.0926	-0.4000	0.6025	-0.0098	-0.1491	0.4279	-1.2638	-3.3449	-1.6273	1.7328	-15.7898	2.4235	0.0077	0.8957	7.4754
1.1698	-0.7513	1.3206	0.9231	-0.9739	2.6275	-9.2205	-5.6636	2.8459	-0.1481	0.1150	0.4002	0.0602	0.8059	-0.7884	-5.2927	15.4814	9.1156	-4.5981	3.1603	-7.9958	-4.5571	1.9900
1.3187	0.2762	-0.7963	-0.4683	-1.4604	-3.5348	3.7598	2.0234	4.5473	0.2247	0.4738	0.6429	0.1554	0.6306	-0.5274	4.2555	-8.4990	-5.0631	-8.2445	-1.4895	5.0911	3.3922	4.4858
1.1993	-0.8996	0.7054	-1.2636	-0.6737	1.1550	-5.1401	7.0519	-0.7756	-0.1817	0.4991	0.5745	-0.6634	0.9503	-0.2665	-2.0545	9.7393	-12.3588	0.2774	1.2156	-5.4179	6.6817	0.0197
1.4135	-1.7642	1.8247	-3.3072	-0.4960	0.8746	-8.1106	15.7063	-4.5798	-0.5190	1.5160	0.1019	-1.0699	0.7618	-0.1763	1.9047	14.6544	-26.2710	9.1052	-2.0683	-7.9075	13.9234	-5.3081

Min. and Max. value of C_P in climb

	Rotor 1	Rotor 2	Rotor 3	Rotor 4	Rotor 5	Rotor 6	Rotor 7	Rotor 7	Rotor 9	Rotor 10	Rotor 11	Rotor 12	Rotor 13	Rotor 14	Rotor 15	Rotor 16	Rotor 17	Rotor 18
Min.	0.00038207	0.00029449	0.00030475	0.00036510	0.00033120	0.00034479	0.00037956	0.00035001	0.00037766	0.00037970	0.00037880	0.00031919	0.00036584	0.00026834	0.00032719	0.00031821	0.00030302	0.00029380
Max.	0.00050125	0.00051149	0.00053199	0.00052643	0.00050614	0.00052897	0.00051520	0.00050982	0.00048852	0.00052128	0.00049878	0.00049566	0.00049837	0.00050525	0.00050720	0.00050072	0.00053276	0.00051042

Min. and Max. value in sampling points of rotational speed and airspeed

	RPM	U_a	V_a	W_a
Min.	823	-30	-18.97	-4.82
Max.	1,700	8.97	18.97	0

Table C.3. C_{RSM} matrix and E matrix of $\bar{C}_T$ in descent

E matrix	C_{RSM} matrix																					
0.847	4.016	-14.357	12.110	-3.424	-35.916	58.136	-68.559	36.483	2.082	2.819	1.828	-2.305	-0.888	-3.731	50.615	-80.462	115.179	-58.380	-23.052	37.186	-57.894	28.143
1.098	4.020	-16.972	13.574	-4.738	-46.978	69.275	-74.684	48.889	3.050	3.328	2.984	-2.900	-0.727	-4.552	69.458	-97.133	126.970	-80.485	-32.746	44.746	-64.747	39.499
1.258	4.013	-11.532	14.900	-4.280	-40.995	37.914	-83.600	50.795	0.781	3.325	3.753	-1.496	0.557	-5.589	61.358	-48.570	140.999	-88.165	-29.431	21.354	-72.035	44.475
-2.562	9.887	-17.268	7.236	-2.431	-70.300	89.381	-40.804	56.501	4.417	3.477	2.875	-8.340	-4.020	-6.219	95.675	-123.170	84.228	-88.896	-42.236	56.468	-45.752	41.621
-1.875	10.161	-16.604	7.664	-4.519	-74.268	78.355	-42.745	68.451	4.242	3.631	3.755	-7.919	-2.721	-5.848	102.745	-104.083	87.813	-112.850	-46.206	46.364	-48.658	54.757
0.390	2.945	-0.381	4.088	0.951	-28.174	6.013	-22.840	10.323	1.986	1.968	0.507	-1.772	-1.049	-2.855	41.111	-11.648	35.039	-15.810	-18.901	7.217	-15.967	7.343
1.239	4.078	-14.762	11.427	-4.628	-33.623	55.498	-64.476	36.454	1.111	2.520	1.986	-3.323	0.109	-3.070	48.082	-73.527	109.476	-58.929	-22.164	33.671	-55.220	28.740
1.666	2.275	-2.844	5.299	-2.981	-12.526	8.208	-32.367	9.904	0.043	1.184	-0.234	-0.478	0.770	-1.104	17.317	-11.625	49.383	-11.766	-7.701	6.414	-23.006	5.056
5.557	-7.614	7.455	13.391	3.288	38.332	-60.130	-78.080	-39.570	-4.797	0.710	-0.814	8.127	5.083	-0.350	-45.142	82.360	104.210	58.678	17.572	-35.356	-45.313	-25.996
-3.161	14.517	-26.585	6.418	-8.194	-98.119	125.325	-38.528	93.144	5.747	4.047	4.280	-10.780	-4.490	-7.208	134.107	-167.869	91.895	-146.773	-59.550	75.440	-53.186	69.429
-1.556	5.444	-10.570	6.959	0.125	-38.298	53.104	-36.913	23.796	2.599	1.828	1.064	-4.444	-2.802	-4.022	52.138	-73.163	69.015	-34.348	-22.819	34.365	-35.924	14.923
1.577	3.889	-8.742	2.511	-1.274	-38.770	33.245	-25.658	14.604	2.858	2.613	0.430	0.278	-1.190	-2.352	57.429	-49.315	44.798	-18.755	-26.539	24.639	-21.885	7.752
1.250	3.046	-13.444	11.483	-3.791	-27.628	50.703	-64.428	30.381	1.229	1.977	1.754	-2.388	-0.011	-2.597	39.850	-67.872	107.341	-49.492	-18.497	30.913	-53.376	24.350
0.131	5.241	-13.266	7.550	-2.814	-32.650	55.010	-48.972	29.444	1.358	1.653	1.138	-2.509	-1.177	-2.982	44.745	-74.341	89.809	-45.498	-19.915	34.035	-46.643	21.535
-2.520	11.270	-20.896	7.611	-5.340	-62.442	93.777	-42.248	59.831	2.372	2.306	2.446	-8.497	-2.455	-4.485	82.873	-120.425	91.309	-94.320	-36.042	52.020	-51.054	44.486
-0.863	5.932	-9.198	4.771	-1.610	-44.824	46.411	-28.268	34.809	2.919	1.991	1.911	-4.209	-2.108	-4.176	62.424	-66.870	56.350	-55.229	-27.987	31.990	-30.029	26.126
-2.573	8.901	-18.195	7.672	-3.049	-64.497	88.406	-42.646	61.206	4.101	2.930	3.838	-7.423	-3.680	-5.402	87.312	-120.950	90.692	-100.224	-38.645	54.917	-50.735	47.867
-1.563	6.615	-17.094	6.986	-2.635	-56.011	86.073	-37.068	48.132	4.131	3.194	2.575	-6.239	-3.167	-4.807	77.949	-123.307	75.612	-76.585	-35.041	57.555	-41.554	36.273

Min. and Max. value of C_P in descent

	Rotor 1	Rotor 2	Rotor 3	Rotor 4	Rotor 5	Rotor 6	Rotor 7	Rotor 7	Rotor 9	Rotor 10	Rotor 11	Rotor 12	Rotor 13	Rotor 14	Rotor 15	Rotor 16	Rotor 17	Rotor 18
Min.	0.0044049	0.0051873	0.0044225	0.0045431	0.0043039	0.0052600	0.0045796	0.0046181	0.0039760	0.0044383	0.0044331	0.0043361	0.0043849	0.0040653	0.0044021	0.0044941	0.0040411	0.0043484
Max.	0.0125732	0.0133816	0.0132519	0.0115596	0.0128855	0.0129800	0.0117935	0.0125556	0.0122391	0.0118505	0.0124350	0.0116238	0.0118765	0.0118147	0.0128946	0.0127718	0.0132413	0.0134446

Table C.4. $\mathbf{C_{RSM}}$ matrix and E matrix of $\mathbf{\bar{C}_P}$ in descent

E matrix	$\mathbf{C_{RSM}}$ matrix																					
-0.044	-3.298	11.968	-1.465	1.904	22.287	-44.151	20.319	-16.255	-0.840	-1.119	-0.905	2.888	0.459	0.765	-30.457	53.620	-43.539	25.792	13.499	-22.235	24.142	-12.373
-2.809	7.184	-1.197	-11.140	-3.180	-31.628	16.687	56.938	29.392	2.404	-0.306	0.793	-5.122	-2.775	0.002	38.239	-15.242	-74.181	-44.273	-15.397	4.298	31.721	20.119
-0.420	-1.790	11.510	-0.951	7.189	16.081	-44.176	2.662	-36.772	-1.561	-0.812	-1.341	4.263	-0.262	-0.437	-20.584	57.373	-7.640	58.435	8.867	-25.285	4.502	-28.089
4.585	-13.395	19.465	3.430	3.173	96.195	-99.120	-2.620	-74.450	-5.356	-4.587	-3.705	11.031	4.645	6.724	-133.969	129.950	-33.871	122.555	60.101	-57.214	27.159	-59.224
-8.753	18.049	-19.283	-12.808	-7.287	-97.150	121.267	68.786	92.681	8.463	1.348	3.351	-18.091	-8.646	-3.295	120.180	-154.542	-58.875	-141.585	-49.294	65.214	14.780	64.687
-0.232	-3.467	25.827	-11.896	9.099	49.024	-103.745	69.108	-68.645	-2.736	-4.050	-3.601	5.097	0.408	5.233	-73.398	136.379	-124.439	109.861	34.917	-59.990	65.494	-53.305
-2.534	0.930	4.740	-9.385	-0.670	8.170	7.461	66.652	-7.215	2.880	-3.485	-2.496	-2.805	-2.866	3.153	-16.340	-21.156	-108.416	19.997	9.235	12.284	54.170	-11.677
1.974	-4.909	16.665	-9.164	6.073	42.776	-75.523	49.152	-52.958	-2.823	-3.023	-2.082	7.254	2.150	3.037	-58.485	93.879	-91.078	81.801	25.953	-39.317	48.256	-38.157
1.303	-2.334	-10.151	8.384	1.538	-0.741	39.073	-38.365	-0.172	0.847	0.955	1.502	1.781	-0.150	-1.298	4.292	-56.430	57.039	-5.223	-3.337	25.639	-27.697	4.427
5.454	-15.715	19.760	-2.483	2.411	103.152	-101.059	18.556	-70.442	-5.150	-4.151	-3.540	9.994	4.772	6.510	-141.923	132.275	-59.162	113.373	62.975	-57.635	37.098	-53.517
-1.670	2.488	1.266	-3.673	-1.013	-16.639	19.371	24.436	8.877	3.942	-0.471	0.154	-5.040	-2.376	0.358	18.965	-33.749	-30.485	-9.223	-7.149	16.165	12.705	2.737
3.749	-6.084	5.535	-5.081	-0.756	38.435	-31.888	25.498	-29.794	-1.357	-1.181	-1.118	4.368	1.684	4.508	-54.437	41.512	-55.377	50.856	24.591	-18.748	30.941	-24.952
-1.204	3.309	4.804	-10.685	-1.361	-20.808	-5.283	50.556	23.368	0.827	0.524	1.365	-0.661	-1.527	-1.609	29.632	1.139	-72.079	-39.713	-13.536	1.352	32.956	19.526
-1.062	3.866	2.657	-0.579	-3.942	-25.864	-4.483	10.150	31.721	1.774	1.672	1.587	-3.584	-1.218	-0.727	33.552	10.134	-11.267	-51.702	-14.551	-6.048	2.942	25.024
-4.649	15.053	-6.994	-14.340	-9.290	-66.731	55.094	76.554	68.777	4.589	1.120	1.423	-12.466	-3.633	0.216	78.369	-66.459	-94.124	-105.090	-30.721	26.262	37.981	48.439
0.413	-3.123	11.615	-5.595	-1.894	46.754	-45.405	42.191	-25.629	-3.247	-3.563	-2.708	2.630	1.377	4.849	-70.588	61.754	-81.194	48.452	33.447	-28.687	43.560	-25.129
4.353	-7.209	21.661	-6.988	4.661	53.529	-113.898	23.081	-52.341	-6.664	-1.244	-0.925	8.999	4.819	3.486	-69.213	159.632	-52.281	74.950	29.149	-72.276	29.327	-33.245
4.034	-9.955	19.279	-0.671	7.087	57.026	-95.501	1.393	-67.772	-4.274	-0.305	-2.356	9.174	3.614	3.279	-74.406	128.262	-27.225	104.778	31.898	-56.770	20.329	-48.827

Min. and Max. value of C_P in descent

	Rotor 1	Rotor 2	Rotor 3	Rotor 4	Rotor 5	Rotor 6	Rotor 7	Rotor 7	Rotor 9	Rotor 10	Rotor 11	Rotor 12	Rotor 13	Rotor 14	Rotor 15	Rotor 16	Rotor 17	Rotor 18
Min.	0.0002352	0.0001898	0.0002316	0.0003064	0.0002369	0.0001970	0.0003133	0.0002322	0.0002135	0.0003053	0.0002323	0.0002605	0.0002975	0.0002374	0.0002497	0.0002821	0.0002236	0.0001825
Max.	0.0004632	0.0004435	0.0004434	0.0004673	0.0004524	0.0004473	0.0004782	0.0004522	0.0004459	0.0004633	0.0004568	0.0004665	0.0004529	0.0004528	0.0004495	0.0004557	0.0004365	0.0004431

Min. and Max. value in sampling points of rotational speed and airspeed

	RPM	U_a	V_a	W_a
Min.	800	-24.87	-20	0.71
Max.	1,800	9.09	10	2

References

[1] Turcksin, T., Bossche, V., D., P., Hendrick, P., "Battery weight optimization for hovering aircraft," *8th European Conference for Aeronautics and Aerospace Sciences*, Madrid, Spain, 2019.

https://doi.org/10.13009/EUCASS2019-880

[2] Hassanalian, M., and Abdelkef, A., "Classifications, applications, and design challenges of drones: A review," *Progress in Aerospace Sciences*, Vol. 91, 2017, pp.99-131.

https://doi.org/10.1016/j.paerosci.2017.04.003

[3] Mckinnon, A.C., "The possible impact of 3D printing and drones on last-mile logistics: An exploratory study," *Built Environ.*, Vol. 42, No. 4, 2016, pp.617-629.

https://doi.org/10.2148/benv.42.4.617

[4] Zhang, H., Wei, S., Yu, W., Blasch, E., Chen, G., Shen, D., and Pham, K., "Scheduling methods for unmanned aerial vehicle based delivery systems," *Proceedings of the IEEE/AIAA Digital Avionics Systems Conference (DASC)*, Colorado Springs, CO, USA, October, 2014.

https://doi.org/10.1109/DASC.2014.6979499

[5] Hii, M.S.Y., Courtney, P., and Royall, P.G., "An Evaluation of the Delivery of Medicines Using Drones," *Drones*, Vol. 3, No. 3, 2019, pp.52.

https://doi.org/10.3390/drones3030052

[6] Demuyakor, J. "The impact of Zipline Drone Technology on Digital Emergency Health Delivery in Ghana," *Shanlax Int. J. Arts Sci. Humanit.* Vol. 8, 2020, pp. 242-253.

https://doi.org/10.34293/sijash.v8i1.3301

[7] Foehn, P., Falanga, D., Kuppuswamy, N., Tedrake, R., and Scaramuzza, D., "Fast trajectory optimization for agile quadrotor maneuvers with a cable-suspended payload," *Proc. Robot., Sci. Syst*, Boston, MA, USA, 2017, pp.1-10.

[8] Lee, T., "Collision avoidance for quadrotor uavs transporting a payload via voronoi tessellation," *2015 American Control Conference*, Chicago, IL, USA, 2015, pp.1842–1848.

https://doi.org/10.1109/ACC.2015.7171001

[9] Faust, A., Palunko, I., Cruz, P., Fierro, R., and Tapia, L., "Automated aerial suspended cargo delivery through reinforcement learning," *Artificial Intelligence*, Vol. 247, 2017, pp.381–398.

https://doi.org/10.1016/j.artint.2014.11.009

[10] Palunko, I., Cruz, P., and Fierro, R., "Agile load transportation: Safe and efficient load manipulation with aerial robots," *IEEE Robotics & Automation Magazine*, Vol. 19 Issue. 3, 2012, pp.69-79.

https://doi.org/10.1109/MRA.2012.2205617

[11] Cruz, P.J., and Fierro, R., "Cable-suspended load lifting by a quadrotor uav: hybrid model, trajectory generation, and control," *Autonomous Robots*, Vol. 41, No. 8, 2017, pp.1629-1643.

[12] Oliveira, D., and Wehrmeister, M., "Using deep learning and low-cost RGB and thermal cameras to detect pedestrians in aerial images captured by multirotor UAV," *Sensors*, Vol. 18, No. 7, 2018, pp.2244. https://doi.org/10.3390/s18072244

[13] Mishra, B., Garg, D., Narang, P., and Mishra, V., "Drone-surveillance for search and rescue in natural disaster," *Comput. Commun.*, Vol. 156, 2020, pp.1-10. https://doi.org/10.1016/j.comcom.2020.03.012

[14] Cao, P., Hwang, J. T., Bewley, T., and Kuester, F., "Mission-Oriented Trajectory Optimization for Search-and-Rescue Multirotor UAVs in Cluttered and GPS-Denied Environments," *AIAA AVIATION 2022 Forum*, Chicago, IL, USA, 2022. https://doi.org/10.2514/6.2022-3999

[15] Cacace, J., Finzi, A., Lippiello, V., Furci, M., Mimmo, N., and Marconi, L., "A control architecture for multiple drones operated via multimodal interaction in search & rescue mission," *2016 IEEE International Symposium on Safety, Security, and Rescue Robotics (SSRR)*, 2016, pp.233-239. https://doi.org/10.1109/SSRR.2016.7784304

[16] Anon., "Photos show 'weaponised commercial drones' in Iraq," BBC News Online, January 18, 2017.

[17] D'Agata, C., "ISIS Drones Pose Another Danger as Iraqi Troops Push For Western Mosul," CBS News, February 20, 2017.

[18] Hao, Z., Qi, L., Wan, J., Musiu, E., Zhou, J., Lu, Z., and Wang, P., "Providing Real Data of Rotor Speed and Pitch Angle for Numerical Simulation of

Downwash Airflow from a Multirotor UAV Sprayer," *Agriculture*. Vol. 11, 2021, pp.1038.

https://doi.org/ 10.3390/agriculture11111038

[19] Hong, S., Zhao, L., and Zhu, H., "CFD simulation of pesticide spray from air-assisted sprayers in an apple orchard: tree deposition and off-target losses," *Atmos. Environ*. Vol.175, 2017, pp.109-119.

https://doi.org/10.1016/j.atmosenv.2017.12.001

[20] Zhu, Y. Z., Guo, Q. W., Tang, Y., Zhu, X., He, Y., Huang, H. S., and Luo, S. M., "CFD simulation and measurement of the downwash airflow of a quadrotor plant protection UAV during operation," *Comput. Electron. Agric.* Vol. 201, 2022.

https://doi.org/10.1016/j.compag.2022.107286

[21] Spoorthi, S., Shadaksharappa, B., Suraj, S., and Manasa, V.K., "Freyr drone: Pesticide/fertilizers spraying drone-an agricultural approach," *IEEE 2nd International Conference on in Computing and Communications Technologies*, Chennai, India, 2017, pp.252-255.

https://doi.org/10.1109/ICCCT2.2017.7972289

[22] Kabra, T. S., Kardile, A. V., Deeksha, M. G., Mane, D. B., Bhosale, P. R., and Belekar, A. M., "Design, Development & Optimization of a Quad-Copter for Agricultural Applications." *International Research Journal of Engineering and Technology*, Vol. 04, Issue. 07, 2017.

[23] Tang, Y., Hou, C. J., Luo, S. M., Lin, J. T., Yang, Z., and Huang, W. F., "Effects of operation height and tree shape on droplet deposition in citrus trees using an

unmanned aerial vehicle," *Computers and Electronics in Agriculture*, Vol. 148, 2018, pp.1-7.

https://doi.org/10.1016/j.compag.2018.02.026

[24] Pradeep, P., Park, S. G., and Wei, P., "Trajectory Optimization of Multirotor Agricultural UAVs," *2018 IEEE Aerospace Conference*, Big Sky, MT, USA, 2018, pp. 1-7.

https://doi.org/10.1109/AERO.2018.8396617

[25] Michael, N., Shen, S., Mohta, K., Mulgaonkar, Y., Kumar, V., Nagatani, K., Okada, Y., Kiribayashi, S., Otake, K., and Yoshida, K., Ohno, K., Takeuchi, E., and Tadokoro, S., "Collaborative mapping of an earthquake-damaged building via ground and aerial robots," *Journal of Field Robotic*, Vol. 29, Issue. 5, 2012, pp.832-841.

https://doi.org/10.1002/rob.21436

[26] Fernandez-Galarreta, J, Kerle, N, and Gerke, M., "UAV-based urban structural damage assessment using object-based image analysis and semantic reasoning," *Nature Hazards and Earth System Science*, Vol. 15, Issue 6, pp.1087-1101.

https://doi.org/10.5194/nhess-15-1087-2015

[27] Liu, J., Michael, J. J., and Holley, P., "Utilizing light unmanned aerial vehicles for the inspection of curtain walls: a case study", *Construction Research Congress*, San Juan, Puerto Rico, 2016.

[28] Santano, D, and Esmaeili, H., "Aerial videography in built heritage documentation: the case of post-independence architecture of Malaysia," *2014*

International Conference on Virtual Systems & Multimedia, Hong Kong, China, 2014.

https://doi.org/10.1109/VSMM.2014.7136680

[29] Li, Y., and Liu, C., "Applications of multirotor drone technologies in construction management," *International Journal of Construction Management*, Vol. 19, Issue. 5, 2019, pp.401-412.

https://doi.org/10.1080/15623599.2018.1452101

[30] Oh, J., Jang, G., Oh, S., Lee, J., Yi, B., Moon, Y., Lee, J., and Choi, Y., "Bridge inspection robot system with machine vision," *Automation in Construction*, Vol. 18, Issue 7, 2009, pp.929-941.

https://doi.org/10.1016/j.autcon.2009.04.003

[31] Gillins, M., Gillins, D., and Parrish, C., "Cost Effective Bridge Safety Inspections Using Unmanned Aircraft Systems (UAS)," *Geotechnical and Structural Engineering Congress 2016*, Phoenix, Arizona, USA, 2016.

https://doi.org/10.1061/9780784479742.165

[32] Iwamoto, T., Enaka, T., Tada, K., "Development of testing machine for tunnel inspection using multi-rotor UAV," *12th International Conference on Damage Assessment of Structures*, Vol. 842, 2017.

https://doi.org/10.1088/1742-6596/842/1/012068

[33] Yoon, S., Gwon, G., Lee, J., and Jung, H., "Three-dimensional image coordinate-based missing region of interest area detection and damage

localization for bridge visual inspection using unmanned aerial vehicles," *Structural Health Monitoring*, Vol. 20, Issue 4, 2020.

https://doi.org/10.1177/1475921720918675

[34] Chen, S., Laefer, D.F., Mangina, E., Zolanvari, S.I., Byrne, J., "UAV Bridge inspection through evaluated 3D reconstructions," *Journal of Bridge Engineering*, Vol. 24, Issue 4, 2019.

https://doi.org/10.1061/(ASCE)BE.1943-5592.0001343

[35] Baur, S., Schickram, S., Homulenko, A., Martinez, N., and Dyskin, A., "Urban air mobility—The rise of a new mode of transportation," Roland Berger GmbH, 2018.

[36] Campbell, S. D., Clark, D. A., and Evans, J. E. "Preliminary Weather Information Gap Analysis for UAS Operations," Project Report ATC-437, MIT Lincoln Laboratory, Lexington, MA, 2017.

[37] Nandakumar, G., Srinivasan, A., Thondiyath, A., "Theoretical anexperimental investigations on the effect of overlap and offset on the design of a novel quadrotor configuration, VOOPS", *Journal of Intelligent and Robotic Systems*, Vol. 92, 2018, pp.615-628.

https://doi.org/10.1007/s10846-017-0707-2

[38] Bershadsky, D., Haviland, S., and Johnson, E., "Electric multirotor propulsion system sizing for performance prediction and design optimization," *57th AIAA/ASCE/AHS/ASC Structures, Structural Dynamics, and Materials Conference*, San Diego, California, USA, 2016.

133

https://doi.org/10.2514/6.2016-0581.

[39] Shi, D., Dai, X., Zhang, X., and Quan, Q, "A practical performance evaluation method for electric multicopters," *IEEE/ASME Trans. Mechatron,* Vol. 22, Issue 3, 2017, pp.1337-1348.

https://doi.org/10.1109/TMECH.2017.2675913

[40] Kim, H., Lim, D., and Yee, K, "Comprehensive analysis and optimized design of multirotor type UAVs," *2019 Asia Pacific International Symposium on Aerospace Technology*, Gold Coast, AUS, 2019, pp.842–851.

https://doi.org/10.3316/informit.943094911613460

[41] Lim, D., Kim, H., and Yee, K., "Unified framework for analysis and design optimization of a multirotor unmanned aerial vehicle," *44th Eur. Rotorcr. Forum*, Delft, Netherlands, 2018.

https://doi.org/10.1016/j.ast.2021.106773

[42] Gray, J. S., Hwang, J. T., Martins, J. R. R. A., Moore, K. T., and Naylor, B. A., "OpenMDAO: An open-source framework for multidisciplinary design, analysis, and optimization," *Struct. Multidiscip. Opim.*, 2019. https://doi.org/10.1007/s00158-019-02211-z

[43] Kim, H., Lim, D., and Yee, K, "Flight Control Simulation and Battery Performance Analysis of a Quadrotor under Wind Gust," *Proceedings of the 2020 International Conference on Unmanned Aircraft Systems (ICUAS'20)*, Athens, Greece, 2020.

https://doi.org/10.1109/ICUAS48674.2020.9214058

[44] Pradeep, P., and Wei, P., "Energy-Efficient Arrival with RTA Constraint for Multirotor eVTOL in Urban Air Mobility," *Journal of Aerospace Information Systems*, Vol. 16, No. 7, 2019, pp.263–277.

https://doi.org/10.2514/1I010710

[45] Pradeep, P., Kulkarni, C. S., Chatterji, G. B., and Lauderdale, T. A., "Parametric Study of State-of-Charge for an Electric Aircraft in Urban Air Mobility," *AIAA Aviation 2021 Forum, American Institute of Aeronautics and Astronautics*, 2021.

https://doi.org/10.2514/6.2021-3181.vid

[46] Kadhiresan, A. R., and Duffy, M. J., "Conceptual Design and Mission Analysis for eVTOL Urban Air Mobility Flight Vehicle Configurations," *AIAA Aviation 2019 Forum, American Institute of Aeronautics and Astronautics*, Dallas, Texas, USA, 2019.

https://doi.org/10.2514/6.2019-2873

[47] Michel, N., Sinha, A.K., Kong, Z., and Lin, X., "Multiphysical Modeling of Energy Dynamics for Multirotor Unmanned Aerial Vehicles," *International Conference on Unmanned Aircraft Systems (ICUAS)*, 2019, pp.738–774.

https://doi.org/10.1109/ICUAS.2019.8797747

[48] Hendricks, E. S., Aretskin-Hariton, E., Ingraham, D., Gray, J. S., Schnulo, S. L., Chin, J., Falck, R., and Hall, D., "Multidisciplinary Optimization of an Electric Quadrotor Urban Air Mobility Aircraft," *AIAA Aviation 2020 Forum, American Institute of Aeronautics and Astronautics*, Virtual Event, 2020.

https://doi.org/10.2514/6.2020-3176

[49] Kim, H., Lim, D., and Yee, K., "Investigation of Operable Conditions and Excess Battery Energy for Quadrotors Under Wind Turbulence," *Journal of Intelligent and Robotic Systems*, Vol. 104, No. 52, 2022, pp.1-21. https://doi.org/10.1007/s10846-021-01494-z

[50] Ding, L., and Wang, Z., "A robust control for an aerial robot quadrotor under wind gusts," *Journal of Robotics*, Vol. 2018, 2018. https://doi.org/10.1155/2018/5607362

[51] Leishman, J. G. "Principles of Helicopter Aerodynamics, second ed." Cambridge University Press, 2006.

[52] Massé, C., Gougeon, O., Nguyen, D., and Saussié, D. "Modeling and control of a quadcopter flying in a wind field: A comparison between LQR and structured H_∞ control techniques," *International Conference on Unmanned Aircraft Systems (ICUAS)*, Dallas, TX, USA, 2018. https://doi.org/10.1109/ICUAS.2018.8453402

[53] Wang, C., Song, B., Huang, P., and Tang, C., "Trajectory tracking control for quadrotor robot subject to payload variation and wind gust disturbance," *Journal of Intelligent and Robotic Systems*, Vol. 83, 2016, pp.315-333. https://doi.org/10.1007/s10846-016-0333-4

[54] Lei, Y., Bai, Y., and Xu, Z., "Wind effect on aerodynamic optimization for non-planar rotor pairs using full-scale measurements," *Journal of Intelligent and Robotic Systems*, Vol. 87, 2017, pp.615-626. https://doi.org/10.1007/s10846-017-0476-y

[55] Davoudi, B., Taheri, E., Duraisamy, K., Jayaraman, B., and Kolmanovsky, I., "Quad-rotor flight simulation in realistic atmospheric conditions," *AIAA Journal*, Vol. 58, No. 5, 2020, pp. 1992-2004.

https://doi.org/10.2514/1.J058327

[56] Waslander, S. L., and Wang, C., "Wind Disturbance Estimation and Rejection for Quadrotor Position Control," *AIAA Infotech64Aerospace Conference*, Arlington, Virginia, USA, 2009.

https://doi.org/10.2514/6.2009-1983

[57] Guo, K., Jia, J., Yu, X., Guo, L., and Xie, L., "Multiple observers based anti-disturbance control for a quadrotor UAV against payload and wind disturbances," *Control Engineering Practice*, Vol. 102, 2020, pp.104560.

https://doi.org/10.1016/j.conengprac.2020.104560

[58] Tran, N. K., Bulka, E., and Nahon, M., "Quadrotor Control in a Wind Field," *2015 International Conference on Unmanned Aircraft Systems*, Piscataway, NJ, USA, 2015, pp.320-328.

https://doi.org/10.1109/ICUAS.2015.7152306

[59] Escareño, J., Salazar, S., Romero, H., and Lozano, R., "Trajectory Control of a Quadrotor Subject to 2D Wind Disturbances," *Journal of Intelligent and Robotic Systems*, Vol. 70, Issue 1. 2013, pp.51-63.

https://doi.org/10.1007/s10846-012-9734-1

[60] Bisheban, M., and Lee, T., "Geometric Adaptive Control for a Quadrotor UAV with Wind Disturbance Rejection," *2018 IEEE Conference on Decision and Control*, Miami, Florida, USA, 2018, pp. 2816-2821.

https://doi.org/10.1109/CDC.2018.8619390

[61] Yang, H., Cheng, L., Xia, Y., and Yuan, Y., "Active Disturbance Rejection Attitude Control for a Dual Closed-Loop Quadrotor Under Gust Wind," *IEEE Transactions on Control Systems Technology*, Vol. 26, No. 4, 2018, pp.1400-1405.

https://doi.org/10.1109/TCST.2017.2710951

[62] Wang, C., Song, B., Huang, P., Tang, C., "Trajectory Tracking Control for Quadrotor Robot Subject to Payload Variation and Wind Gust Disturbance," *Journal of Intelligent and Robotic Systems*, Vol. 83, Issue 2, 2016, pp.315-333.

https://doi.org/10.1007/s10846-016-0333-4

[63] Zhang, C., Zhou, X., Zhao, H., Dai, A., and Zhou, H., "Three-dimensional fuzzy control of mini quadrotor UAV trajectory tracking under impact of wind disturbance," *2016 International Conference on Advanced Mechatronic Systems*, Melbourne, Australia, 2016, pp.372-377.

https://doi.org/10.1109/ICAMechS.2016.7813477

[64] Bisheban, M., and Lee, T., "Geometric Adaptive Control with Neural Networks for a Quadrotor in Wind Fields," *IEEE Transactions on Control Systems Technology*, Vol. 29, No. 4, 2021, pp.1533-1548.

https://doi.org/10.1109/TCST.2020.3006184

[65] Paris, A., Lopez, B. T., and How, J. P., "Dynamic Landing of an Autonomous Quadrotor on a Moving Platform in Turbulent Wind Conditions," *2020 IEEE International Conference on Robotics and Automation*, Virtual, 2020, pp.9577-9583.

https://doi.org/10.1109/ICRA40945.2020.9197081

[66] Miesner, S., Keßler, M., Krämer, E., and Schäferlein, U., "High-fidelity Simulation of the Volocopter-2X in cruise flight," 77th Annual Forum And Technology Display, *Vertical Flight Society*, Virtual, May, 2021.

[67] Johnson, W., and Silva, C., "NASA Concept Vehicles and the Engineering of Advanced Air Mobility Aircraft," *The Aeronautical Journal*, October 2021, pp. 1-33.

https://doi.org/10.1017/aer.2021.92

[68] Misiorowski, M., Gandhi, F., and Oberai, A., "Computational Study on Rotor Interactional Effects for a Quadcopter in Edgewise Flight," *AIAA Journal*, Vol. 57, No. 12, 2019, pp.5309-5319.

https://doi.org/10.2514/1J058369

[69] Hwang, J. Y., Jung, M. K., and Kwon, O. J., "Numerical Study of Aerodynamic Performance of a Multirotor Unmanned Aerial-Vehicle Configuration," *Journal of Aircraft*, Vol. 52, No. 3, 2015, pp.839-846.

https://doi.org/10.2514/1.C032828

[70] Usov, D., Appleton, W., Filippone, A., and Bojdo, N., "Low-Order Aerodynamic Model for Interference in Multirotor Systems," Journal of Aircraft, 2022, pp.1-13.

https://doi.org/10.2514/1.C036797

[71] Han, D., and Barakos, G. N., "Aerodynamic Interference Model for Multirotors in Forward Flight," *Journal of Aircraft*, Vol. 57, No. 6, 2020, pp. 1220-1223.

https://doi.org/10.2514/1.C035978

[72] Barcelos, D., Kolaei, A., and Bramesfeld, G., "Aerodynamic Interactions of Quadrotor Configurations," *Journal of Aircraft*, Vol. 57, No. 6, 2020, pp.1074-1090.

https://doi.org/10.2514/1.C035614

[73] Nguyen, D. H., Liu, Y., and Mori, K., "Experimental Study for Aerodynamic Performance of Quadrotor Helicopter," *Transactions of the Japan Society for Aeronautical and Space Sciences*, Vol. 61, No. 1, 2018, pp. 29-39.

https://doi.org/10.2322/tjsass.61.29

[74] "Zhu, Y., Lin, D., Li, M., Lv, P., and Ye, J., ""Numerical Study of the Aerodynamic Interference of Rotors Imposed on Fuselage for a Quadrotor,"" IEEE Acess, Vol.9, 2021, pp.150021-150036.

https://doi.org/10.1109/ACCESS.2021.3124507

[75] Luo, J., Zhu, L., and Yan, G., "Novel Quadrotor Forward-Flight Model Based on Wake Interference," *AIAA Journal*, Vol. 53, No. 12, 2015, pp.3522-3533.

https://doi.org/10.2514/1.J053011

[76] Diaz, P., and Yoon, S., "High-Fidelity Computational Aerodynamics of Multi-Rotor Unmanned Aerial Vehicles," *56th AIAA Aerospace Sciences Meeting*, Kissimmee, Florida, USA, 2018.

https://doi.org/10.2514/6.2018-1266

[77] Yoon, S., Lee, H. C., and Pulliam, T. H., "Computational Analysis of Multi-Rotor Flows," *54th AIAA Aerospace Sciences Meeting*, San Diego, California, USA, 2016.

https://doi.org/10.2514/6.2016-0812

[78] Tanabe, Y., Aoyama, T., Sugiura, M., Sugawara, H., Sunada, S., Yonezawa, K., and Tokutake, H., "Numerical Simulations of Aerodynamic Interactions Between Multiple Rotors," *42nd European Rotorcraft Forum*, Lille, France, 2016.

[79] Ilka,R., Tilaki, A.R., Asgharpour-Alamdari, H., and Baghipour, R. "Design optimization of permanent magnet-brushless DC motor using elitist genetic algorithm with minimum loss and maximum power density," *Int. J. Mechatron. Electr. Comp. Technol.* Vol. 4, 2014, pp.1169-1185.

[80] German, B. J., "Introduction to Batteries and Cell Discharge Modeling for Electric Aircraft Design," *AIAA Workshop on Electric Aircraft Design*, June, 2018.

[81] Dahl, H., and Faulkner, A., "Helicopter simulation in atmospheric turbulence," *Proceedings of the 4th European Rotorcraft Forum*, 1978.

[82] Kim, T., Oh, S., and Yee, K., "Improved Actuator Surface Method for Wind Turbine Application," *Renewable Energy*, Vol. 76, 2015, pp.16-26.

https://doi.org/10.1016/j.renene.2014.11.002

[83] Jasak H., "Error Analysis and Estimation for the Finite Volume Method with Applications to Fluid Flows", Ph.D. thesis, Imperial College London, 1996.

[84] Kim, H., and Yee, K., "Downwash Effect on the Unguided Rocket under Rotor Wake and External Wind," *Transactions of the Japan Society for Aeronautical and Space Sciences*, Vol. 63, No. 3, 2020, pp.80-89.

https://doi.org/10.2322/tjsass.63.80

[85] Son, C., Oh, S., and Yee, K., "Ice Accretion on Helicopter Fuselage Considering Rotor-Wake Effects," *Journal of Aircraft*, Vol. 54, No. 2., 2017, pp. 500-518.

https://doi.org/10.2514/1.C033830

[86] Theys, B., Dimitriadis, G., Andrianne, T., Hendrick, P., and Schutter, J. D., "Experimental and numerical study of micro-aerial-vehicle propeller performance in oblique flow," *Journal of Aircraft*, Vol. 54, 2017, pp.1076-1084.

https://doi.org/10.2514/1.C033618

[88] Lim, D., Kim, H., and Yee, K., "Mission-Oriented Performance Assessment and Optimization of Electric Multirotors," *Aerospace Science and Technology*, Vol. 115, 2021, Art 106773.

https://doi.org/10.1016/j.ast.2021.106773

[89] Arbanas, B., Ivanovic, A., Car, M., Haus, T., Orsag, M., Petrovic, T., and Bogdan, S., "Aerial-ground robotic system for autonomous delivery tasks," *2016 IEEE International Conference on Robotics and Automation (ICRA)*, Stockholm, Sweden, 2016, pp.5463-5468.

https://doi.org/10.1109/ICRA.2016.7487759

[90] Gawel, A., Kamel, M., Novkovic, T., Widauer, J., Schindler, D., von Altishofen, B.P., Siegwart, R., and Nieto, J., "Aerial picking and delivery of magnetic objects with mavs," *2017 IEEE International Conference on Robotics and Automation (ICRA)*, Singapore, 2017, pp.5746-5752.

https://doi.org/10.1109/ICRA.2017.7989675

[91] Sankarasrinivasan, S., Balasubramanian, E., Karthik, K., Chandrasekar, U., and Gupta, R., "Health monitoring of civil structures with integrated UAV and image processing system," *Procedia Computer Science*, Vol. 54, 2015, pp.508-515.

https://doi.org/10.1016/j.procs.2015.06.058

[92] U.S. Military Specification. MIL-F-8785C, 1980.

[87] Harris, F. D., "Hover Performance of Isolated Proprotors and Propellers— Experimental Data," NASA Ames Research Center, CR-219486, Dec. 2017.

국문 초록

무익기형 전기 추진 수직 이착륙기는 택배 및 운송 서비스, 수색 및 구조, 국방, 농업, 구조물 점검과 같은 분야에서 대표적으로 이용되고 있는 항공기이다. 쿼드로터는 이러한 임무를 수행하기 위한 대표적인 소형 무익기형 전기 추진 수직 이착륙기이다. 대형 무익기형 전기 추진 수직 이착륙기는 효율적인 제자리 비행 성능, 높은 내풍성, 낮은 소음 공해와 같은 특징으로 인해 도심 내 운항 서비스를 위한 항공기로 활용되고 있다.

무익기형 전기 추진 수직 이착륙기의 여러 회전 날개는 안정된 비행을 유지하기 위해, 지속해서 회전 속도를 변화시킨다. 게다가, 모터의 회전 속도와 부하되는 토크 또한 지속적으로 변화한다. 그러므로 무익기형 전기 추진 수직 이착륙기의 비행 성능을 예측하기 위해, 제어기에서 각 회전 날개에 부여된 회전 속도에 따른 추력 및 토크를 해석해야 한다. 그리고 이러한 회전 날개의 회전 속도를 유지하기 위해 모터에 부하 되는 토크를 기반으로, 모터에서 요구되는 전력을 예측해야 한다.

본 논문에서는 제어, 회전 날개 공력, 전기 추진 시스템 해석이 포함된 다학제 해석 기반의 비행 시뮬레이션 프레임워크를 제시한다. 비행 시뮬레이션 프레임워크를 이용하여, 실제 운용 환경에서의 무익기형 전기 추진 수직 이착륙기 비행 성능을 예측할 수 있다.

비행 시뮬레이션 프레임워크를 활용하여 쿼드로터에 대해 외풍을 저항하기 위한 비행 전반적인 성능과 그에 따른 배터리 에너지 소모를 예측하였다. Von Kármán 외풍 난류와 Beaufort 외풍 강도 등급을

활용하여 남실바람, 건들바람, 된바람 환경에 대한 산업용 쿼드로터의 비행시간을 조사하였다. 그 결과, 동일한 외풍 환경일지라도 전진 비행 속도가 증가할수록 배터리 소요 에너지가 증가한다는 것을 밝혔다. 전진 비행 속도의 증가로 인해 쿼드로터에 유입되는 유속이 증가하여, 동체 항력, 위치 오차, 기수 내림 각도, 요구 기계 동력이 증가하였다. 그리고 특정 외풍 속도와 전진 속도 이상에서의 쿼드로터는 요구되는 회전 날개의 회전 속도가 모터의 회전 속도의 한계보다 높으므로 비행할 수 없었다.

또한, 비행 시뮬레이션 프레임워크를 활용하여 도심 운항 서비스용 무익기형 전기 추진 수직 이착륙기의 전반적인 비행 성능을 예측하였다. 여러 회전 날개의 특징으로 인해, 회전 날개 간 거리와 회전 날개의 회전 방향에 따라 회전 날개 간 간섭효과가 필연적으로 비행 성능에 영향을 미친다. 이때, 운용에 유리한 최적의 회전 날개 회전 방향이 존재한다. 본 논문에서 실제 운용에서 바람직한 비행 성능을 발휘하는 회전 날개의 회전 방향에 대한 개념인 FRRA 를 제시하였다. FRRA 는 전방 로터의 후퇴 측과 후방 로터의 전진 측이 일직선으로 정렬된 상태의 회전 방향이다. FRRA 회전 방향은 고속 전진 비행에서 회전 날개 간 간섭효과로 인한 추력 손실이 최소화된다. 회전 날개 간 간섭효과로 인해 불리한 비행 성능을 가지는 회전 방향 대비 FRRA 회전 방향은 도심 항공 교통 서비스에 대한 일반적인 운용에서 배터리 소모율이 7% 정도 감소하였다.

주요어: 무익기형 전기 추진 수직 이착륙기, 다학제, 공력 해석, 다단 제어, 전기 추진 시스템, 6-자유도, 외풍 난류, 회전 날개 간 간섭효과,

압력판 기법

학번: 2018-33010

성명: 김형석

146

압력판 기법

학번: 2018-33010

성명: 김형석